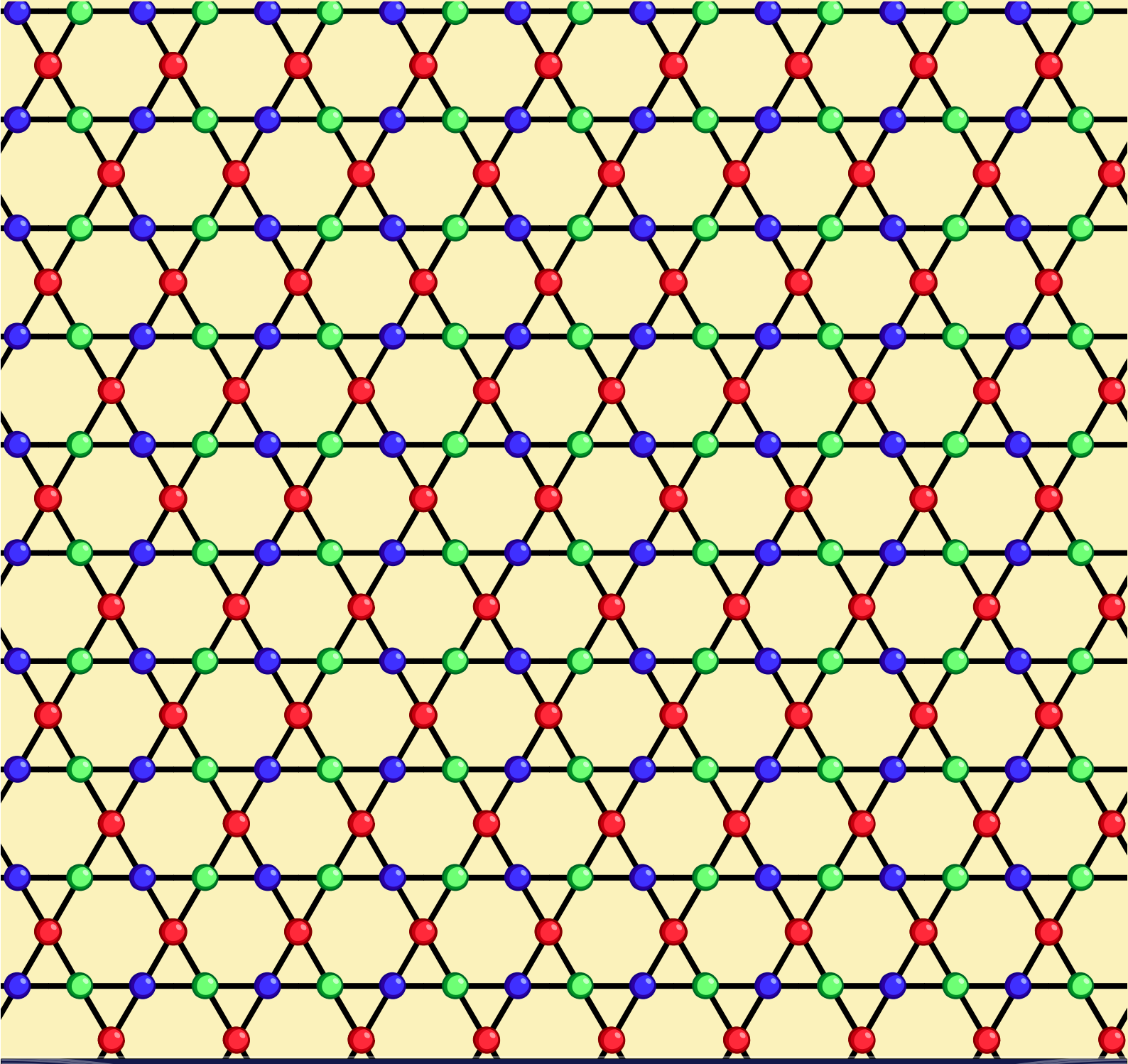

Engineering tunable edge states in kagome platforms

Sajid Sekh

Engineering electronic edge states in kagome platforms

Sajid Sekh

Kraków, 2026

THE HENRYK NIEWODNICZAŃSKI
INSTITUTE OF NUCLEAR PHYSICS
POLISH ACADEMY OF SCIENCES

Institute of Nuclear Physics PAS

A thesis submitted for the degree of

Doctor of Philosophy in Physics

Supervisor: dr. hab. Andrzej Ptok, prof. IFJ PAN

Co-supervisor: dr. hab. Przemysław Piekarz, prof. IFJ PAN

Acknowledgements

Several individuals have made it possible for me to complete this thesis, and it is my pleasure to acknowledge them here.

First and foremost, I would like to thank my supervisor, Prof. Andrzej Ptok, for his continuous mentorship and guidance over the years. Many of the skills I possess today, whether in physics, computation, or maintaining calm under pressure, I owe it to him. His door was always open whenever I had any problems, and he was consistently generous with his time and support. I especially value the academic freedom under his supervision, which has helped me to learn and work on different topics.

I am also grateful to my co-supervisor, Prof. Przemysław Piekarz, for his role during my PhD. His guidance and support, particularly during challenging moments, have been instrumental to the thesis completion. Thanks to him, I now know more about *ab initio* calculation and psychedelic music than when I started.

During the doctoral school, I greatly benefited from scientific collaborations at both national and international levels. In this regard, I acknowledge the NAWA-STER program for providing financial support for my visit to Uppsala University, Sweden, under project no. BPI/STE/2023/1/00027/U/00001. At Uppsala, I had the opportunity to work with Prof. Annica Black-Schaffer, which developed into a long-standing, fruitful collaboration. I extend my sincere gratitude to her for arranging my visit at short notice and for her insightful feedback and meticulous comments,

which have been crucial to this thesis. It was also a pleasure to interact with the team at Uppsala, and I would especially like to thank Arnob for his help upon my arrival.

I would also like to express my sincere thanks to Prof. Andrzej Oleś and Prof. Wojciech Brzezicki from Jagiellonian University for choosing to work with me. Their long-term collaboration provided me with good exposure to DFT and nickelate superconductors. In this context, I acknowledge the support from the National Science Centre (NCN, Poland) under Project No. 2021/43/B/ST3/02166.

A significant part of this thesis relied on heavy numerics, and I gratefully acknowledge the Polish high-performance computing infrastructure PLGrid (HPC Center: ACK Cyfronet AGH) for providing computational resources and support under grants no. PLG/2023/016835, PLG/2024/017875, and PLG/2025/018954.

Lastly, my acknowledgements would not be complete without appreciating those who supported me beyond academia. I am indebted to my parents, who played a great role in helping me achieve what I have today. I thank them for their unconditional support. Additionally, I have benefited from wonderful friends who have inspired me to work harder, helped me during challenging times, and given me unforgettable memories. I thank each one of them through this thesis.

Abstract in English

Advances over the past decades have brought condensed matter physics to a crossroads with topology, leading to the development of topological phases of matter. Topological phases are characterized by bulk properties, which are protected by global details rather than local order parameters. Materials exhibiting such topological phases are hypothesized to be insensitive to local perturbations such as impurities or disorder. This is highly advantageous for device applications, where such imperfections are often unavoidable. A fascinating consequence of topological bulk order is the emergence of electronic states at the boundaries of materials. These conducting states are typically known as edge or surface states that exist alongside an insulating bulk.

In this thesis, we propose kagome-structured materials as a platform for designing electronic edge states. While the kagome lattice shares similarities with the honeycomb lattice in its electronic band structure, it uniquely hosts an additional flat band. Moreover, kagome lattices appear in a wide range of compounds exhibiting diverse phenomena, including charge density waves, superconductivity, spin–orbit coupling, and magnetism.

Motivated by these features, we investigate both pristine and topological edge states of kagome lattices in the monolayer limit. Pristine edge states arise from physical lattice termination, and we identify four distinct terminations obtained via line cuts. These terminations influence the presence and number of edge states, and in some

cases, can fully suppress them. When intrinsic spin–orbit coupling (SOC), modeled via the Kane–Mele framework, is introduced, these states become topological. The resulting edge states are spin-polarized and counter-propagating, consistent with $\mathbb{Z}_2$ helical edge states, which we confirm using the Wilson loop method. We further demonstrate that breaking time-reversal symmetry leads to chiral edge states. By combining ferromagnetism with Rashba SOC, two topological bulk gaps emerge, resulting in gapless chiral states across all terminations. Adding Kane–Mele coupling widens the bulk gap and gives rise to two distinct topological phases. However, chiral edge states can also emerge purely from noncollinear magnetic order. In this scenario, the magnetic exchange field can exhibit two distinct regimes depending on the degree of out-of-plane spin canting, and we analyze chiral states in both regimes. Our results demonstrate that Kane–Mele SOC can open or close bulk gaps and induce different topological phases, depending on the strengths of SOC and the magnetic exchange field.

Overall, our results show that tuning SOC and magnetism enables control over bulk gaps and topological phases, which may be useful for engineering diverse and tunable edge states in kagome lattice platforms.

Abstrakt w języku polskim

Postępy w ciągu ostatnich dekad doprowadziły fizykę materii skondensowanej do skrzyżowania z topologią, prowadząc do rozwoju topologicznych faz materii. Fazy topologiczne charakteryzują się właściwościami objętościowymi, które są chronione przez globalne własności, a nie lokalne parametry porządku. Zakłada się, że materiały wykazujące fazy topologiczne są niewrażliwe na lokalne zaburzenia, takie jak zanieczyszczenia i nieporządek. Jest to niezwykle korzystne w zastosowaniach w urządzeniach, gdzie takie niedoskonałości są często nieuniknione. Fascynującą konsekwencją topologicznego porządku objętościowego jest pojawianie się stanów elektronowych na granicach materiałów. Te stany przewodzące prąd są zazwyczaj znane jako stany krawędziowe lub powierzchniowe, które występują przy izolatorze.

W niniejszej pracy proponujemy materiały o strukturze kagome jako platformę do projektowania elektronicznych stanów krawędziowych. Chociaż sieć kagome ma podobieństwa do sieci plastra miodu w swojej strukturze pasm elektronowych, to w unikalny sposób posiada dodatkowe płaskie pasmo. Co więcej, sieci kagome występują w szerokiej gamie związków wykazujących różnorodne zjawiska, takie jak fale gęstości ładunku, nadprzewodnictwo, sprzężenie spin-orbita i magnetyzm.

Zmotywowani tymi cechami, badamy zarówno pierwotne, jak i topologiczne stany krawędziowe sieci kagome w granicy monowarstwy. Pierwotne stany krawędziowe powstają w wyniku fizycznej terminacji sieci i identyfikujemy cztery różne terminacje uzyskane poprzez przecięcia liniowe. Terminacje te wpływają na obecność

i liczbę stanów krawędziowych, a w niektórych przypadkach mogą je całkowicie stłumić. Po wprowadzeniu wewnętrznego sprzężenia spin–orbita (z ang. *spin–orbit coupling* SOC), modelowanego za pomocą modelu Kane–Mele, stany te stają się topologiczne. Powstałe stany krawędziowe są spolaryzowane spinowo i propagują się w przeciwnych kierunkach, zgodnie z helikalnymi stanami krawędziowymi $\mathbb{Z}_2$, co potwierdzamy za pomocą metody pętli Wilsona. Ponadto wykazujemy, że złamanie symetrii odwrócenia w czasie prowadzi do chiralnych stanów krawędziowych. Połączenie ferromagnetyzmu z polem magnetycznym indukowanym przez SOC typu Rashba powoduje powstanie dwóch topologicznych przerw objętościowych, skutkując bezprzerwowymi stanami chiralnymi dla wszystkich rodzajów krawędzi. Dodanie sprzężenia typu Kane–Mele poszerza przerwę objętościową i prowadzi do powstania dwóch odrębnych faz topologicznych. Jednakże chiralne stany krawędziowe mogą również powstawać wyłącznie z niekolinearnego porządku magnetycznego. W tym scenariuszu pole wymiany magnetycznej może wykazywać dwa odrębne stany w zależności od stopnia przechylenia spinu poza płaszczyznę. Analizujemy stany chiralne w obu przypadkach. Uzyskane wyniki pokazują, że pole magnetyczne indukowane przez Kane–Mele SOC może otwierać lub zamykać przerwy objętościowe i indukować różne fazy topologiczne, w zależności od natężenia pola magnetycznego i pola wymiany magnetycznej.

Ogólnie rzecz biorąc, nasze wyniki pokazują, że dostrojenie pola magnetycznego i porządku magnetycznego umożliwia kontrolę nad przerwami objętościowymi i fazami topologicznymi, co może być przydatne w projektowaniu zróżnicowanych i dostrajalnych stanów krawędziowych w układach zawierających sieci kagome.

Activity during doctoral program

List of publications:

- S. Sekh, and A. M. Black-Schaffer, A. Ptok, *Kagome edge states under lattice termination, spin-orbit coupling, and magnetic order*, arXiv:2602.12223 (2026)
- S. Sekh, and A. Ptok, W. Brzezicki, P. Piekarz, A. M. Oleś, *Electronic and magnetic properties of the* $NdNiO_2/SrTiO_3$ *thin films*, arXiv:2512.19916 (2025)
- S. Sekh, and A. Ptok, *Topological in-gap chiral edge states in the superconducting Haldane model with spin-orbit coupling*, Phys. Rev. B 112, 064501 (2025)
- S. Yadav, S. Sekh, and A. Ptok, *Low temperature phase of* $AuSn_4$ *induced by the van der Waals interactions*, Phys. Rev. Materials 9, 034202 (2025)

Oral and poster presentations:

- Oral – Zakopane School of Physics, Zakopane, 23 May, 2025. *Topological in-gap chiral edge states in superconducting Haldane model with spin-orbit coupling.*
- Oral – XXI National Superconductivity Conference, Jagiellonian University, Kraków, 25 Sep., 2024. *Electronic and magnetic properties of infinite-layer nickelates.*
- Poster – Multiscale Phenomena in Condensed Matter, IFJ PAN, Kraków, 16-19 Sep., 2024 *Electronic and magnetic properties of infinite-layer nickelates.*

- Oral – Quantum Many Body Theory meeting, Jagiellonian University, Kraków, 22 Jan., 2024. *Electronic and magnetic properties of infinite-layer nickelates.*

- Oral – NZ33 department seminar, IFJ PAN, Kraków, 4 June, 2024. *On the edge states of kagome lattice.*

- Oral – Quantum Matter Theory group at Uppsala University, Uppsala, Sweden, 23 Dec., 2024. *Detecting the band topology of 3D semimetals using circular dichroism.*

- Poster – Autumn School on Correlated Electrons, Jülich, Germany, Oct. 2022. *Circular dichroism: an optical recipe for detecting band-topology in 3D semimetals.*

Achievements:

- Best poster award at the MULTIS conference hosted by IFJ PAN in Kraków, 2024.

- Schematic artwork was featured on the cover of Annalen der Physik 535, 4 (2023).

- NAWA-STER (NCN, Poland) scholarship for a two-month research visit to the Quantum Matter Theory group at Uppsala University, Sweden (2023).

Grants:

- We gratefully acknowledge the Polish high-performance computing infrastructure PLGrid (HPC Center: ACK Cyfronet AGH) for providing computer facilities and support within computational grants no. PLG/2023/016835, PLG/2024/017875, and PLG/2025/018954.

- We kindly acknowledge support from the National Science Centre (NCN, Poland) under Project No. 2021/43/B/ST3/02166.

Contents

1 Introduction

1.1 Historical perspective

The kagome lattice is formed by corner-sharing triangles arranged in a hexagonal fashion. In more technical terms, the pattern is an example of trihexgonal tilling [1], which is one of the eleven uniform tilings of the Euclidean plane in tilling theory. While the kagome lattice has gained prominence in physics only in the past century, its origins date back much further. In East Asia, the traditional bamboo weaving patterns [2] feature the kagome structure (see Fig. 1.1), which dates back thousands of years ago [3] . The pattern also has a long history of religious connotations, as it appears in different cultures as the Star of David or the hexagram.

In Physics, the term “kagome lattice" was coined by Kodi Huisimi [5]. It began with the seminal work of Onsager in 1944, where he derived the exact solution of the Ising model on the square lattice [6]. This inspired others to pursue spin physics on different lattices. A breakthrough came in 1950 when Kodi Huisimi and Itiro Syôzi of Osaka University were expanding on Onsager’s work. By simplifying the method of Onsager and using a

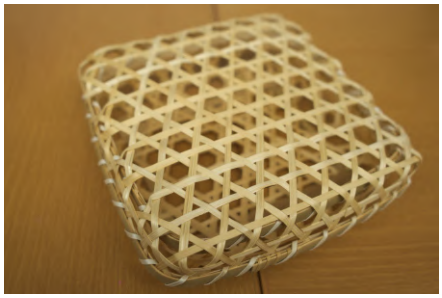

Figure 1.1: Kagome pattern in traditional handmade Japanese basket. Adapted from Ref. [4].

dual transformation, Huisimi and Syôzi were able to find the analytical solutions on the triangular and honeycomb lattice [7]. In parallel, Syôzi was trying to understand the phase transition in a decorated honeycomb lattice, where he placed an extra spin on the sides and vertices of the lattice. Using star-to-triangle transformation, Syôzi demonstrated [8] that the decorated honeycomb lattice maps to a new type of lattice. Now known as kagome lattice, the word first appears in Syôzi's work in 1951, where the author acknowledges Husimi for introducing kagome lattice to him. Syôzi showed that while the ferromagnetic (FM) kagome lattice has a logarithmic divergence at transition, the antiferromagnetic (AFM) counterpart exhibits no phase transition.

Nearly two decades later, Takano and colleagues at Kyoto reported the first observation [9] of a quasi-two-dimensional kagome lattice in jarosite minerals. Jarosites are a family of compounds with the chemical formula $AFe_3(SO_4)_2(OH)_6$, where A is a monovalent cation. In these materials, the Fe^{3+} ions form a quasi-2D kagome lattice in the *ab* plane, characterized by strong in-plane interactions and weak out-of-plane coupling. The kagome lattice signature was evident in their unusual magnetic behavior: Takano *et. al.* observed that, despite strong AFM interactions, long-range magnetic order only emerged at low temperatures (~ 50 K), reflecting the hallmark frustration of the lattice. In the 1990s, another kagome compound $SrCr_8Ga_4O_{19}$, studied [10] at Bell Labs, displayed similar anomalous magnetic properties. On the theoretical front, these experimental realizations drew more attention due to a milestone work of Philip W. Anderson in 1973 [11]. His proposal of the resonating valence bond (RVB) theory highlighted the possibility that geometric frustration could prevent conventional magnetic order and give rise to novel quantum states.

Over the years, kagome platforms have emerged as an increasingly popular topic of research. As illustrated in Fig. 1.2, the number of arXiv submissions with the word "kagome" in the title has grown steadily over time. In the early days, research activity notably increased following the discovery of spin-liquid material Herbert-

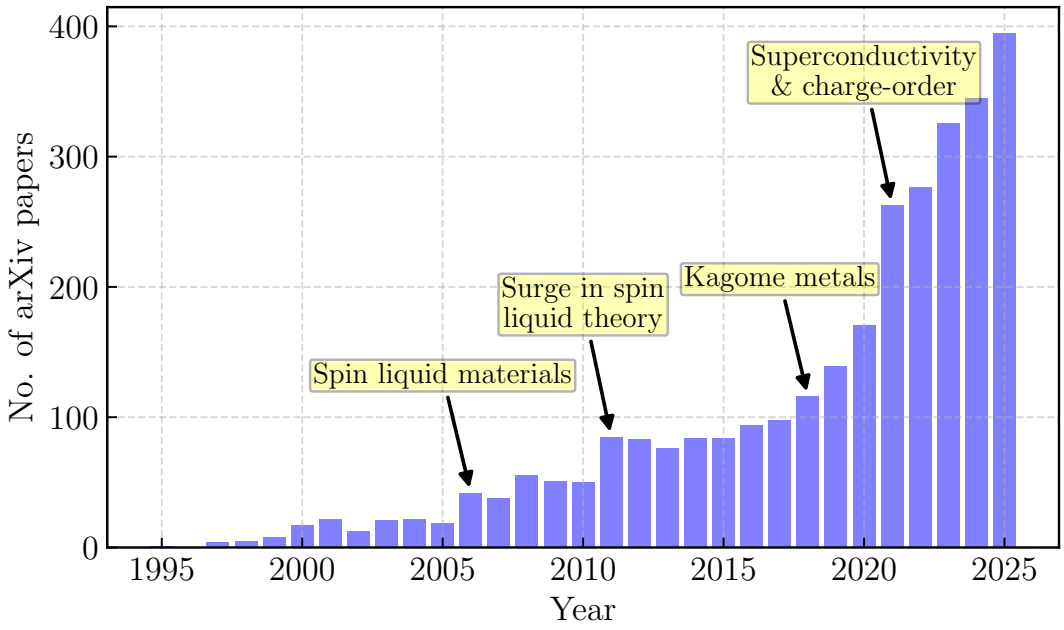

Figure 1.2: Number of arXiv papers with the word “kagome" in the title. Major milestones are marked with arrows.

smithite [12, 13], and was further boosted by theoretical developments in spin-liquid physics [14–20]. Interest surged again after the discovery of kagome metals [21–23] around 2019, and especially from 2020 onward, when superconductivity (SC) and charge order were observed [24–28]. Today, kagome platforms serve as a versatile testbed for exploring a wide range of phenomena, including chiral spin liquids, charge and spin order, correlation effects, and topological phases. In the next section, we provide an overview of key experimental signatures in kagome materials.

1.2 Overview of experimental trends

1.2.1 Charge density wave and superconductivity

In “135” AV_3Sb_5 (A= K, Rb, Cs) [28] kagome materials, both theoretical and experimental studies indicate the presence of a charge ordering phase intertwined with

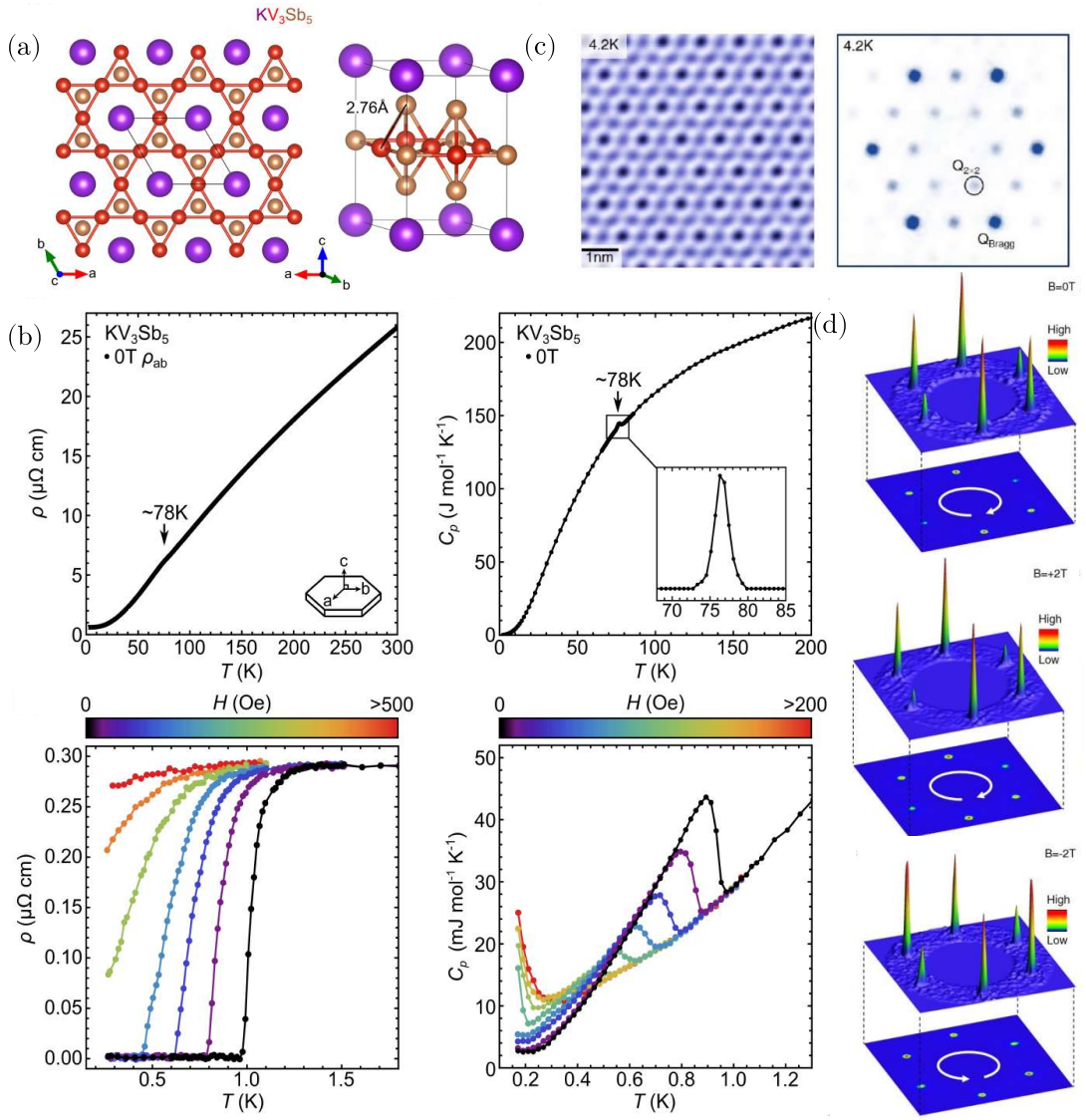

Figure 1.3: (a) Crystal structure of kagome superconductor KV_3Sb_5. (b) Experimental resistivity ρ and heat capacity C_p plotted as a function of T (top). Both plots showcase an anomaly at $T^* = 78$ K, which is highlighted in the inset of C_p plot. Same plots as top but in the range $T < 2$ K corresponding to the bulk superconductivity regime (bottom). (c) 2×2 charge density order and its Fourier transformed pattern. (d) Spectroscopic maps at different magnetic fields ($B = 0$ T, 2 T, -2 T) indicates chiral charge order. Chirality is measured by traversing from lowest to highest peaks. Adapted from Ref. [28] and Ref. [27].

SC [26, 29–32]; however, the underlying mechanism is intensely debated. A charge ordering phase, often called a charge density wave (CDW), refers to the localization of electronic charge in real space with periodicity that may be commensurate or incommensurate with the lattice unit cell. From an electronic perspective, this is interesting because SC contradicts the idea of localization, and thus, CDW and SC are competing phases.

Experimental results for one of the kagome materials KV_3Sb_5 [28] is shown in Fig. 1.3. As discussed previously, the V atoms make the kagome lattice, while Sb atoms are arranged in a honeycomb fashion [see Fig. 1.3(a)]. Top panel of Fig. 1.3(b) reveals that in-plane (*ab*) resistivity and specific heat exhibit a slight kink at the temperature $T^* \sim 78$ K. This suggests an electronic instability, where the electronic charges reorder themselves in a CDW pattern. Bottom panel of Fig. 1.3(b) showcases resistivity and specific heat at lower temperatures (below 2 K). Here, the charge order slowly gets suppressed and the SC phase emerges. Scanning tunnelling microscopy (STM) data shows that the CDW has a 2×2 structure at $T = 4.2$ K, as shown in Fig. 1.3(c). In the same figure but on the right, we have Fourier transform of CDW pattern, which shows the wavevectors associated with CDW. The more intense peaks stem from the Bragg diffraction, while less intense peaks with smaller magnitudes refers to the enlarged charge order periodicity in real space. Although T^* can change depending on the alkali atoms (A= K, Rb, Cs), the 2×2 structure is observed in all kagome variants. Instead of charges, the spatial modulation can also occur in spins or Cooper pairs, which lead to spin [33] and pair [34] density waves, respectively. Additionally, the ordered phase can break rotational symmetry, resulting in a nematic order [35–37], or break both translational and rotational symmetries, leading to a stripe order [38].

Different measurements further report that the CDW phase breaks the time-reversal symmetry (TRS) [27, 39] due to its chiral nature. Being one of the symmetries of the Hamiltonian, TRS significantly affects the nature of edge states, which we will dis-

cuss later. More recent study [40] also suggests breaking of TRS, as μSR data hints towards internal fields that could be connected with TRS breaking loop currents. Additionally, transverse field μSR reveals a power-law dependence with temperature, which is typical of nodal SC, a type of SC where the superconducting gap exhibits point or line nodes on the Fermi surface. This suggests their origin may lie in the complex interplay between lattice distortion and loop currents. This is better illustrated in Fig. 1.3(d), where charge modulation peaks change follow a clockwise or anticlockwise pattern based on magnetic field. Since connected by correlation, the density-ordered phases often precede unconventional superconductivity, and promote Copper pairing with finite angular momenta. In fact, the nonlocal Hubbard model on the kagome lattice favors such exotic pairing mechanisms and intriguing ordered phases [41].

1.2.2 Spin-orbit coupling and Berry curvature

The rise of topological physics has made Berry curvature (BC) a significant concept in condensed matter. BC can be thought of as a geometric property of electronic wavefunctions in momentum space that acts like a magnetic field. SOC and out-of-plane magnetization is a popular route to engineer tunable BC in materials, leading to gapless chiral modes inside bulk Chern gap [see Fig. 1.4(a)]. These two factors typically give rise to a topological Chern phase with broken TRS. One of the hallmarks of the Chern phase is the anomalous Hall effect (AHE) [42], in which Hall conductance is generated from Berry curvature without any external magnetic field.

This makes kagome magnets with SOC of great interest. One of the earlier candidates was Fe_3Sn_2 [21, 44], which is reported to be a bilayer FM with finite SOC. However, no zero-field AHE is observed in Fe_3Sn_2 so far. This can be attributed to its in-plane magnetization with complex magnetic texture. The in-plane magnetization

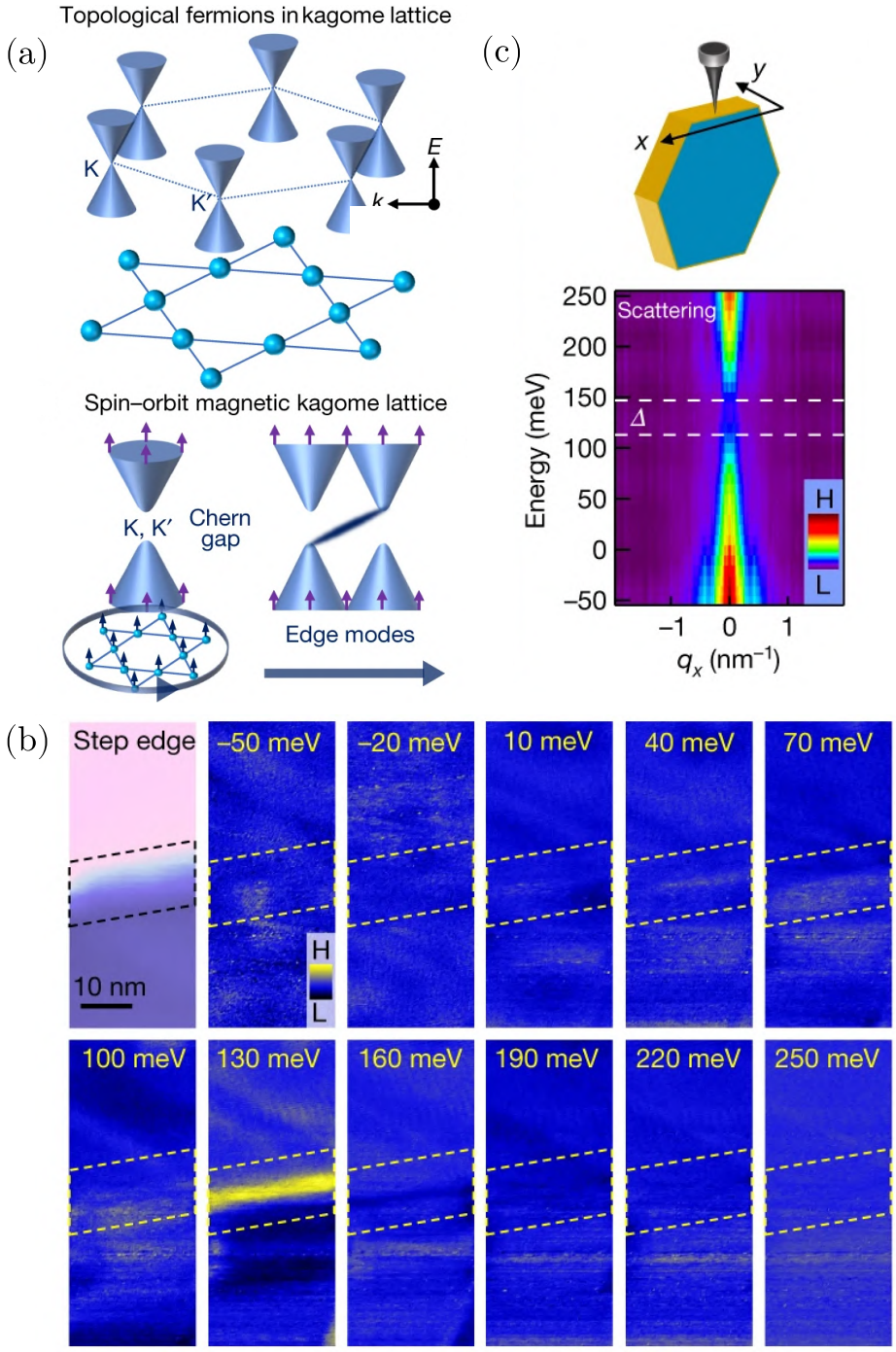

Figure 1.4: (a) Schematic describes SOC-induced Chern gap in kagome lattice. Chern gap is characterized by a gapless edge state connecting upper and lower bulk bands. (b) Gapless edge state can be identified by peak in dI/dV map at 130 meV. (c) Quasiparticle interference pattern shows the energy-momentum relation. Dashed white lines indicate Chern gap $\Delta = 34$ meV. Adapted from Ref. [43].

competes with intrinsic SOC and tends to close the Chern gap required for finite BC. Another issue is that Sn atoms lie in the center of the kagome net (made by Fe), and hopping to Sn atoms deviates from the ideal kagome band structure [45].

Relatively newer “166" RMn_6Sn_6 (R = Gd, Tb, Dy, Ho, Er) compounds [43, 46–48] look promising in this aspect due to their out-of-plane magnetic order and SOC effects. These are part of a bigger kagome family AM_6X_6 [49], where A is an alkali or rare-earth atom, M refers to transition metals, and X site denotes group IV elements (Sn, Ge, Si). Setting M=Mn and X=Sn produces the RMn_6Sn_6 compounds with R site containing a rare earth element. Unlike Fe_3Sn_2, the heavier R sites can push the Sn atoms to create the ideal kagome bands. Subsequently, a wide choice of possible of rare-earth atoms in such compounds make it easy to tune SOC and Chern phases [47].

Particularly interesting is the compound $TbMn_6Sn_6$, where Mn atoms forming the kagome layer exhibit FM order along the *c*-axis. Spectroscopic measurements [43] reveal that the Dirac point (DP) is located approximately 130 meV above the Fermi level (E_F). DPs refer to points of degeneracy in the band structure, around which the dispersion follows a linear relation. This linear relationship gives rise to quasi-particles that behave like massless Dirac fermions, similar to those in high-energy physics. DPs were originally identified in graphene [50], where they give rise to high carrier mobility and relativistic-like electronic behavior. Here, out-of-plane magnetization and SOC open a finite Chern gap of about 34 meV at the DP [see Fig. 1.4(c)]. Edge states arising from this Chern gap are seen in the dI/dV map at 130 meV [see Fig. 1.4(b)]. Since the Fermi level does not lie within this gap, the system is in a Chern metallic phase. This behavior contrasts with that of a Chern insulator, where E_F lies inside the Chern gap, resulting in a quantized anomalous Hall conductivity $\sigma_{xy} = (e^2/h)C$, with C being an integer (Chern number) characterizing the topological phase. The details of such quantization will be discussed later. In a metal, however, σ_{xy} is not quantized and the idea of Chern number be-

comes ill-defined. For example, in $TbMn_6Sn_6$, the anomalous Hall conductivity is approximately $0.1 \times (e^2/h)$ [43] in the metallic state, a value that is consistently supported by both direct experimental measurements and indirect estimates based on Berry curvature analysis. Effect of Berry curvature leads to various topological Hall effects [47, 51, 52] (e.g. anomalous, topological, spin) in quantum transport measurements, which remain consistent with the theory.

1.2.3 Weyl points in 3D kagome materials

Weyl points (WPs) [54, 55] refer to a special point in 3D Brillouin zone (BZ), where linearly dispersing bands touch each other at a point. First discovered by angle-resolved photoemission spectroscopy (ARPES) in TaAs semimetal [56], the low-energy excitations near WP resemble the chiral Weyl fermions [57] in high-energy physics, which justifies the name. Similar to Weyl fermions, the WPs are chiral in nature, and always come in pairs [58] with either left- or right-handed chirality. Existence of WP requires either broken TRS or inversion symmetry, which gives rise to finite BC in the system. In practice, this can be achieved in 3D systems with FM and SOC [see Fig. 1.5]. WPs carry a topological charge, and their gaplessness is protected by symmetry, unlike DPs in Graphene. The manifestation of their topology can be seen in a special surface state, known as Fermi arcs [56, 59], which connects two WPs by a line.

Although some kagome lattices appear to exist in bilayer forms, most kagome materials are three-dimensional. For a long time, kagome materials Mn_3X (X=Sn, Ge) [60–63] and $Co_3Sn_2S_2$ [64–66] are known to host WPs. ARPES shows topological surface states [53] of $Co_3Sn_2S_2$ in Fig. 1.5(b). While $Co_3Sn_2S_2$ is a out-of-plane ferromagnet [67], Mn_3X is known to host noncollinear antiferromagnetism [68]. The magnetic ordering breaks TRS and strong interlayer coupling provides the 3D bulk character – this fulfils the criteria to obtain WPs, as predicted by theoretical calculation [69]. On

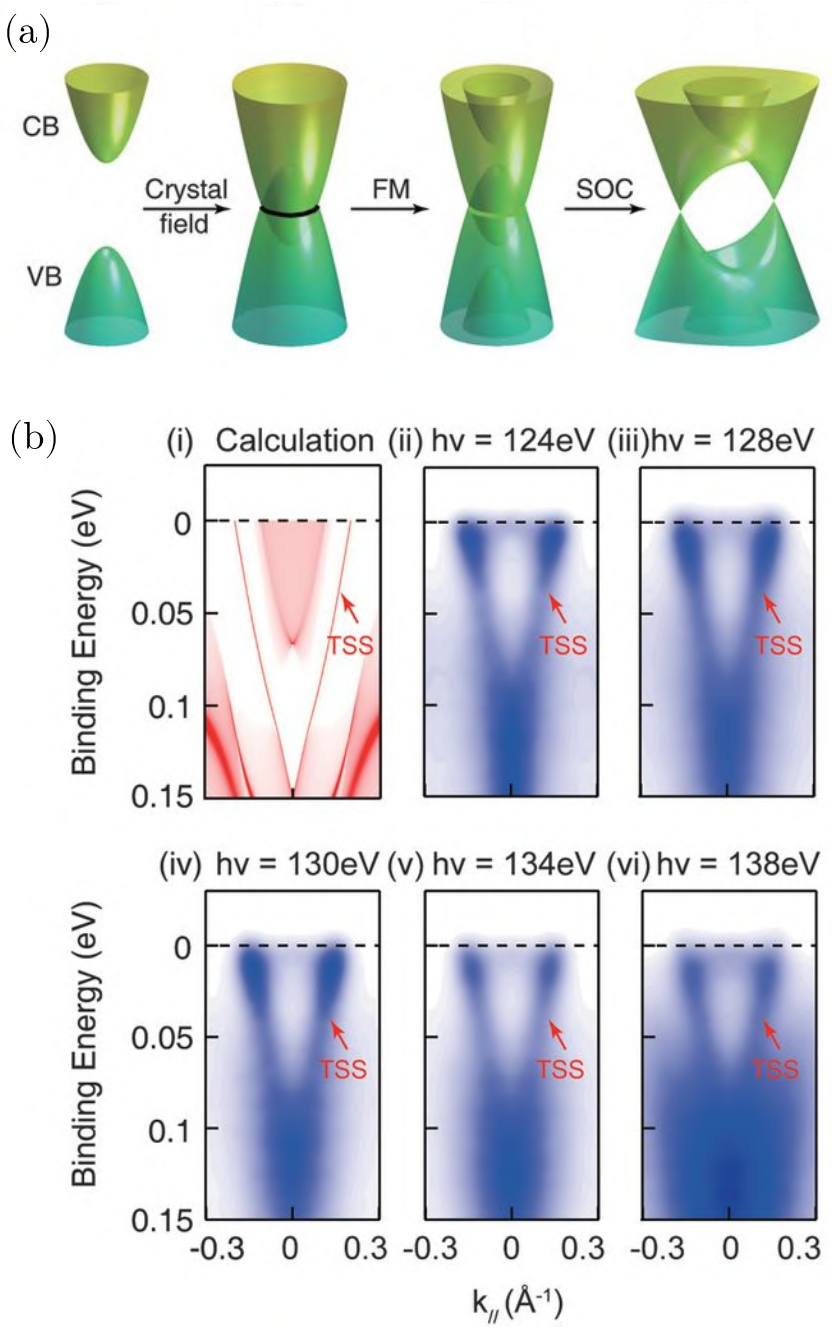

Figure 1.5: (a) Schematic dispersion for generating magnetic Weyl semimetals. (b) Theoretical (i) and experimental (ii-vi) slab spectra of kagome Weyl semimetal $Co_3Sn_2S_2$ along (001) surface. Adapted from Ref. [53].

the experimental front, both materials are reported to exhibit negative magnetoresistance [65, 70] in transport measurements, which happens due to chiral anomaly [63], a phenomenon exclusive to WP. Another indirect signal of WP is the giant or large AHE as seen in $Co_3Sn_2S_2$ [66], which is facilitated by broken TRS and concentrated BC near Weyl point crossing. Other experimental probes for WP include mapping of linear dispersion [71] around the Weyl crossing by ARPES and imaging the Fermi arc [72].

1.2.4 Breathing distortion

An interesting variation of the kagome lattice is where the inversion symmetry of upper and lower corner-sharing triangles are broken via trigonal distortion. This is termed a breathing kagome lattice [73], where the "breathing" pattern comes from expansion of one set of triangles while other contracts [see Fig. 1.6(a)]. This modifies the electronic structure by introducing anisotropic hoppings. The anisotropy hopping breaks the C_3 symmetry of the original kagome lattice, splitting the hopping amplitudes into two groups: t_1 and t_2.

Theoretical calculation [75] predicts that breathing anisotropy can stabilize a gapped $\mathbb{Z}_2$ spin liquid as the ground state of the pyrochlore lattice. Electronically, such distortion is predicted [76] to open a gap at the DP. Furthermore, if extrinsic or intrinsic SOC is present, the quadratic band touches the point between dispersing band and flat band (FB) at Γ opens up, resulting in a weakly dispersing (nearly) FB. FBs refer to energy bands in a material that remain nearly constant across momentum. Their flat character quenches kinetic energy and enhances interaction effects, which often give rise to phenomena like magnetism or superconductivity. Here, the weakly dispersing band becomes topological in presence of SOC, and lies far away from other bulk bands. This can be a route to produce tunable isolated topological bands. Additionally, breathing distortion can also be used to generate higher-order topological

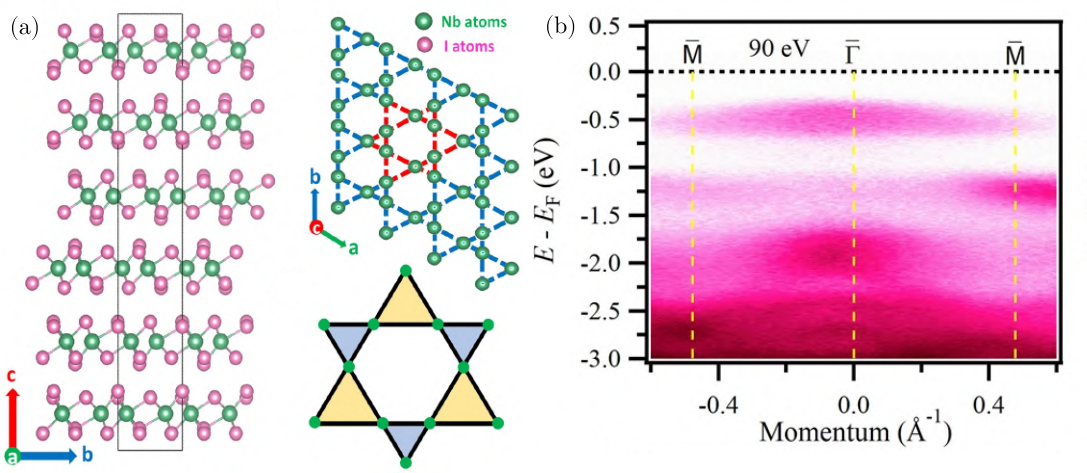

Figure 1.6: (a) Crystal structure of breathing kagome material Nb_3I_8. Breathing asymmetry distorts upper and lower triangle plaquettes of kagome lattice. (b) ARPES data of Nb_3I_8 shows a weakly dispersing flat band around 500 meV. Adapted from Ref. [74]

insulator (HOTI) [77], where corresponding in-gap states localize at the corner of the finite sample. It has been shown [78] that tuning of anisotropic hopping ratios (t_1/t_2) shifts the Wannier centres from the center to the corner of the triangles, leading to topological quadrupole moments. Quadrupole moments are a signature of HOTIs. HOTIs are materials where the usual conducting states do not appear on surfaces but instead on edges or corners of the material. In general, for a d-dimensional system, conventional topological insulators host states in $d-1$ dimensions, while HOTIs shift these states to $d-2$, $d-3$, or even lower-dimensional boundaries. However, the topological robustness of such HOTIs is yet to reach a consensus [79].

Experimentally, HOTIs are reported in phononic kagome crystal [80] with broken C_3 symmetry. Among conventional materials, the semiconductor family Nb_3X_8 (X=Cl, Br, I) is well-known for its breathing kagome geometry of Nb atoms. Spectroscopic measurement [74] shows the predicted flat and weakly dispersing bands around 500 meV energy [see Fig. 1.6(b)]. The topological phases of breathing kagome lack direct smoking gun evidence, as no "band inversion" is observed for the isolated bands around 500 meV. Here the "band inversion" [81–84] refers to the inversion of

conduction and valence bands, and is a routine method to detect non-trivial bands of a topological insulator.

1.2.5 Complex magnetic order and Kondo behavior

The novel magnetic states on kagome lattice have been an active pursuit for a long time. As a whole, the magnetic order is influenced by geometric frustration, SOC, and itinerant electron behavior. The frustration leads to a highly degenerate classical ground state in the case of localized spins, which can stabilize magnetic phases such as quantum spin liquid [85, 86], non-collinear spin texture [87], and chiral spin states [88]. In insulating kagome materials such as Herbertsmithite $ZnCu_3(OH)_6Cl_2$, no long-range magnetic order is observed [89] down to low temperatures despite strong AFM interaction, which provides strong evidence for a quantum spin liquid ground state. On the other hand, Dzyaloshinskii–Moriya interaction favors non-coplanar magnetic texture [43] that can carry finite scalar spin chirality [90]. Such non-coplanar order leads to anomalous Hall effect in Mn_3Sn [60]. The frustration can be lifted by FM ordering [91] or breathing distortion [92], which can stabilize collinear [65] or Néel type orders, while still hosting unusual excitations like magnon bands [93] with topological character.

Another interesting aspect is the Kondo effect [94] in kagome lattices. Kondo-like behavior emerges when localized magnetic moments (often from 4f orbitals) couple to conduction electrons. These conduction electrons, originating from multiple dispersive bands, hybridize with the local moments to form many-body singlets that screen the moments. However, the FBs remain largely insensitive to screening despite enhancing local moment fluctuations due to their localized character. Consequently, a selective Kondo screening is predicted [95], where sites contributing to the FB resist singlet formation, similar to what is observed for Lieb lattice [96].

In most 166 compounds, the highly localized 4f bands lie mostly away from the Fermi level, but Ce and Yb variants stand out due to proximity of 4f bands near the Fermi level [97]. A possible hybridization of 4f bands makes them a good candidate for Kondo-like behavior. Promising results can be seen in $CsCr_3Sb_5$ [98], where logarithmic temperature dependence of resistivity and ultra-low carrier density with cooling typically hints towards a Kondo-like behavior. Another quite recent study claims Kondo physics in a kagome AFM $La(Cu_xNi_{1-x})_7$. Surprisingly, the system lacks 4f electrons, and the Kondo physics may arise from effective localized moments of loop currents that originate from 3d orbitals.

1.3 Aim and organization of the thesis

Kagome lattice can be imagined as a cousin of the honeycomb lattice (e.g., graphene), which shares the same hexagonal unit cell and offers nearly similar electronic bands. Recent experiments have established that the kagome lattice exhibits a plethora of electronically rich and complex phenomena. We are interested in understanding how such bulk effects in the 2D limit influence states at the boundary, which are known as edge states. Historically, some of these phenomena, such as magnetism and SOC, have been shown to strongly affect the physics of edge states, making the kagome lattice a promising candidate.

The study of edge states can be important from several angles. First, nanoribbon character may produce wildly different electronic and magnetic properties. In fact, this is already well-known in graphene, where zigzag nanoribbons consistently exhibit metallic character with edge magnetism. If the nanoribbon is cut slightly differently, for example, in an armchair fashion, these qualities either change or vanish completely. The effects of such mechanical termination are not well known in the kagome lattice. Secondly, once edge states are well understood in nanoribbons, a practical question arises: how robust or fragile are these states for actual device

applications? This robustness is more fundamental and universal, relying on bulk order and Hamiltonian symmetries rather than chemical details. A possible route to realizing robust edge states is to engineer topological edge states, with the help of SOC and magnetic effects. Therefore, the thesis is motivated by the hypothesis that edge state characteristics in the kagome lattice strongly depend on the interplay between lattice termination, SOC, and magnetic order.

Specifically, we seek to address the following research questions:

- How does a **physical lattice termination** affect the existence, localization, and dispersion of edge states in kagome lattices?
- Can **SOC** effects lead to **topologically robust edge states**? If so, how does the interplay of SOC, lattice geometry, and magnetism modify these phases?
- In what ways do different types of **magnetic orderings** modify the topological edge states and their character?
- How can one quantify the **robustness of topological edge states** compared to ordinary states in a mathematically universal manner?
- What are possible ways to **detect topological edge states** in an experiment?

By systematically investigating these questions, this thesis aims to develop a comprehensive understanding of the factors that govern the topological landscape of kagome lattices. While analogous questions have been extensively studied in honeycomb lattices, similar studies for kagome lattices are sparse, which motivates the focused investigation in this thesis. The results are expected to advance the understanding of edge states and topological phases in kagome materials and may guide future design of materials and devices with tunable topological properties. We oraganize this thesis as follows.

First, we introduce the necessary concepts related to electronic models and topological band theory in Chapter 2. In this chapter, we explain the numerical tight-binding method, which we use to generate most of the results in this thesis. We begin discussing our results in Chapter 3, where we focus on pristine kagome edge states arising from lattice termination. After a review of Shockley states and graphene nanoribbon states, we write down the tight-binding Hamiltonian of the kagome lattice and show how to obtain the bulk and edge spectra in infinite and slab geometries, respectively. We then analyze how different terminations affect the edge dispersion in the kagome lattice.

We begin the discussion on topological edge states in Chapter 4. Here, we introduce the quantum spin Hall effect and the helical states that originate from it. We then introduce Kane–Mele SOC as a model for the quantum spin Hall effect and study its effect on the bulk and edge spectra. To this end, we compute the projected expectation value of the position operator and the spin polarization of the bands to understand the nature of the edge states. Furthermore, we analyze the topological nature of the bulk using Wilson loop analysis.

Chapter 5 focuses on chiral edge states arising from time-reversal-symmetry-broken bulk states. We explain the emergence of chiral edge states in the context of the quantum Hall and quantum anomalous Hall effects. We discuss both collinear ferromagnetic and non-collinear magnetic configurations, and analyze how Rashba and Kane–Mele SOCs tune the bulk and edge spectra. Finally, we conclude the thesis in Chapter 6.

The thesis is based on the work: arXiv:2602.12223 (2026). To study different electronic models within the tight-binding framework, a numerical toolkit was developed in parallel during the PhD. Majority of the code is written in Python, with occasional use of Fortran, and is hosted on GitHub (see github.com/z2gap/tbforge).

2 Theoretical concepts

2.1 Second quantization

Second quantization is an efficient way of describing a variable number of particles in an ensemble. During the first quantization, classical mechanics leads to the creation of quantum mechanics (QM), after which classical fields are quantized to obtain the quantum field theory (QFT). In first quantization, the particles are viewed as fundamental objects. However, a major consequence of QM is the indistinguishability of identical particles, which requires the wavefunction to be either symmetric for bosons

$$\psi_B(x_1, x_2) = \frac{1}{\sqrt{2}}[\phi_a(x_1)\phi_b(x_2) + \phi_b(x_1)\phi_a(x_2)], \tag{2.1}$$

or antisymmetric for fermions

$$\psi_F(x_1, x_2) = \frac{1}{\sqrt{2}} \begin{bmatrix} \phi_a(x_1) & \phi_b(x_2) \\ \phi_a(x_2) & \phi_b(x_1) \end{bmatrix}. \tag{2.2}$$

For a many-body state with a large number of particles, proper symmetrization/antisymmetrization can be tedious and difficult. This motivates the use of occupation number for describing a state in second quantization. Instead of tracking the individual wavefunctions, second quantization uses the creation ($a^\dagger$) and annihilation (a) operators to build the state. For instance, in case of a system with N sites, the

state can be described in terms of occupation number as $|n_1, n_2, ..., n_N\rangle$. Here, the creation and annihilation operators can act on the ith site as

$$\begin{aligned} a_i^\dagger |n_1, n_2, ..., n_N\rangle &= \sqrt{n_i + 1}\ |n_1, n_2, ..., n_i + 1, ..., n_N\rangle \\ a_i |n_1, n_2, ..., n_N\rangle &= \sqrt{n_i}\ |n_1, n_2, ..., n_i - 1, ..., n_N\rangle \end{aligned} \tag{2.3}$$

The operators follow different commutator algebras depending on the particle (boson or fermion). In specific, fermionic operators anti-commute: $\{c_{i\sigma}, c_{j\sigma'}^\dagger\} = \delta_{ij}\delta_{\sigma\sigma'}$ and bosonic operator commute $[b_i^\dagger, b_j] = \delta_{ij}$, which automatically takes care of the symmetrization/antisymmetrization for any arbitrary number of particles. This is useful for describing a many-body state in a compact manner.

2.2 Tight-binding model

Tight-binding (TB) [99] model provides an effective description of atoms in a crystal, which can be used to infer its electronic properties. It assumes that the electrons are tightly bound to the isolated atoms, and the electronic wavefunction is localized on the atomic site. The exponentially decaying nature of the wavefunction limits interaction with other sites, resulting in a wavefunction that is similar to the wavefunction of free electrons in that atomic orbital. Therefore, a reasonable ansatz for the wavefunction is the linear combination of atomic orbitals (LCAO) [100]

$$\psi_n(\mathbf{r}) = \sum_i c_{in}\phi_n(\mathbf{r} - \mathbf{R}_i), \tag{2.4}$$

where ψ_n refers to the wavefunction of nth atomic level, ith atomic orbital, described by ϕ_n, is centered at $\mathbf{R}_i$, and c_{in} are unknown coefficients. Plugging the wavefunction

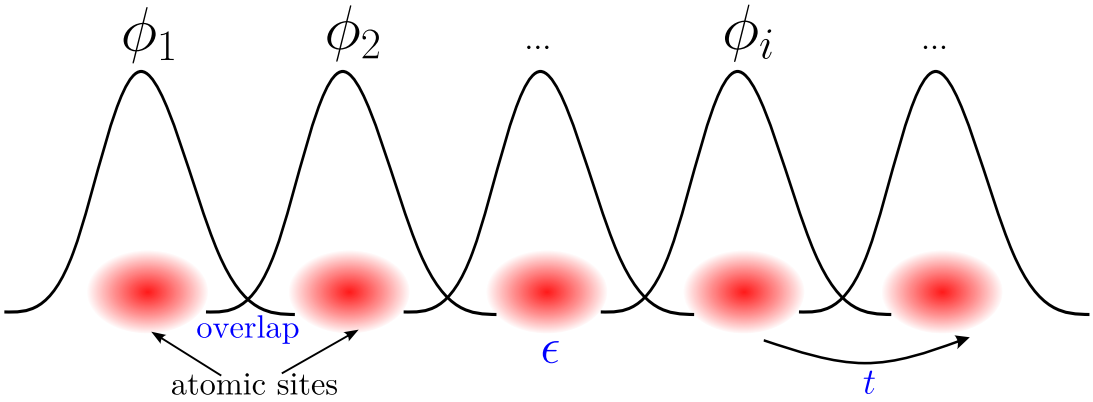

Figure 2.1: Figure illustrates the idea of tight-binding model. The atomic orbitals ϕ_i ($i = 1, 2, ...$) are approximated by localized wavefunctions centered around red atomic sites. Here, onsite potential is denoted by ϵ and t describes nearest-neighbor hopping.

into time-independent Schrödinger equation leads to

$$\begin{aligned} &\sum_j [H - E]\, c_{nj} |\phi_{nj}\rangle = 0 \\ \Longrightarrow &\sum_j \Big[\underbrace{\langle \phi_{ni} | H | \phi_{nj} \rangle}_{h_{ij}} - E \underbrace{\langle \phi_{ni} | \phi_{nj} \rangle}_{S_{ij}} \Big] c_{nj} = 0, \end{aligned} \tag{2.5}$$

where $|\phi_{nj}\rangle = \phi_n(\mathbf{r} - \mathbf{R}_j)$ is expressed in Dirac notation, h_{ij} is known as Hamiltonian matrix, and S_{ij} is called overlap matrix. If the basis is orthonormal, we can additionally have $S_{ij} = \delta_{ij}$, but this is not always guaranteed (like for atomic orbitals). At this point, we can invoke the periodicity of crystals to write a Bloch-like ansatz

$$\psi_n(\mathbf{r}) = \frac{1}{\sqrt{N}} \sum_i e^{-i\mathbf{k}\cdot\mathbf{R}_i}\, \phi_n(\mathbf{r} - \mathbf{R}_i), \tag{2.6}$$

where N is the number of atomic sites. It is easy to check the solution respects Bloch's theorem since $\psi_n(\mathbf{r} + \mathbf{T}) = \psi_n(\mathbf{r})$ for any translation vector $\mathbf{T}$. With this, we see the diagonal terms of h_{ij} become

$$\epsilon_n = \langle \phi_{ni} | H | \phi_{ni} \rangle. \tag{2.7}$$

This is typically called the "onsite potential". On the other hand, in the minimal single-orbital case, the off-diagonal term writes as

$$t_{ij}(\mathbf{R}_i - \mathbf{R}_j) = \sum_{ij} e^{-i\mathbf{k}\cdot(\mathbf{R}_i - \mathbf{R}_j)} \langle \phi_{ni} | H | \phi_{nj} \rangle. \tag{2.8}$$

Note that, this term is non-local, and can be viewed as electrons hopping from jth to ith site. Rightfully so, t_{ij} is called the "hopping matrix" [see Fig. 2.1]. The matrix elements of t_{ij} depend on the lattice and orbital configuration. Due to the exponential localization of wavefunction, mostly a summation up to the nearest-neighbor (NN) atomic sites is enough to capture the effective low-energy physics. This also helps the Hamiltonian matrix to remain sparse. However, in some cases (e.g. interlayer hopping in multilayer/moire structures), higher-order hopping terms might be necessary.

In general, t_{ij} is unknown for a given problem. A simple starting point is to consider NN unit hopping $t_{ij} = t = 1$, and tune other energy scales in terms of t. This is useful for a universal study of the lattice (say, kagome) properties without focusing on a specific material. From here on, different levels of modelling sophistication can be achieved based on the problem. For example, one can obtain hopping elements from *ab initio* data [density functional theory (DFT) +TB downfolding] to make electronic models more accurate. Alternatively, Slater-Koster (SK) [100] tight-binding method can be followed if the active orbitals are known. In the SK table, possible matrix elements are expressed in terms of direction cosines, which can be used to construct the hopping matrix elements.

In the language of second quantization, we can finally write the kinetic part of a general spinless Hamiltonian as

$$H_T = -\sum_{ij} t_{ij}\, c_i^\dagger c_j - \mu \sum_i c_i^\dagger c_i, \tag{2.9}$$

where $c_i^\dagger$ describes creation of electron at site i, t_{ij} is the hopping amplitude, and μ sets the chemical potential.

2.3 Magnetic texture and Zeeman effect

Electrons in real materials have spins, which often leads to a magnetic texture. In the TB framework, the magnetic texture [101] can be modelled as

$$H_{\text{mag}} = -J \sum_i \mathbf{m}_i \cdot \mathbf{s}_i, \tag{2.10}$$

where J denotes coupling exchange that is positive for ferromagnetic coupling and negative for antiferromagnetic coupling. The magnetic moments of localized spins are described by the unit vector $\mathbf{m}_i$, while

$$\mathbf{s}_i = \frac{1}{2} \sum_{\sigma\sigma'} c_{i\sigma}^\dagger \, \boldsymbol{\sigma}_{\sigma\sigma'} \, c_{i\sigma'} \tag{2.11}$$

is the spin operator described in terms of the Pauli matrices $\boldsymbol{\sigma}$.

If a system with a magnetic structure is placed under a uniform magnetic field, its energy levels split into several components. This happens due to the interaction between local magnetic moments and applied magnetic field. Originally discovered by Pieter Zeeman in 1896, the phenomenon is dubbed as the "Zeeman effect" [102, 103]. Quantitatively, the effect can be expressed as a perturbation due to the magnetic field $\mathbf{B}$

$$H = -\boldsymbol{\mu} \cdot \mathbf{B}, \tag{2.12}$$

where $\boldsymbol{\mu}$ is the magnetic moment of the atom. Neglecting the nuclear terms, μ can be written as $\mu \approx (\mu_B g J)/\hbar$, where μ_B is the Bohr magneton, g is the Landé g-factor, and J is the angular momentum of electrons.

We can write the Zeeman term for an out-of-plane magnetic field as follows

$$H_Z = h_Z(c^\dagger_{i\uparrow}c_{i\uparrow} - c^\dagger_{i\downarrow}c_{i\downarrow}), \tag{2.13}$$

where $\mathbf{B} = h_Z\hat{z}$ is the strength of the magnetic field along the z direction. The term is quite similar to local magnetic field if one sets $\sigma = \sigma_z$ in Eq. (2.11), except the field is uniform and externally applied. The Zeeman term decouples the spin sectors and lifts the spin degeneracy of the bands. It is an important term for designing spin-polarized states, quantum anomalous Hall insulators, and Majorana zero modes.

2.4 Spin-orbit coupling

Spin-orbit coupling is at the center of topological physics. SOC is a relativistic effect by which the magnetic moment of spin gets coupled to its orbital motion around the nucleus. More specifically, in an electron's rest frame, positive charges inside the nucleus moving in an orbit generate an effective magnetic field, which interacts with the electron's spin magnetic moment. The SOC Hamiltonian is given by

$$H_{\text{SOC}} = \lambda\mathbf{L}\cdot\mathbf{S}, \tag{2.14}$$

where $\mathbf{L}$ is the orbital angular momentum, $\mathbf{S}$ denotes spin angular momentum, and λ determines the strength of the coupling. The effect roughly scales with $Z^{2.4}$, so heavy atoms are expected to exhibit stronger SOC.

In crystals, the effect of SOC is multifold as it greatly tunes the electronic, magnetic, and topological properties of the materials. For example, SOC can modify bands through splitting or opening band gaps. Lifting of degeneracy is a useful step towards isolating states near the Fermi level. Such isolated states can be engineered to be topological (e.g. spinless SC state in 1D nanowire), or the coupling itself can produce protected edge states inside the gapped bulk (e.g. Kane–Mele

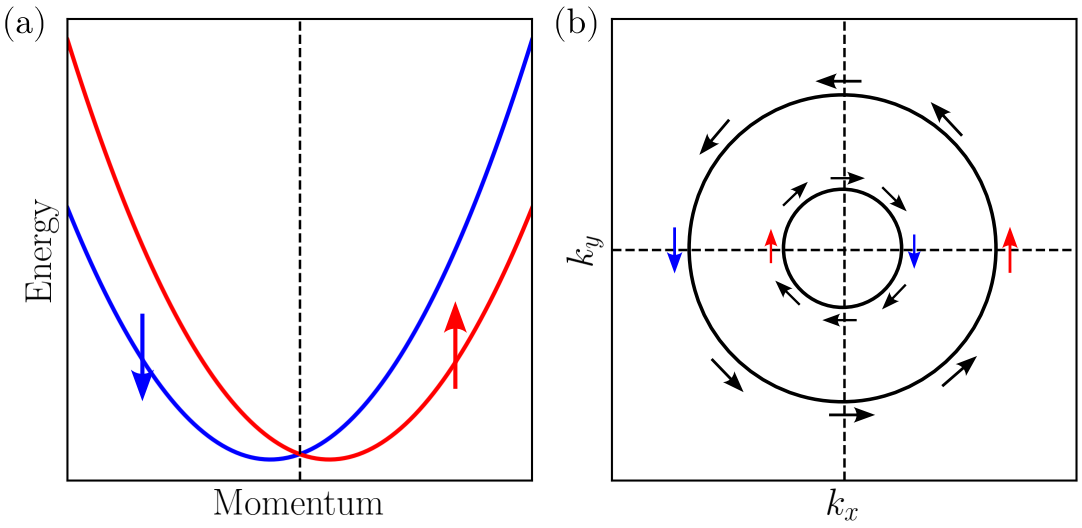

Figure 2.2: (a) The free electron dispersion under Rashba coupling exhibits splitting of bands. (b) Fermi contour illustrates momentum-dependent spin orientation and mixing of spins in a single band.

effect). Additionally, in some unconventional SC, SOC affects the pairing symmetry and stabilizes the exotic topological superconducting states.

The splitting of bands is explained by the Rashba model [104] of SOC (Rashba SOC, RSOC), which arises due to lack of inversion symmetry in materials (non-centrosymmetric, surface, interfaces). When an external electric field is applied perpendicular to the plane, an electron's motion couples to its spin, leading to the Rashba effect. The Rashba Hamiltonian on a TB lattice reads

$$H_R = i\lambda_R \sum_{\langle ij\rangle,\sigma\sigma'} c^{\dagger}_{i\sigma}(\boldsymbol{\sigma}_{\sigma\sigma'} \times \mathbf{d})_z \, c_{j\sigma'}, \tag{2.15}$$

where λ_R is the strength of the coupling, $\boldsymbol{\sigma}$ refers to vectors of Pauli matrices, $\mathbf{d} = \mathbf{r}_j - \mathbf{r}_i$ is the vector connecting NN sites, and $\langle ij\rangle$ implies the sum is restricted to NN sites only. It is easy to note from Eq. (2.15) that Rashba SOC mixes the spin sectors and S_z is no longer a good quantum number [see Fig. 2.2]. Rashba effect is known to produce "spin-momentum" locking, where spin orientation is locked to momentum direction. Writting the Rashba Hamiltonian in $\mathbf{k}$-space highlights the

coupling between spin and momentum

$$H_R(\mathbf{k}) = 2\lambda_R(\sin k_y \sigma_x - \sin k_x \sigma_y), \tag{2.16}$$

where spins have a helical texture $(\sin k_y, -\sin k_x, 0)$ in momentum space. In topological physics, breaking inversion symmetry is one way to generate Weyl semimetals. Therefore, Rashba-like SOC is a natural route to realize Weyl semimetals. Rashba SOC is also important in 1D Majorana nanowire setup, where it sets the stage by splitting the bands to artificially engineer topological p-wave SC.

Additionally, Kane–Mele SOC (KMSOC) [81] is another important factor in topological physics. It was originally proposed to model the quantum spin Hall (QSH) effect in graphene. The KM Hamiltonian is given by

$$H_{\mathrm{KM}} = i\lambda_{\mathrm{KM}} \sum_{\langle\langle ij\rangle\rangle,\sigma\sigma'} \nu_{ij}\, c^{\dagger}_{i\sigma}\sigma^{z}_{\sigma\sigma'}c_{j\sigma'}, \tag{2.17}$$

where $\langle\langle \ldots \rangle\rangle$ denotes sum over next-nearest neighbor (NNN) sites, λ_{KM} is the strength of SOC coupling, and ν_{ij} is a hopping-dependent factor that takes either 1 or -1 depending on whether hopping $j \to i$ is anticlockwise or clockwise, respectively. If hopping crosses an intermediate site 0 while going from j to i then $\nu_{ij} = (2/\sqrt{3})(\hat{\mathbf{d}}_{j0} \times \hat{\mathbf{d}}_{0i})_z$ with $\hat{\mathbf{d}}_{ab}$ representing unit vector connecting a and b sites. It may seem that this type of chiral term breaks TRS; however, TRS is preserved since spin up and down channels have opposite chiralities. This follows from σ_z factor, which corresponds to third Pauli matrix acting on spin sector. We will revisit this term later and explain its electronic properties.

2.5 Topological band theory

Topological band theory (TBT) [105] is a framework for understanding phases of matter that cannot be classified solely by conventional order parameters. It goes beyond the Landau framework, which relies on local order parameters and spontaneous symmetry breaking. In the Landau picture, phases are distinguished by the presence or absence of symmetry breaking, characterized by local observables such as magnetization, density waves, or superconducting order parameters. Here, phase transitions are typically understood as the emergence or disappearance of such local order, often accompanied by symmetry changes in the Hamiltonian.

In contrast, TBT emphasizes that certain phases of matter cannot be distinguished by any local order parameter. Instead, these phases are distinguished by global, non-local properties of the electronic wavefunctions defined over BZ. These properties are encoded in mathematical objects known as topological invariants.

The central idea of TBT comes from geometric structure of the Bloch wavefunction. In a crystal, electrons described by Bloch's theorem, posses energy eigenvalues $E_n(\mathbf{k})$ and corresponding Bloch eigenstates $|u_n(\mathbf{k})\rangle$. Evolution of $|u_n(\mathbf{k})\rangle$ across momentum space acquires a geometric phase and is connected to problem of parallel transport in differential geometry. The variation of $|u_n(\mathbf{k})\rangle$ defines a vector bundle over the BZ, and different phases correspond to inequivalent topological classes of such bundles. Therefore, we say two bands belong to the same "topological phase" if and only if their wavefunctions can be continuously deformed into one another without closing the bulk energy gap. An important consequence of topological bulk is the emergence of protected edge states, which follows from the bulk–boundary correspondence [106].

2.5.1 Connection to topology

The concept is analogous to topology [107], a branch of mathematics which studies how geometric objects remain invariant under continuous deformations such as stretching, twisting, and bending. In topology, objects are typically assigned an integer called “topological invariant" that acts as a label of the topological class. One such invariant is the “genus" g, which counts the number of independent “handles" or simply “holes" in an object. Objects in a similar topological class can be smoothly deformed into one another without processes like tearing or glueing. With such classification, while a cup and obwarzanek both have $g = 1$, and thus belong to same topological class [see Fig. 2.3]. But, a pretzel with $g = 3$ is topologically distinct from these two. A more direct relation between geometry and topology comes from the Gauss-Bonnet theorem [108], which relates local geometric curvature to a global topological integer. In the simplest form, the Gauss-Bonnet theorem reads

$$\int_S K\, dA = 2\pi\chi, \tag{2.18}$$

where K is the Gaussian curvature, dA is the surface element, and χ refers to an invariant called Euler characteristic. While genus is linked to “holes", Euler characteristic is useful for higher-dimensional manifolds and more abstract settings. Notably, these are connected as $E = 2 - 2g$. What is remarkable is that, such abstract concepts of topological invariants are incredibly useful for classifying states of matter. In fact, condensed matter physics has its own set of topological invariants, which we will discuss later.

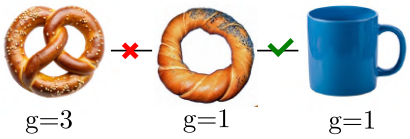

Figure 2.3: Comparison of genus g shows that obwarzanek and cup are topologically equivalent since both have $g = 1$, whereas pretzel with $g = 3$ belongs to a different topological class.

2.5.2 Accidental degeneracies

From concepts of topology, it is obvious that band-touchings are central to topological phases of matter. In solids, degeneracy in energy can occur due to symmetry of lattice space groups. However, bands can also cross simply due to tuning of Hamiltonian parameters. This is known as “accidental degeneracy". We can see this by considering a two-band model, which can be expressed in terms of Pauli matrices $\sigma_{x,y,z}$

$$H_{\text{2-band}}(\mathbf{k}) = d_1(\mathbf{k})\sigma_x + d_2(\mathbf{k})\sigma_y + d_3(\mathbf{k})\sigma_y. \tag{2.19}$$

Here, $d_i(\mathbf{k})$ are functions that contain Hamiltonian parameters. The important question here is how many parameters need to be tuned at a minimum to realize band degeneracy? Even though intuitively it may seem possible to tune one parameter and make energy levels meet, the answer is non-trivial. To show this, we write the eigenenergies of the Hamiltonian

$$E_{\text{2-band}}(\mathbf{k}) = \pm\sqrt{d_1^2(\mathbf{k}) + d_2^2(\mathbf{k}) + d_3^2(\mathbf{k})}. \tag{2.20}$$

From this expression, it is easy to follow that band degeneracy or $\Delta E_{\text{2-band}}(\mathbf{k}) = 0$ requires

$$d_1(\mathbf{k}) = d_2(\mathbf{k}) = d_3(\mathbf{k}) = 0. \tag{2.21}$$

That is, three independent terms need tuning for degeneracy to appear, as long as there is no other symmetry at play.

Such accidental degeneracies are special in TBT since they often signal a change in band topology, where Hamiltonian takes a universal form and becomes independent of microscopic details. A prototypical example is a linear band crossing in 2D, where

a low-energy Hamiltonian near the degeneracy point $\mathbf{k}_0$ can be expanded as

$$H_{2D}(\mathbf{q}) \approx q_x\sigma_x + q_y\sigma_y \quad \text{with } \mathbf{q} = \mathbf{k} - \mathbf{k}_0. \tag{2.22}$$

The spectrum of such system $E_{2D}(\mathbf{q}) = \pm\sqrt{q_x^2 + q_y^2}$ is doubly degenerate at $\mathbf{q} = 0$ and resembles physics of Dirac cones. The band degeneracy remains protected as long as no perturbation proportional to σ_z appears. Perturbations of such types $H' = m\sigma_z$ (m = constant) are known as “mass term", which can change band topology by gapping out the spectrum.

In 3D, such perturbations are not possible since there are three crystal momentum axes, and thus, solving three equations in Eq. (2.21) gives isolated points. Perturbations such as $m\sigma_z$, which could gap out the spectrum, now only shift the degeneracy points and one typically needs higher degrees of freedom to induce a gap opening. This is analogous to point nodes in Weyl semimetals, where degeneracy is protected.

2.5.3 Symmetries of Hamiltonian

Finally, we would like to mention about fundamental symmetries [109] of the Hamiltonian that are important for classifying states of matter. There are mainly three important symmetries: time-reversal ($\mathcal{T}$), particle-hole ($\mathcal{P}$), and chiral (S). We describe each of them below.

Time-reversal symmetry: Time-reversal symmetry, as the name suggests, describes invariance under reversal of time $t \to -t$. For spin-1/2 systems, it is defined by the antiunitary operator $\mathcal{T} = i\sigma_y K$ satisfying $\mathcal{T}^2 = \pm 1$, where σ_y is second Pauli matrix and K refers to complex conjugation. For an electron described by a Hamiltonian

$H(\mathbf{k})$, TRS requires:

$$\mathcal{T}H(\mathbf{k})\mathcal{T}^{-1} = H(-\mathbf{k}). \tag{2.23}$$

The above expression suggests that under reversal of time, a particle should retrace itself $\mathbf{k} \to -\mathbf{k}$. It is worthy to mention that any type of magnetic field breaks TRS. This is easy to make sense of with a hand-waving argument. Consider an electron (of charge e and mass m) moving in an external field $\mathbf{B}$ with velocity $\mathbf{v}$, then its equation of motion is governed by Lorentz force: $m\dot{\mathbf{v}} = -e\mathbf{v} \times \mathbf{B}$. Notice that the force changes sign under time reversal, because $\mathbf{v} \to -\mathbf{v}$ while $\mathbf{B}$ remains the same. In practice, TRS enforces pairing between states at $\pm\mathbf{k}$ and guarantees a special type of protected edge states. We will discuss these states later in detail.

Particle-hole symmetry: Particle-hole symmetry (PHS) is natural to superconducting systems, which are described by Bogoliubov–de Gennes (BdG) Hamiltonians. In superconductors, Bogoliubov transformation doubles the Hilbert space by generating a hole for every particle. PHS relates particles and holes via an antiunitary operator $\mathcal{P}^2 = \pm 1$. The presence of the symmetry requires

$$\mathcal{P}H(\mathbf{k})\mathcal{P}^{-1} = -H(-\mathbf{k}). \tag{2.24}$$

An important result of this symmetry is that energy spectrum become symmetric ($E \leftrightarrow -E$). This is a powerful relation that give rises to concept of zero-energy Majorana modes, since zero-energy states can be their own particle-hole partners.

Chiral symmetry: Finally, chiral symmetry is a unitary symmetry S that combines both TRS and PHS such that $S = \mathcal{T} \cdot \mathcal{P}$. Any Hamiltonian that satisfies chiral symmetry must obey

$$SH(\mathbf{k})S^{-1} = -H(\mathbf{k}). \tag{2.25}$$

By virtue of chiral symmetry, one can express the Hamiltonian in an off-diagonal form. Chiral symmetry remains important in bipartite lattices (e.g. honeycomb lattice, Su-Schrieffer-Heeger model), where hoppings are between two sublattices.

It is possible to classify noninteracting fermionic Hamiltonians based on the presence or absence of discrete symmetries. In this framework, the time-reversal (TRS) and particle-hole (PHS) symmetry operators can each take values $0, +1$, or -1, while chiral symmetry is either absent (0) or present (1). These possibilities lead to exactly ten distinct symmetry classes. The foundational works of Altland and Zirnbauer [110] and later Kitaev [111] established a periodic table of topological phases based on these symmetries. In this classification, each symmetry class, in a given spatial dimension d, is characterized as either topologically nontrivial (with $\mathbb{Z}$ or $\mathbb{Z}_2$ invariants) or trivial. This is known as the “tenfold classification".

2.5.4 Berry curvature and Chern invariant

A central mathematical concept in TBT framework is the Berry phase [112], which arises when a quantum system is adiabatically transported in parameter space. Here, adiabaticity plays a crucial part, which ensures the Hamiltonian changes slowly enough so that the system remains in its instantaneous eigenstate up to a phase.

This idea of Berry phase was originally proposed by Michael Berry in 1984 [113]. In the context of crystalline solids, this parameter space is the BZ and the relevant states are the Bloch wavefuntions $|u_n(\mathbf{k})\rangle$. We can quantify Berry phase mathematically as follows.

Consider a closed path C in momentum space. As the electron moves in BZ and its crystal momentum $\mathbf{k}$ varies adiabatically along C, the Bloch state acquires a geomet-

ric contribution. This geometric phase is termed the Berry phase

$$\gamma_n[C] = \oint_C \boldsymbol{\mathcal{A}}_n(\mathbf{k}) \cdot d\mathbf{k}, \tag{2.26}$$

where $\boldsymbol{\mathcal{A}}_n(\mathbf{k}) = i\langle u_n(\mathbf{k})|\nabla_{\mathbf{k}} u_n(\mathbf{k})\rangle$ is the Berry connection. The expression in Eq. (2.26) indicates that Berry phase depends on geometry of the path and Bloch wavefunctions along it, instead of time taken to traverse the loop. However, Berry phase is not a gauge-invariant quantity. This is because Bloch states can be defined up to a phase factor: $|u_n(\mathbf{k})\rangle \rightarrow e^{i\phi(\mathbf{k})}|u_n(\mathbf{k})\rangle$. Under such transformation, the Berry connection changes as

$$\boldsymbol{\mathcal{A}}_n(\mathbf{k}) \rightarrow \boldsymbol{\mathcal{A}}_n(\mathbf{k}) + \boldsymbol{\nabla}_{\mathbf{k}}\phi(\mathbf{k}). \tag{2.27}$$

If the phase factor $\phi(\mathbf{k})$ shifts by integer multiples of 2π, notice that there is no change. Therefore, Berry phase depends on gauge but is invariant modulo 2π. A physically more meaningful and gauge-invariant quantity is given by local density of Berry phase. This is famously known as the Berry curvature

$$\boldsymbol{\Omega}_n(\mathbf{k}) = \boldsymbol{\nabla}_{\mathbf{k}} \times \boldsymbol{\mathcal{A}}_n(\mathbf{k}). \tag{2.28}$$

One may identify that the expression of Berry curvature is similar to magnetic field in classical field theory. Here, the only distinction is that Berry curvature lives in momentum space, whereas magnetic field is defined in real space. This coincidence comes from their gauge structure, where both are defined as a curl of gauge connection. In more precise terms, Berry curvature is, in fact, dual of magnetic field. We like to point out that expression in Eq. (2.28) contains derivative of a complex wavefunction, which makes it not suitable in numerical setting. A more numerics-

friendly expression is given by

$$\Omega_n(\mathbf{k}) = -\mathrm{Im} \sum_{m \neq n} \frac{F^{xy}_{mn}(\mathbf{k}) - F^{yx}_{mn}(\mathbf{k})}{[E_m(\mathbf{k}) - E_n(\mathbf{k})]^2} \tag{2.29}$$

$$\text{with} \quad F^{xy}_{mn}(\mathbf{k}) = \langle u_n(\mathbf{k}) | \partial_{k_x} H(\mathbf{k}) | u_m(\mathbf{k}) \rangle \langle u_m(\mathbf{k}) | \partial_{k_y} H(\mathbf{k}) | u_n(\mathbf{k}) \rangle.$$

The above expression denotes xy component of the abelian Berry curvature tensor. Here, $\{m, n\}$ and $\{x, y\}$ denote band and spatial indices, respectively and $E_n(\mathbf{k})$ is the energy of the nth band.

Now, since Berry curvature is similar to a magnetic field, it is possible to define a flux of the Berry field. In fact, this is a topological invaraint known as “Chern number" $\mathcal{C}$. Being a topological invariant, Chern number only takes integer values $\mathcal{C} = 0, 1, 2, ...$ Mathematically, it can be expressed as

$$\mathcal{C}_n = \frac{1}{2\pi} \int_{\mathrm{BZ}} \Omega_n(\mathbf{k})\, d^2k. \tag{2.30}$$

Chern invariant measures the total “flux" of Berry curvature through the BZ and can be understood as a winding number that counts how many times the Bloch wavefunctions wrap around the underlying parameter space. In topological classification of matter, a nonzero Chern number signals a non-trivial phase that cannot be smoothly deformed into a trivial insulator without closing the energy gap. This leads to important experimental consquence such as quantized Hall conduatnce, which we will discuss in more detail later.

3 Lattice-terminated edge states

3.1 Edge states arising from lattice geometry

3.1.1 Shockley states

Inside a perfect crystal, electrons experience a periodic potential generated by the repeating arrangement of atoms. This periodicity leads to the formation of energy bands described by Bloch's theorem. However, at the surface, the translational symmetry of the lattice is broken and the periodic boundary conditions are no longer satisfied. As a consequence, additional electronic states may appear that are localized near the surface, commonly referred to as "surface states". More formally, a surface state arises when the solutions of the Schrödinger equation inside the crystal and in the vacuum region can be matched continuously at the surface boundary.

The essential idea can be illustrated using a one-dimensional nearly free electron model [116, 117]. Consider a one-dimensional chain of non-interacting electrons with lattice periodicity a. The electronic states satisfy the Schrödinger equation

$$\Big[-\frac{d^2}{dz^2}+V(z)\Big]\psi(z)=E\psi(z). \tag{3.1}$$

Inside the crystal, the effective potential originates from the ion cores and can be approximated by a weak periodic potential of amplitude V_1, while outside the crystal,

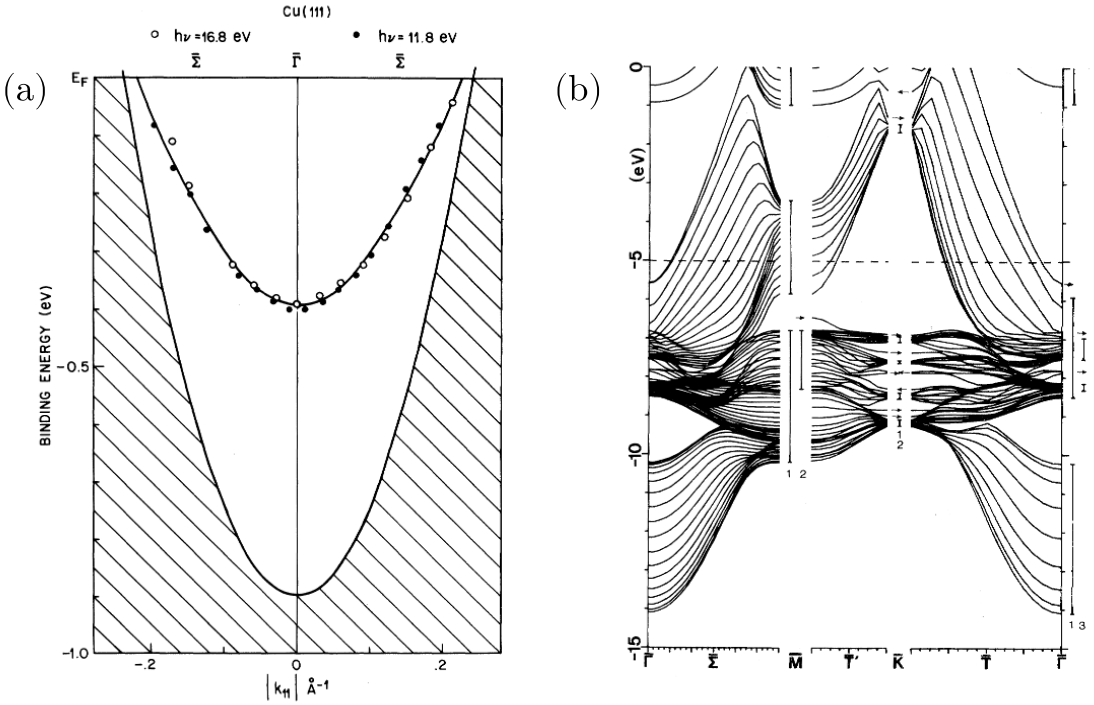

Figure 3.1: (a) ARPES spectrum of Cu(111) slab. Shaded areas denote continuous bulk bands and solid line refers to surface state (adapted from Ref. [114]). (b) Ab initio band structure of a six-layer Cu(111) slab. Here, vertical lines highlight bulk bands and arrows represent surface states (adapted from Ref. [115]).

the electron experiences a constant surface barrier V_0. Then we have

$$V(z) = \begin{cases} -V_0 + 2V_1 \cos(gz), & \text{inside crystal} \\ V_0, & \text{otherwise,} \end{cases} \tag{3.2}$$

where $g = 2\pi/a$ denotes to BZ length. For the periodic potential, the Schrödinger's equation can be solved by taking the ansatz: $\psi_k(z) = Ae^{ikz} + Be^{i(k-g)z}$. With this, the energies and wavefunctions are straightforward to obtain [116]

$$\begin{aligned} E(q) &= -V_0 + \frac{g^2}{2} + q^2 \pm \sqrt{(g^2q^2 + V_1^2)}, \\ \psi_k^b &= e^{iqz} \cos\left(\frac{gz}{2} + \delta\right), \end{aligned} \tag{3.3}$$

where $q = (k - g/2)$ measures the distance from BZ boundary and δ is the phase factor satisfying $e^{i2\delta} = (E - k^2)/V_1$. From this expression, we see two energy levels and the wavefunction is described by a propagating Bloch wave. The energy spectrum has a gap $\Delta E = 2V_1$ at BZ boundary $q = 0$. Interestingly, $E(q)$ in Eq. (3.3) allows imaginary values of q. When q is imaginary, the solution is given by a decaying evanescent mode

$$\psi_k^s = e^{-qz} \cos\left(\frac{gz}{2} + \delta\right). \tag{3.4}$$

Imaginary values of q are not allowed in the bulk since they violate periodic conditions. But they are completely fine at the surface because the wavefunction is matched with a decaying solution in the vacuum region

$$\psi_k^v = e^{-\sqrt{(V_0 - E)}z}. \tag{3.5}$$

If both the wavefunction and its derivative are continuous at the surface boundary, a localized solution can exist.

These solutions are called "Shockley states" [117]. They refer to a special type of surface states that arise from surface termination, and were first predicted by William Shockley in 1939. However, experimentally Shockley states were demonstrated much later on Cu(111) surface. Fig. 3.1(a) shows ARPES measurement of Cu(111) slab [114], where a surface state exists around $\bar{\Gamma}$ point. Independently, existence of surface state is also confirmed by ab initio calculation of a six-layer Cu(111) slab [Fig. 3.1(b)].

3.1.2 Graphene nanoribbons

A modern example of edge states appears in 2D graphene (or honeycomb) nanoribbons (GNR). Although several terminations are possible depending on the cut,

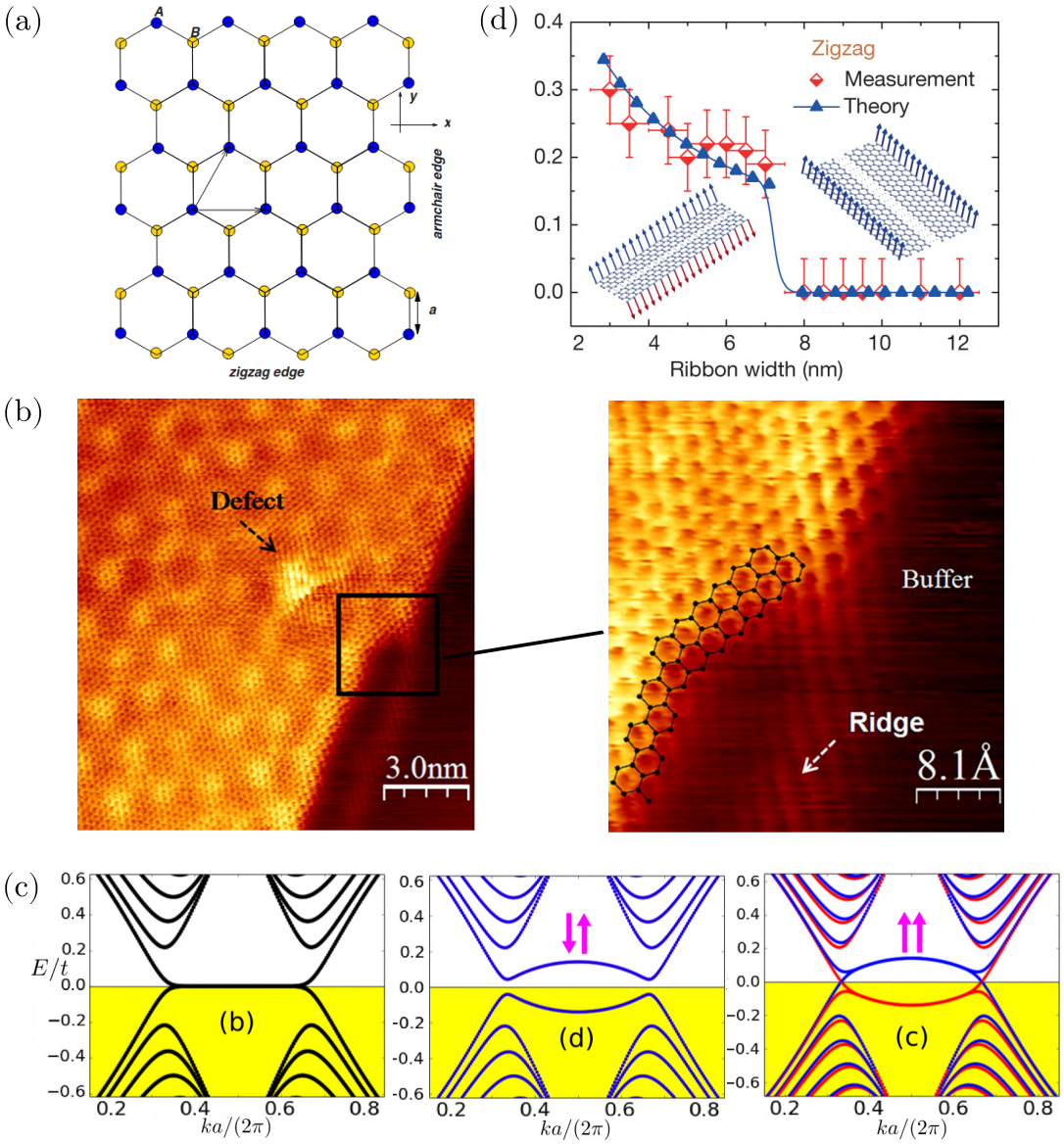

Figure 3.2: (a) Graphene nanoribbon with zigzag (top, bottom) and armchair (left, right) edges (adapted from Ref. [118]). (b) STM image of graphene/6H-SiC (left). Black square, zoomed on the right, illustrates armchair and zigzag edges (adapted from Ref. [119]). (c) Mean-field calculation of graphene nanoribbon with non-magnetic (NM), antiferromagnetic (AFM), and ferromagnetic (FM) order (adapted from Ref. [120]). (d) Bandgap obtained from tunnelling spectroscopy is plotted against ribbon width. Increasing width drives inter-edge AFM state into FM state (adapted from Ref. [121])

mainly two types of graphene nanoribbons [122, 123] are important: zigzag (ZGNR) and armchair (AGNR) [see Fig. 3.2(a)]. Techniques like epitaxy, lithography, and chemical etching routinely prepare these nanoribbons, which then can be probed by STM [see Fig. 3.2(b)] to estimate the nanoribbon type. Electronically, GNRs produce significantly different features – most calculations predict metallic behavior in ZGNR and quasi-metallic or semiconducting behavior in AGNR. Here, particularly interesting is the ZGNR, which famously host localized flat edge state at the Fermi level with no armchair analogue. This is due to sublattice termination of ZGNR. In other words, ZGNR edge always contains one sublattice with termination ending either at A or B sublattice, whereas AGNR mixes these sublattices [cf. Fig. 3.2(a)]. By virtue of this, ZGNR allows unique boundary conditions that permit evanescent edge solutions at $E = 0$ [124]. However, in practice, the system contains a small gap induced by magnetic order at the edge. This was predicted by DFT investigation [125], where a zero-energy state in nonmagnetic limit develops a finite gap in spin-polarized calculation. Consequently, a magnetic gap was demonstrated experimentally [121].

One of the most compelling features of ZGNR is the edge magnetism. Magnetic structure of ZGNR at the edge consists of two parts: FM order along edge and AFM coupling between edges. Without going into microscopic details, an overall understanding of magnetic behavior can be drawn from Lieb's theorem [126]. This theorem applies to bipartite lattice, and further states that ground state of half-filled Hubbard model has total spin $S = |N_A - N_B|/2$, with N_A and N_B referring to the number of sites belonging to each sublattice. Since pristine graphene has same number of A and B sites, magnetic order with zero net magnetization is expected from Lieb's theorem. Role of Coulomb term also helps in Stoner instability, where flat zero-energy states with a large density of states (DOS) drives FM order at the edges.

Nevertheless, strength of inter-edge AFM coupling is reduced in very wide ribbons

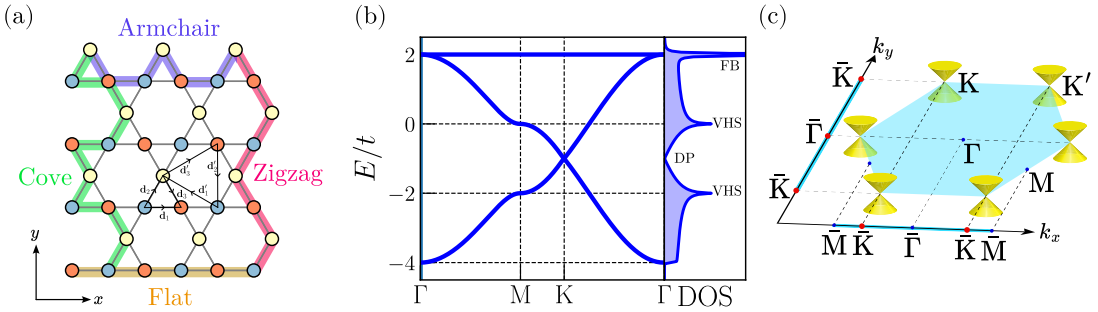

Figure 3.3: (a) Kagome lattice with three sublattice atoms (color-coded) per unit cell shows possible terminations via line cut. Nearest $\mathbf{d}_{1,2,3}$ and next-nearest neighbor $\mathbf{d}'_{1,2,3}$ vectors are marked by solid lines with arrows. (b) Bulk band structure and density of states (DOS) highlight Dirac point (DP) at K, Van Hove singularity (VHS) at M, and a flat band (FB) above the Fermi level. We keep the tight-binding parameter as $t = 1$ and $\mu/t = 0$. (c) 2D bulk BZ (blue hexagon) and the projected ribbon BZ version along k_x and k_y.

— in such limits, edge magnetic order becomes fully FM [121]. In fact, realization of a ground state with finite spin S is possible is several ways. One of them is to induce sublattice imbalance, which in practice, can be done by constructing nanoflakes [127] or introducing vacancies [128]. Alternatively, doping [129] or electric field [121] can push the system away from half-filling to realize finite spin magnetic order. Theoretical calculations based on mean-field Hubbard model predict edge magnetism for any $U/t > 0$ [120, 130], whereas bulk magnetization remains very small. A higher Hubbard parameter can, however, lead to bulk AFM order via Mott-Hubbard transition. Calculation at the mean-field level predicts this transition for around $U/t = 2.23$; however, quantum Monte Carlo forecasts a higher number [131]. Overall, mean-field results agree well with DFT results [132].

3.2 Kagome tight-binding model and bulk features

The kagome lattice is defined by the hexagonal basis with three sublattice atoms per unit cell. We illustrate the real space lattice in Fig. 3.3(a). The bulk crystal can be

constructed by simply repeating the three-sublattice unit cell across the real space. Furthermore, the lattice has point group symmetries similar to a triangular lattice, which includes C_6 rotation and mirror symmetry σ, making it fall under D_6 point group in two dimensions.

The bulk features of kagome bands can be extracted by constructing a TB model. Realistically, the TB model may have many inputs – multiple orbitals, magnetic structure, SOC, impurity, or interaction, depending on the material. However, the essential low-energy bulk physics can be accurately modelled from a minimal single-particle Hamiltonian with NN hopping and chemical potential. We write the kinetic Hamiltonian similar to Eq. (2.9)

$$H_T = -t \sum_{\langle ij \rangle} c_i^\dagger c_j - \mu \sum_i c_i^\dagger c_i. \tag{3.6}$$

Here, t denotes the NN hopping integral between NN sites i and j, and μ refers to the chemical potential. Although the hopping integral can potentially extend to higher-order neighbors, a NN hopping is sufficient here. We point out that t is also a scalar since we consider a single s-like orbital in our model for simplicity. Had we considered multiple orbitals, the hopping element would have been a matrix. Furthermore, real materials contain spin, but for now we omit the spin degrees of freedom since the bands we are interested in are spin-degenerate.

The kagome bands can be obtained by writing the TB Hamiltonian in reciprocal space. If we consider the basis $\psi_{\mathbf{k}} = [c_{\mathbf{k}A}, c_{\mathbf{k}B}, c_{\mathbf{k}C}]^T$, the Hamiltonian can be expressed as $H_T = \sum_{\mathbf{k}} \psi_{\mathbf{k}}^\dagger h_T(\mathbf{k}) \psi_{\mathbf{k}}$, where h_T is given by

$$h_T(\mathbf{k}) = \begin{bmatrix} h_{AA} & h_{AB} & h_{AC} \\ h_{AB}^* & h_{BB} & h_{BC} \\ h_{AC}^* & h_{BC}^* & h_{CC} \end{bmatrix}. \tag{3.7}$$

We notice that, although the Hamiltonian has nine terms, it is written in an upper

triangular form with six independent terms due to hermiticity. Here, h_{AA}, h_{BB}, h_{CC} correspond to the onsite potentials of sites, which can be set to μ. All the other terms correspond to hopping integrals. Consider $\mathbf{a}_1$ and $\mathbf{a}_2$ to be the hexagonal lattice vectors and δ_1, δ_2, and δ_3 as the vector connecting sites between A to B, B to C, and C to A, respectively such that

$$\mathbf{a}_1 = a\begin{bmatrix}1 & 0\end{bmatrix}, \quad \mathbf{a}_2 = a\begin{bmatrix}1/2 & \sqrt{3}/2\end{bmatrix}, \text{ and} \tag{3.8}$$

$$\delta_1 = \mathbf{a}_1/2, \quad \delta_2 = \mathbf{a}_2/2, \quad \delta_3 = (\mathbf{a}_1 - \mathbf{a}_2)/2. \tag{3.9}$$

This description enables us to write

$$h_T(\mathbf{k}) = \begin{bmatrix} -\mu & -2t\cos\tau_1 & -2t\cos\tau_3 \\ -2t\cos\tau_1 & -\mu & -2t\cos\tau_2 \\ -2t\cos\tau_3 & -2t\cos\tau_2 & -\mu \end{bmatrix}, \tag{3.10}$$

where we have used the identity $(e^{ix} + e^{-ix}) = 2\cos x$, and $\tau_i = (\mathbf{k}\cdot\delta_i)$ with $i = 1, 2, 3$. We can find out the analytic form of the band structure by exact diagonalization

$$E(\mathbf{k}) = 2t, -t[1 \pm \sqrt{3 + 2\cos k_x + 4\cos(k_x/2)\cos(\sqrt{3}k_y/2)}]. \tag{3.11}$$

Here we have set $\mu = 0$. We show the dispersion in Fig. 3.3(b). We plot the bands along the high-symmetry path Γ–M–K–Γ so it captures the essential features such as DP, Van Hove singularity (VHS), and FB. For example, the dispersive bands touch linearly at K point to create DPs at K/K′. The excitations around DP resemble the Dirac fermions [133] in high-energy physics, which were first observed [50] in graphene.

3.2.1 Van Hove singularity

There also exist two saddle points around M, which refer to the change of band curvature $\partial^2 E/\partial k^2$. Such inflection point leads to logarithmic divergence in DOS, which is known as van Hove singularity [134, 135] or simply VHS points. Unlike honeycomb lattice, where two VHSs are identical, the twofold VHS in kagome exhibits different properties [136] depending on whether they have pure (p-type) or mixed (m-type) sublattice character. The saddle points in band structure create flat or nearly flat regions in the Fermi surface, where opposite flat ends can be connected by a single wavevector $\mathbf{Q}$ [137, 138]. Known as "Fermi surface nesting" [139–141], this enhances the electronic susceptibility, and when paired with diverging DOS, can create several symmetric-breaking electronic instabilities. Such instabilities are key to realize exotic quantum phases like charge [139]/spin [142, 143]/pair [144] density wave, nematic/stripe order [145], loop current [146], and unconventional superconductivity [41, 147, 148].

3.2.2 Flat band

Lastly, the spectrum contains a flat band (FB) above the Fermi level. FBs are a popular playground to study correlation physics [149–152] – this is because flattening of the band quenches the kinetic energy ($\partial_k E \to 0$), rendering the potential energy (Coulomb energy in our case) to dominate the system. FBs famously occur in twisted bilayer graphene [153–155], where twisting two graphene layers at a small angle ($\sim 1.1^\circ$) produces a nearly flat band, and is intimately connected to the celebrated unconventional SC and correlated insulating phases. Contrastingly, FBs exist in a kagome lattice due to geometry and interference without needing extra effort. In fact, electron hopping amplitudes on the corner-sharing triangles interfere destructively [156, 157], and cancel each other, and as a result, the electrons become localized. Similar to VHS, FBs lead to a diverging DOS. Such a large number of

states is useful for electronic ordering. For example, according to the Stoner criteria [158, 159] $DOS(E_F)U > 1$, a large DOS can lead to ferromagnetism despite the interaction being weak $(U << 1)$. Additionally, the BCS theory [160] of superconductivity states that $T_c \propto \exp(-1/[DOS(E_F)U])$, and a large DOS can potentially enhance the T_c [161].

3.3 Pristine edge states in kagome lattice

In order to probe the edge state dispersion of kagome lattice, we need to consider the so-called “ribbon"0 or “slab geometry". It is extended in one direction (say along $i = x/y$), while the other direction is kept finite, similar to a ribbon. This ensures that the wavevector k_i remains a good quantum number along the extended direction, enabling the band structure to be computed while still capturing the influence of finite-size edge effects.

When the translation symmetry is lost due to finite edges, the bulk BZ (in 2D) reduces to the 1D projected BZ. We show this projection of BZ in Fig. 3.3(c). The bulk BZ is represented by the blue hexagon, where DPs are located at the corners. We see that depending on the projection axis (k_x or k_y), the reduced BZ has different periodicity. Additionally, the BZ along k_x contains two DPs with well-preserved valleys, whereas along k_y, there are three DPs, with K and K′ valleys mixed and one Dirac point coinciding with the Γ point. Even though the bulk bands are well-known, the projected bands can still create a non-trivial spectrum (presence or absence of gap, overlapping of special points) that requires careful inspection to understand the edge physics. During projection, bulk states form a continuum, and the edge states must lie outside this continuum for them to be identifiable. Otherwise, the edge states can hybridize with the bulk states, making it harder to be detected by STM reliably. Therefore, we aim to understand how specific lattice terminations project the bulk bands into the reduced Brillouin zone and, in doing so, generate

specific edge states (e.g. flat or dispersive) that lie in the gaps of the projected bulk continuum.

For this purpose, we consider terminations produced by line cuts on kagome lattice. Although the cuts may take any shape, we keep them linear for simplicity. This produces four types of terminations, as shown in Fig. 3.3(a). Out of these four, the zigzag and armchair terminations [122, 123] already exist in graphene, with different consequences on the localization and electronic properties. We analyze how this compares with the kagome lattice in the next parts. To do this, we introduce a variation of local density of states (LDOS). This is called momentum-resolved site LDOS [162, 163], which returns the site-resolved state distribution for a given momentum and energy. Since pristine kagome spectrum lack any global gap, we choose to show LDOS at a specific momentum. We can express the site LDOS as

$$\rho_i(E, k_a) = \sum_n |\psi_{in}(k_a)|^2 \, \delta[E - E_n(k_a)], \tag{3.12}$$

where E_n and ψ_{in} are the energy and wavefunction of the n-th state, i refers to the site index, and $a = x, y$ dummy index describes the axes. The delta function is approximated by the Lorentzian

$$\delta(x) \equiv \frac{1}{\pi}\Big(\frac{\epsilon}{x^2 + \epsilon^2}\Big), \tag{3.13}$$

with small smearing ($\epsilon = 10^{-3}$) for numerical convenience. In the expression of $\rho_i(E, k_a)$, typically we set E to the energy of edge states and pick a momentum k_a that maximizes edge-to-bulk bands ratio.

3.3.1 Terminations at fixed y: armchair and flat

As per Fig. 3.3(a), considering lattice terminations at fixed y produces armchair and flat terminations, with the latter being exclusive to the kagome geometry. For a

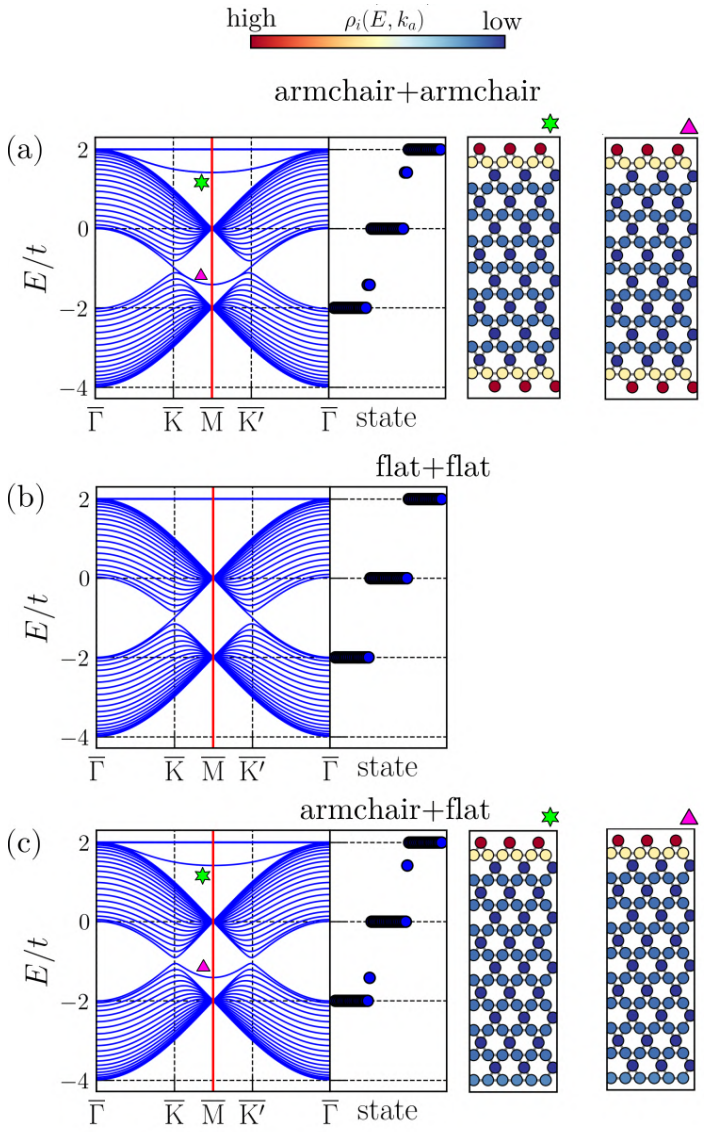

Figure 3.4: Kagome ribbon band structures for three types of terminations at fixed y: (a) armchair-armchair, (b) flat-flat, (c) armchair-flat (left). Solid red line highlights the momentum, where edge states are maximum relative to bulk. We plot the energy levels at this momentum against number of states (center). Same momentum is used to compute the corresponding site LDOSs $\rho(E, k_a)$, which are then projected on the real-space lattice (right). Icons relate site LDOS to edge states in the spectrum. The parameters are taken to be $t = 1$ and $\mu/t = 0$.

comprehensive analysis of the termination effect, we examine three possible edge scenarios: armchair, flat, and armchair-flat. At the same time, the length of the ribbon is kept long enough to prevent interactions between edge states from opposite sides. For the armchair termination, we find that the ribbon band structure hosts two edge states in the gap of bulk continuum. They are marked by triangular and star icons in Fig. 3.4(a). One of them connects DP from K to K', while the other lies in the vicinity of the FB. Next to the band structure, we show the energy levels at $\overline{\mathrm{M}}$ point, where edge states are clearly visible. Here, three continuous branches associated with the bulk bands appear, accompanied by two pairs of isolated in-gap edge states. The edge states are two-fold degenerate, while each of them contains a top and bottom mode. This is due to the mirror symmetry and a large slab length, which we address in Appendix A.

The LDOS of the edge states at M point reveals that the wave functions are strongly concentrated near the boundary. The LDOS is highest on edge sites with a coordination number of two, forming a distinct triangular plaquette pattern at the termination. Interestingly, the s-like electrons hopping around such chiral triangular motifs are predicted [164] to possess a finite orbital angular momentum (OAM). In the bulk, the OAM contributed by clockwise and anticlockwise triangles cancels out. But at the edge, this cancellation fails, which allows the edge states to carry nonzero OAM. Because OAM is linked to both rotational and translational motion, kagome edge states with finite group velocity $v_k = \partial_k E(k)$ may therefore play a role in orbitronic transport [165].

The picture changes entirely when both boundaries have flat termination, as illustrated in Fig. 3.4(b). In this case, the ribbon band structure closely resembles the bulk spectrum, and no edge states appear. Consequently, no LDOS is shown for this termination.

When two terminations are mixed, the mirror symmetry is broken. This is the case in Fig. 3.4(c), where lower and upper terminations are flat- and armchair-like,

respectively. The resulting edge mode resembles that of a fully armchair-terminated ribbon. The only contrasting part is that, due to the loss of mirror symmetry, states are no longer two-fold degenerate. In fact, the LDOS distribution shows that all surviving edge states are localized on the armchair boundary, while the flat edge does not support edge-localized eigenstates.

3.3.2 Terminations at fixed x: zigzag and cove

We now turn to the discussion of terminations at fixed x, which yields zigzag- and cove-like terminations. Similar to the previous section, we examine three possibilities: zigzag, cove, and a mix of zigzag and cove terminations. To probe their effect on the electronic spectrum, we impose periodic boundary conditions along the y-axis while keeping the system finite along x.

The band structure for a pristine zigzag edge is shown in Fig. 3.5(a). For such termination, three DPs appear at the projected $\overline{\mathrm{K}}$, $\overline{\mathrm{K}}'$, $\overline{\Gamma}$ points. The DP at $\overline{\Gamma}$ originates from the folding of the $\overline{\mathrm{K}}$ onto $\overline{\Gamma}$ under the chosen slab BZ. This can be understood more clearly from the BZ diagram in Fig. 3.3(c). We point out that such overlapping is missing for edges along y direction. This illustrates how lattice termination can reshape the projected band structure, and thus modify the hybridization of states at $\overline{\Gamma}$ with perturbations such as substrates or impurities. This factor can be crucial for designing controlled heterostructures.

Nevertheless, the zigzag spectrum [see Fig. 3.5(b)] hosts two well-defined edge modes: one near DP and the other near FB. Furthermore, the LDOS shows that the edge states appear at opposite sides of the slab and remain degenerate due to mirror symmetry. Depending on the chosen energy, the LDOS pattern displays a characteristic phase shift: the maximum weight sits either on sites with a coordination number of two or four. In contrast to the zigzag case, the cove spectrum

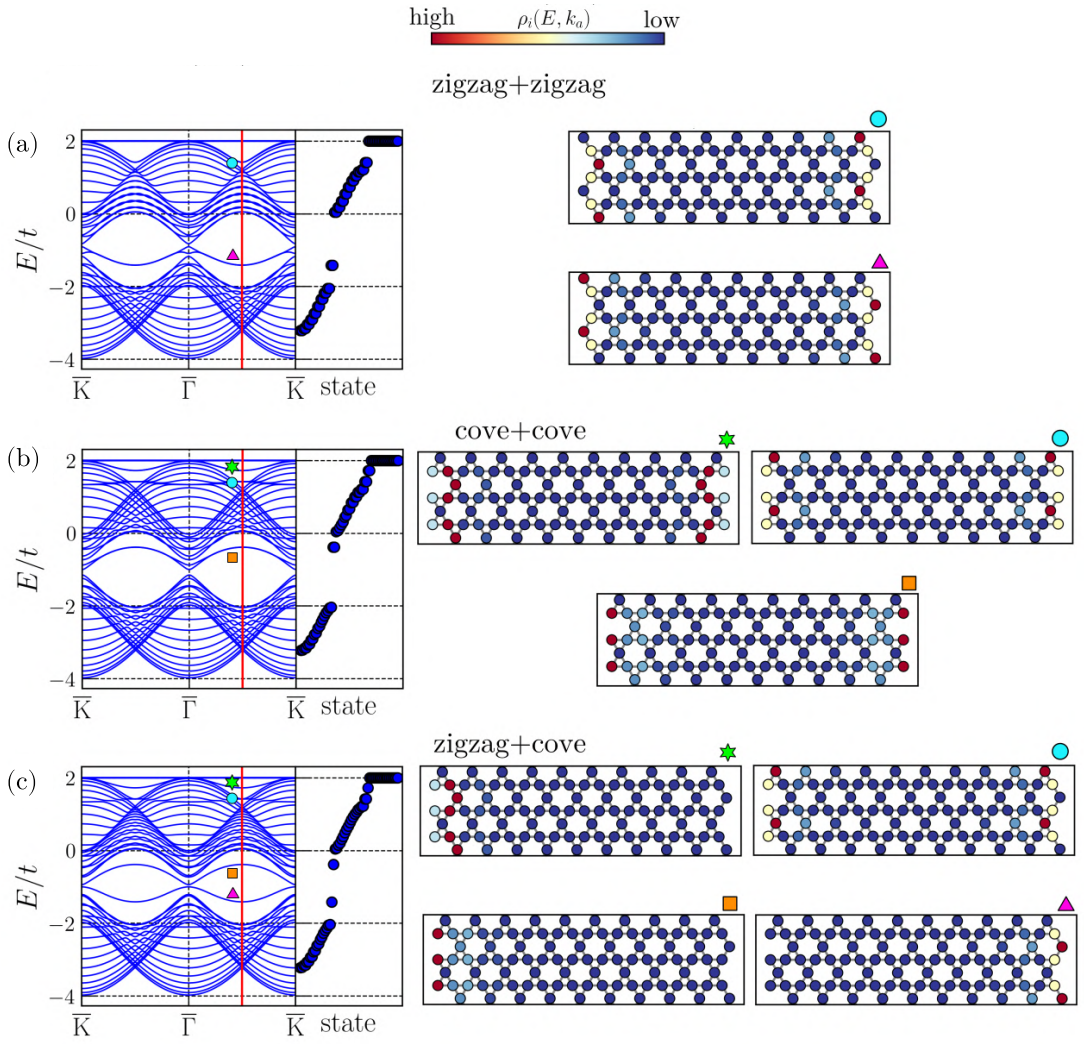

Figure 3.5: Kagome ribbon band structures for three types of terminations at fixed x: (a) zigzag-zigzag, (b) cove-cove, (c) zigzag-cove (left). Solid red line highlights the momentum, where edge states are maximum relative to bulk. We plot the energy levels at this momentum against number of states (center). Same momentum is used to compute the corresponding site LDOSs $\rho(E, k_a)$, which is then projected on the real-space lattice (right). Icons relate site LDOS to edge states in the spectrum. The parameters are taken to be $t = 1$ and $\mu/t = 0$.

contains non-degenerate edge states; in fact, only one edge state (marked by circle) retains degeneracy, whereas the remaining edge states are non-degenerate. The LDOSs reveal that although all edge states remain localized, their spatial patterns differ subtly. States near zero energy occupy dangling sites with reduced coordination, which is consistent with the behavior of localized boundary modes discussed earlier. Higher-energy states, however, prefer to reside on fully coordinated edge sites (four NNs), suggesting the boundary geometry controls not only the existence of edge modes but also their microscopic weight distribution.

Finally, the hybrid edge containing zigzag on one side and cove on the other naturally inherits features from both terminations. The resulting spectrum in Fig. 3.5(c) contains all edge states characteristic of zigzag and cove boundaries, giving rise to a total of five edge modes. Among these, only one state (highlighted by circle) is two-fold degenerate and localizes on both edges of the slab. In contrast, other edge states localize only on one side of the slab.

4 Kagome quantum spin Hall effect

4.1 Quantum spin Hall effect

Quantum spin Hall (QSH) effect is a type of Hall effect that occurs without a magnetic field. QSH effect is observed in 2D topological insulator (TI), a type of insulator similar to an ordinary insulator with gapped bulk. What sets TI apart is that it is characterized by a topological invariant, leading to gapless boundary modes protected by symmetry. For QSH insulators, the boundary modes are known as helical edge states, which are a pair of spin-polarized edge states that circulates an insulating bulk. The hallmark of QSH effect is that, unlike pristine edge states, helical edge states are topologically protected by time-reversal symmetry (TRS). This special immunity can be understood from Kramer's theorem [166]. In systems with half-integer spin, TRS leads to the formation of Kramer's pair, where each state has a TRS partner with same energy but with opposite spin and momentum. That means, under any TRS-preserving perturbation (e.g. non-magnetic impurity), an electron with specific spin cannot change its direction, which prevents "backscattering" between right- and left-moving edge channels. This topological aspect gives rise to quantized Hall effect, where Hall conductance is given by an integer topological invariant and a constant factor of $2e^2/h$.

QSH effect was first experimentally demonstrated in HgTe/CdTe quantum wells [82, 167] (QWs). The setup involved a HgTe layer sandwiched between two CdTe layers

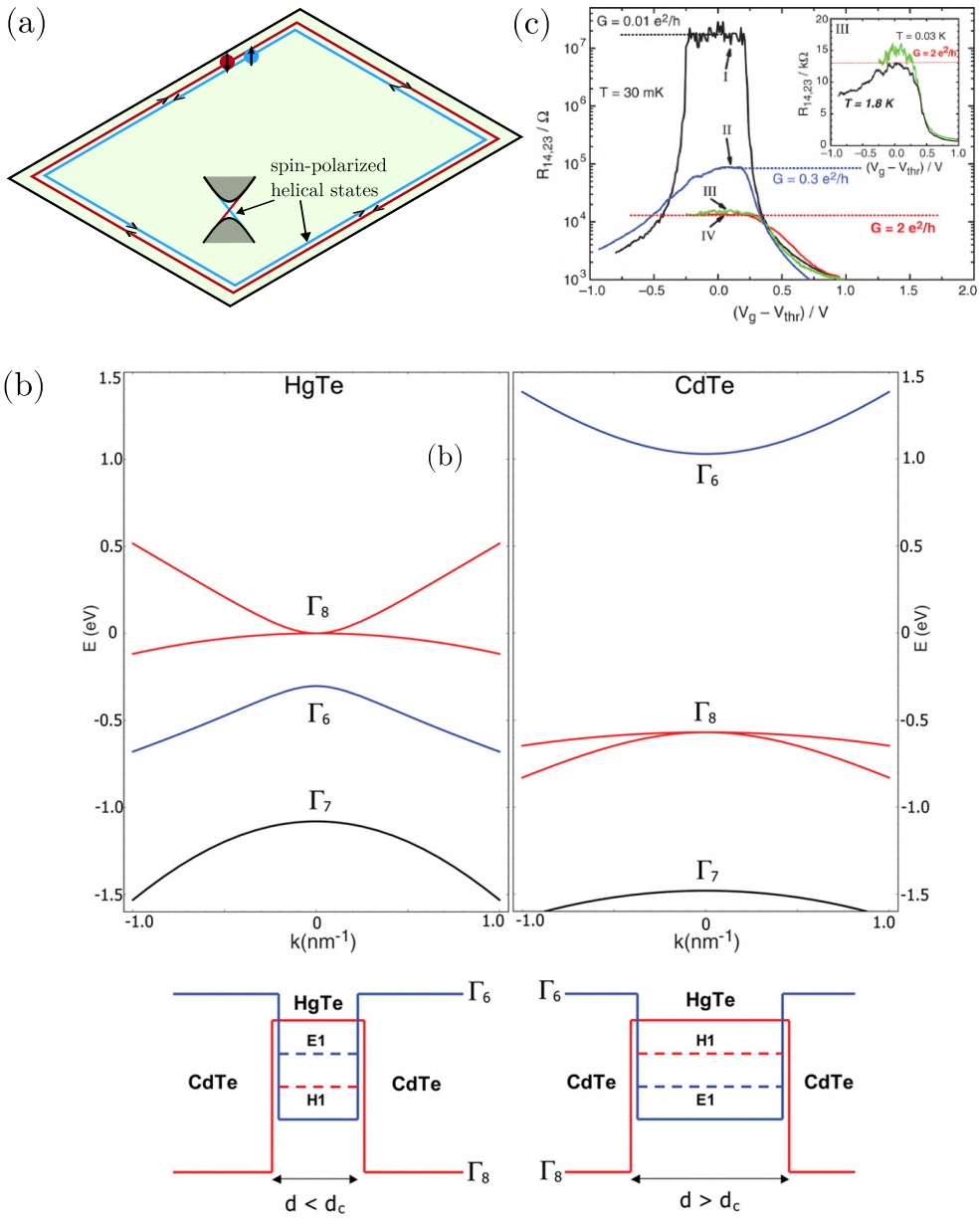

Figure 4.1: (a) Schematic of QSH state illustrates a pair of spin-polarzied helical states propagating along edge. In the QSH state, same helical states can be found inside of a gapped bulk. (b) Bulk bands of HgTe and CdTe (top) and schematic of band inversion in HgTe/CdTe quantum well (bottom) (adapted from Ref. [82]). Here, subbands E_1 and H_1 invert when quantum well thickness d crosses a critical value $d_c \approx 6.33$ nm. (c) Longitudinal Hall resistance of quantum well in the ordinary (I) and inverted regime (II,III,IV). QSH state exhibits quantizated conductance G in terms of $2e^2/h$. Inset shows temperature dependence of G (adapted from Ref. [167]).

[see bottom panel of Fig. 4.1(b)]. Bulk CdTe has a s-type conduction band (Γ_6) and p-type valence band (Γ_8), but this ordering is opposite in HgTe due to strong SOC of Hg element. When HgTe is placed between CdTe barriers, quantum confinement causes the bulk bands to split into a series of discrete subbands. For example, the Γ_6 band splits into $\{E_1, E_2, E_3, \ldots\}$, while the Γ_8 band splits into $\{H_1, H_2, H_3, \ldots\}$.

The hallmark of the experiment is that, as QW thickness d increases beyond a critical thickness $d_c \approx 6.3$ nm, E_1 and H_1 bands cross each other and invert [see Fig. 4.1(b)]. Other than band inversion, there exist probes like thermoelectric and non-local transport [168–171] to verify a TI. However, we use the quantized Hall conductance as an example here. When the QW thickness is well beyond the critical value and the system enters the inverted regime [see curves III and IV in Fig. 4.1(c)], the conductance approaches the quantized value $G = 2e^2/h$. This is several orders of magnitude larger than that of an ordinary insulating state [e.g., $G = 0.01e^2/h$ for curve I in Fig. 4.1(c)). The quantized conductance is observed at very low temperatures (typically in the mK range), while noticeable deviations emerge as the temperature increases [see inset of Fig. 4.1(c)].

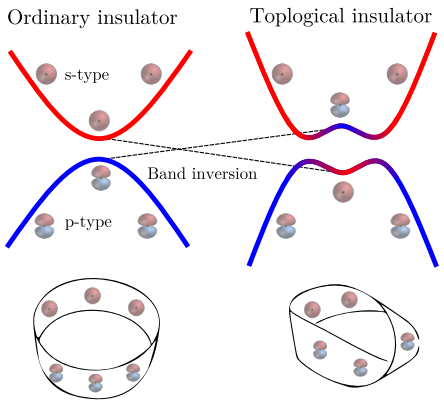

Figure 4.2: Schematic of ordinary and topological insulators illustrates the idea of band inversion. While an ordinary insulator is made up of separate s- and p- type bands, the orbital character switches in topological insulators. Intuitively, such continuous inversion of orbitals is analogous to topology of Möbius strip.

Initially, band inversion was used as one of the key signatures of TIs, where Bloch bands intertwine in a non-trivial way. A simple comparison helps illustrate this idea. In an ordinary insulator, the conduction and valence bands typically have well-defined orbital characters [see Fig. 4.2]. For example, conduction band may

originate from s-type orbitals, while the valence band is composed of p-type orbitals. In contrast, in a topological insulator, orbital character evolves and switches as one moves along a path in BZ. This continuous exchange of orbital character reflects the non-trivial topology of the band structure. An intuitive analogy is the Möbius strip: because of its topology, a path along the strip returns to the starting point with the orientation reversed. Similarly, in a TIs, orbital character of the bands evolves continuously and exchanges due to the underlying topological structure of the Bloch bands.

4.2 Theoretical models for QSH effect

4.2.1 Bernevig-Hughes-Zhang model

Bernevig–Hughes–Zhang (BHZ) model [82, 172, 173] is an effective four-band Hamiltonian that describes QSH effect in HgTe/CdTe QWs. In the model, there are four important bands derived from Γ point in BZ: $\{|E_1,+\rangle, |H_1,+\rangle, |E_2,-\rangle, |H_2,-\rangle\}$. Here E_1 and H_1 are subbands in QWs and $\pm$ refer to Kramer partners. Due to TRS, the 4×4 Hamiltonian has block diagonal structure

$$H_{\mathrm{BHZ}}(\mathbf{k}) = \begin{pmatrix} h(\mathbf{k}) & 0 \\ 0 & h^*(\mathbf{k}) \end{pmatrix}. \tag{4.1}$$

Here, $h(\mathbf{k})$ can be written in Bloch sphere structure $h(\mathbf{k}) = \epsilon(\mathbf{k})\mathbb{I}_2 + \mathbf{d}(\mathbf{k})\cdot\sigma$ with σ referring to vector of Pauli matrices and $\epsilon(\mathbf{k})$ and $\mathbf{d}(\mathbf{k})$ are given by

$$\epsilon(\mathbf{k}) = C - Dk^2, \quad \mathbf{d}(\mathbf{k}) = [Ak_x, Ak_y, M - Bk^2], \quad \text{where } k^2 = k_x^2 + k_y^2. \tag{4.2}$$

In the above model, $\{A, B, C, D, M\}$ denote material parameters, where B and M are particularly important. This is because B and M appear in the third component of $\mathbf{d}(\mathbf{k})$, which acts as a mass term. Parameter B (for this problem $B < 0$) controls

the quadratic momentum dependence and is often called Newtonian mass, where Dirac mass M is connected to QW thickness d such that sign of M changes beyond critical thickness d_c, i.e., $M > 0$ if $d < d_c$ and $M < 0$ if $d > d_c$. The hallmark of BHZ model is that its bulk topological invariant changes sign depending on $\mathrm{sgn}(M/B)$. Although $\mathrm{sgn}(M/B)$ dependence can be shown more rigorously, we use a hand-waving argument that checks how many times $\mathbf{d}(\mathbf{k})$ covers the Bloch sphere as we traverse from $k = 0$ to $k \to \infty$ [174]. When the sphere is covered exactly once, system is topological with Chern number $\mathcal{C} = \pm 1$, otherwise it is an ordinary insulator reflecting $\mathcal{C} = 0$. We see that $\mathbf{d}(\mathbf{k}) = [0, 0, M]$ for $k = 0$ and $\mathbf{d}(\mathbf{k}) = [0, 0, 1]$ as $k \to \infty$. Therefore, $\mathbf{d}(\mathbf{k})$ wraps the sphere only if $\mathrm{sgn}(M) < 0$, which corresponds to band-inverted topological regime for $d > d_c$. Result of this topology translates to edge states in the spectrum, which can be seen if BHZ model is solved on ribbon geometry. It is captured in Fig. 4.3(a), where a thick QW with supercritical thickness displays topological edge states that are not visible otherwise.

4.2.2 Kane–Mele model

Kane–Mele (KM) model, often called Kane-Mele SOC, is a microscopic lattice model for QSH effect, proposed by C. L. Kane and E. J. Mele in 2005. Unlike BHZ model, which is constructed from an effective four-band $(k \cdot p)$ continuum Hamiltonian, KM model is directly defined on honeycomb lattice. Novelty of KM model comes from a complex next-nearest neighbor hopping, which changes sign based on hopping direction. We can write the original QSH Hamiltonian on graphene

$$H^{g}_{\mathrm{QSH}} = H_T + H_{\mathrm{KM}} + H_R + H_v, \tag{4.3}$$

where first term refers to spinful version of kinetic term in Eq. (2.9)

$$H_T = -t \sum_{\langle ij\sigma \rangle} c^{\dagger}_{i\sigma} c_{j\sigma} - \mu \sum_{i\sigma} c^{\dagger}_{i\sigma} c_{i\sigma}. \tag{4.4}$$

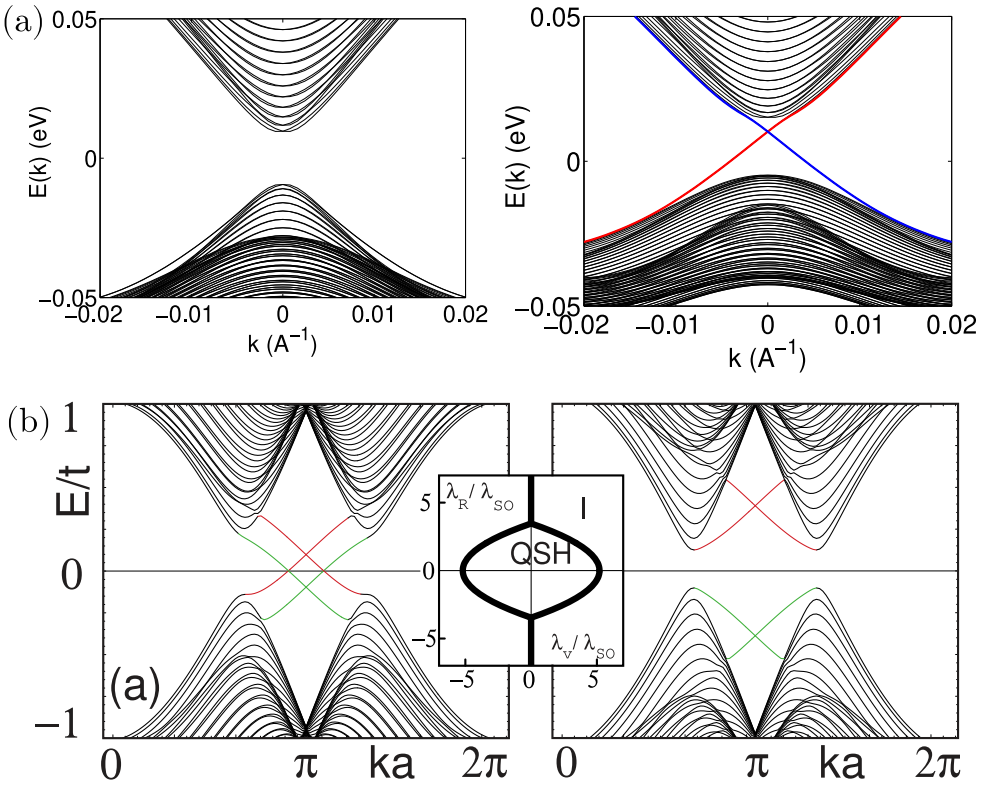

Figure 4.3: (a) Ribbon band structure of BHZ model for ordinary (left) and QSH (right) phase. Topological QSH state takes over when QW thickness crosses a critical value, resulting in gapless edge states (red, blue) inside gapped bulk (black) (adapted from Ref. [175]). (b) Ribbon band structure of Kane-Mele model on honeycomb lattice for QSH (left) and ordinary (right) phases. Staggered potential changes from $\lambda_v/t = 0.1$ in QSH phase to $\lambda_v/t = 0.4$ in ordinary phase, while Kane-Mele $\lambda_{\mathrm{SO}}/t = 0.06$ and Rashba SOC $\lambda_R/t = 0.05$ remain fixed. Inset shows QSH phase diagram between λ_v and λ_R (adapted from Ref. [81]).

The hallmark of KM model lies in H_{KM}, which has been introduced in Eq. (2.17). Kane-Mele also considered a Rashba SOC term, which is denoted by H_R and is already explained in Eq. (2.15). It is good to remember that the original QSH Hamiltonian denotes KM coupling strength as λ_{SO}, making it equivalent to λ_{KM}. We mostly use the former symbol to explain original results, but the latter is used throughout the thesis to denote KM SOC. Kane and Mele also considered a Rashba-type SOC in QSH Hamiltonian similar to Eq. (2.15). Finally, there is an onsite staggered potential

that breaks sublattice symmetry of graphene

$$H_v = \lambda_v \sum_i \xi_i c_{i\sigma} c_{i\sigma}, \tag{4.5}$$

with ξ_i being either 1 or -1 depending on A or B sublattice and λ_v refers to the strength of onsite potential.

In the absence of Rashba SOC (RSOC), parameters λ_{SO} and λ_v control the electronic properties. Kane-Mele showed that the energy gap in such a case is given by $\Delta E = |6\sqrt{3}\lambda_{\mathrm{SO}} - \lambda_v|$. Ratio of λ_{SO} to λ_v sets a critical point in the model $\lambda_{\mathrm{SO}}/\lambda_v = 1/(3\sqrt{3}) \approx 0.192$, above which the system exhibits a topological QSH phase. Below this critical value, spectrum is dominated by λ_v and the system behaves like an ordinary insulator. Topological QSH phase leads to TRS-protected gapless edge states in the bulk. This is captured in Fig. 4.3(b), where tuning $\lambda_v/t = 0.1 - 0.4$ with respect to λ_{SO}/t leads to a transition from QSH phase to an ordinary phase. QSH spectrum shows a pair of gapless edge states traversing the bulk, which otherwise become gapped. Here, edge states are doubled due to Kramer's theorem, which also prevents them from mixing with each other in case of a perturbation. This prevents backscattering and provides QSH edge states with topological immunity.

4.3 QSH model in kagome lattice

4.3.1 Model details

To investigate QSH effect, we consider KM model in kagome lattice. This prompts us to write the kagome QSH Hamiltonian

$$H_{\mathrm{QSH}} = H_T + H_{\mathrm{KM}}, \tag{4.6}$$

where we have described H_T and H_{KM} in Eq. (4.4) and Eq. (2.17), respectively. Obtaining bulk bands requires Fourier transformation of real-space Hamiltonian in Eq. (4.6) and diagonalizing it. In momentum space, we take the basis $\psi_{\mathbf{k}} = [c_{\mathbf{k}\alpha\sigma},\ c_{\mathbf{k}\alpha\sigma'}]^T$ with $\alpha = \{A, B, C\}$ and $\sigma = \{\uparrow, \downarrow\}$ indiacting sublattice and spin degrees of freedom, respectively. With this, KM Hamiltonian becomes a 6×6 matrix in momentum space

$$h_{\mathrm{KM}}(\mathbf{k}) = \sigma_z \otimes 2i\lambda_{\mathrm{KM}} \begin{bmatrix} 0 & \cos\delta_3 & -\cos\delta_1 \\ -\cos\delta_3 & 0 & \cos\delta_2 \\ \cos\delta_1 & -\cos\delta_2 & 0 \end{bmatrix}. \tag{4.7}$$

For compactness, we use Kronecker product $\otimes$ to write h_{KM} and further define $\delta_i = \mathbf{k} \cdot \mathbf{d}'_i$. Here, $\mathbf{d}'_i$ describe the vectors connecting NNN sites [see Fig. 3.3(a)], which can be written in terms of $\mathbf{a}_1$ and $\mathbf{a}_2$

$$\mathbf{d}'_1 = \frac{\mathbf{a}_2 - 2\mathbf{a}_1}{2}, \quad \mathbf{d}'_2 = \frac{\mathbf{a}_1 - 2\mathbf{a}_2}{2}, \quad \mathbf{d}'_3 = \frac{\mathbf{a}_1 + \mathbf{a}_2}{2}. \tag{4.8}$$

As we have discussed before, pristine kagome lattice host gapless bulk bands, which are two-fold degenerate due to spins. KM term turns this gapless bulk into a gapped bulk. Bulk spectrum presented in Fig. 4.4(a) illustrates this effect, where setting $\lambda_{\mathrm{KM}}/t = 0.15$. At the same time, KMSOC turns FB dispersive. Presence of bulk band gaps creates two unique insulating fillings $\langle n \rangle = 1/3$ and $\langle n \rangle = 2/3$, where Fermi level can be tuned to realize a potential QSH state.

4.3.2 Topological characterization of QSH bulk

Pfaffian matrix

Band topology of a TRS-invariant bulk system is characterized by a topological invariant known as $\mathbb{Z}_2$ index. Being a *mod* 2 quantity, $\mathbb{Z}_2$ index takes two values: 1 in

the topological phase and 0 in the trivial phase. Originally, Kane and Mele provided a method to compute $\mathbb{Z}_2$ in their seminal QSH work [81]. It relies on computing Pfafian of the sewing matrix, which encodes how Bloch states transform under TRS. Mathematically, if $\mathcal{T} = i\sigma_y K$ (K is complex conjugation) denotes TRS operator, then sewing matrix acting on n-th Bloch state $|u_n\rangle$ is given by

$$w_{mn}(\mathbf{k}) = \langle u_m(-\mathbf{k})|\mathcal{T}|u_n(\mathbf{k})\rangle. \tag{4.9}$$

At time-reversal-invariant-momenta (TRIM) Γ_i, $w_{mn}(\mathbf{k})$ becomes antisymmetric (i.e. $\mathbf{w} = -\mathbf{w}^T$), and thus admits a Pfaffian

$$P(\mathbf{k}) = \mathrm{Pf}[\mathbf{w}(\mathbf{k})]. \tag{4.10}$$

In this formulation, $P(\mathbf{k})$ is a central quantity. Generally, the Pfaffian can be thought of as a function of a skew-symmetric matrix $\mathbf{A}$ whose square equals the determinant $\mathrm{Pf}(\mathbf{A})^2 = \det(\mathbf{A})$. Because $P(\mathbf{k})$ is complex, its phase can wind and may exhibit zeros in momentum space. Kane and Mele showed that $\mathbb{Z}_2$ invariant is determined by counting the number of zeros of $P(\mathbf{k})$ inside the half Brillouin zone (HBZ) modulo two. Formally, the $\mathbb{Z}_2$ index is written as ν such that

$$\nu = \frac{1}{2\pi i}\oint_C d\mathbf{k}\cdot\nabla_{\mathbf{k}}\log[P(\mathbf{k}) + i\delta], \tag{4.11}$$

where the line integration path C is along the boundary of HBZ and δ is added to help with convergence. An even ν corresponds to a trivial insulator, while an odd ν signals a QSH insulator.

Wilson loop method

One drawback of Pfaffian method is that it is not gauge-invariant. It stems from the fact that there is a gauge freedom in choosing $|u_n(\mathbf{k})\rangle$. A better approach is given

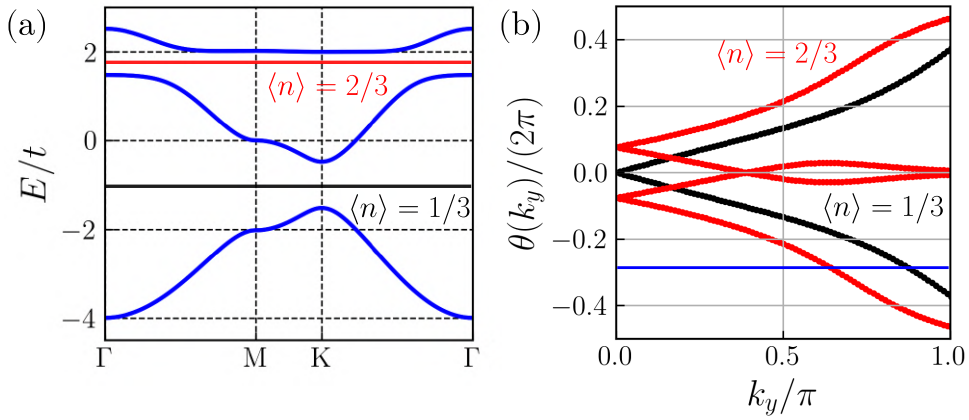

Figure 4.4: (a) The QSH bulk bands of kagome lattice. (b) The phase of the Wilson loop eigenvalues is plotted as a function of k_y. For both filling, $\theta(k_y)$ crosses a reference line $\theta_c = -0.3$ exactly once.

by the Wilson loop [176, 177] method, which is similar to tracking the evolution of hybrid Wannier charge center [176–178]. Numerically, Wilson loop approach provides better stability and is used in material-based softwares like Wannier90 [179] and Z2Pack [180]. Wilson loop is defined as the path-ordered exponential of the Berry connection along a closed loop C in momentum space

$$W(C) = \mathcal{P} \exp\Big(i \oint_C \boldsymbol{\mathcal{A}}(\mathbf{k}) \cdot d\mathbf{k} \Big), \tag{4.12}$$

where $\mathcal{P}$ is path ordering and $\boldsymbol{\mathcal{A}}(\mathbf{k}) = i\langle u_m(\mathbf{k}) | \nabla_{\mathbf{k}} | u_n(\mathbf{k}) \rangle$ represents the Berry connection with m, n as occupied band indexes. Phase of the Wilson loop is a key quantity in band topology since it captures the geometric phase accumulated by a Bloch wavefunction when an electron is transported around a closed path in momentum space. For discretized BZ, Yu *et. al.* [181] showed that Eq. (4.12) can be expressed as

$$W(k_y) = \prod_i \mathbf{P}_{i,i+1}(k_y), \tag{4.13}$$

where $P^{mn}_{i,i+1}(k_y) = \langle u_m(k_x^{i+1}, k_y) | u_n(k_x^{i+1}, k_y) \rangle$ is the overlap matrix. If there are N_{occ} occupied bands, then $\mathbf{P}$ is a $N_{\text{occ}} \times N_{\text{occ}}$ matrix and the phase of its eigenvalues λ_n is a central quantity

$$\theta_n(k_y) = \text{Im}[\ln \lambda_n(k_y)]. \tag{4.14}$$

Evolution of $\theta_n(k_y)$ against k_y indicates $\mathbb{Z}_2$ index of occupied bands. If $\theta(k_y)$ winds the 1D BZ spanned by k_y an odd number of times, $\mathbb{Z}_2$ topological number becomes 1, whereas it is 0 for even number of windings. This can alternatively be how many times $\theta(k_y)$ crosses a constant reference line θ_c.

To see it more clearly, we have plotted $\theta(k_y)$ in Fig. 4.4(b). It shows the evolution of $\theta(k_y)$ across HBZ for $1/3$ and $2/3$ filling of QSH bulk bands. Remember that, due to spin degeneracy, $1/3$ and $2/3$ fillings correspond to two and four occupied bands, respectively, which results in the same number of eigenvalue phases appearing in the plot. The lines start at $k_y = 0$ (Γ point), which is one of the special momenta that remain invariant under TRS. Such momenta are called time-reversal-invariant (TRIM) points, and as a result, $\theta(k_y)$ is degenerate at these points, irrespective of filling. As k_y is varied, $\theta(k_y)$ jumps nearly π amount for both fillings. Importantly, if we set a reference line at $\theta_c = -0.3$, $\theta(k_y)$ crosses this line once or, more generally, an odd number of times. This indicates a nontrivial bulk topological phase with $\mathbb{Z}_2$ index $\nu = 1$. It is worth noting that these odd crossings occur for any arbitrary θ_c.

4.3.3 Helical kagome edge states

Presence of TRS-invariant QSH bulk guarantees helical edge states at the boundary. Due to TRS, these edge states come in pairs and are spin-polarized. This can be seen in the ribbon band structure in Fig. 4.5. To illustrate how edge states are localized

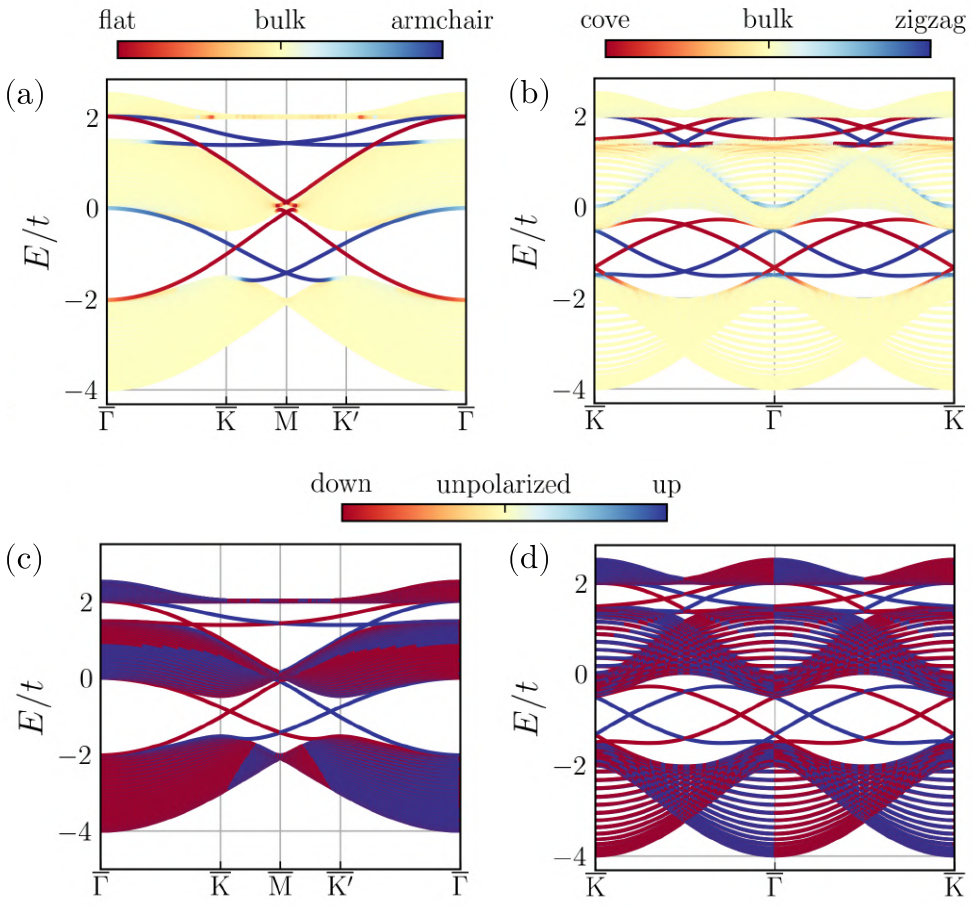

Figure 4.5: Kagome ribbon bands in the QSH phase for (a,c) armchair-flat and (b,d) zigzag-cove type termination. Color represents expectation of position operator in (a,b) and spin-polarization in (c,d). We set $\lambda_{\mathrm{KM}}/t = 0.15$ and $\mu/t = 0$ in all plots.

on boundary, we can project the expectation of position operator on the bands

$$\rho_{n,a}(\mathbf{k}) = \sum_i |\psi_{in}(\mathbf{k})|^2 \, \mathbf{r} \cdot \hat{e}_a, \tag{4.15}$$

where $\hat{e}_a$ denotes an unit vector along the axis $a = (x/y)$ perpendicular to momentum, ψ is the wavefunction, and $\mathbf{r}$ is the position operator. At the same time, it is judicious to define spin-polarization along z direction

$$m_{n,z} = \sum_i \langle \psi_{in} | S_z | \psi_{in} \rangle, \tag{4.16}$$

where $S_z = \mathrm{diag}(\mathbb{I}, -\mathbb{I})$ denotes z component of the spin operator.

We start with the projected ribbon band structure for armchair-flat termination in Fig. 4.5(a), which shows edge states inside two energy gaps corresponding to $\langle n \rangle = 1/3$ and $2/3$ insulating fillings in bulk [see Fig. 4.4(a)]. It is also possible to check TRS-invariance since $E(\overline{\mathrm{K}}) = E(\overline{\mathrm{K}'})$. Irrespective of filling or termination, there is a universal theme of helical states. That is, edge states belonging to same boundary have opposite slopes $\partial E/\partial k$, indicating their counter-propagating motion. At the same time, these counter-propagating states carry opposite spins [see Fig. 4.5(b,c)].

Remarkably, even though the flat termination does not host any edge states without SOC, we see the presence of an edge state under KM term. Similar picture is seen for the zigzag-cove termination in Fig. 4.5(d), with additional overlap of DP and Γ point.

5 Kagome quantum anomalous Hall state

5.1 Quantum Hall effect

Topological insulators exhibit a quantized spin Hall effect, which originates from the topology of their Bloch bands. However, the idea that Hall transport can acquire quantized values due to topological properties dates back to the early 80s. This concept was first experimentally realized in the landmark discovery of the integer quantum Hall effect, also known simply as the quantum Hall (QH) effect. In 1980, von Klitzing [182, 183] observed that a two-dimensional electron gas subjected to a strong perpendicular magnetic field exhibits a Hall conductance quantized in integer multiples of e^2/h. Remarkably, the precision of this quantization was so high—up to eight decimal places—that it became a standard for measuring resistivity [184].

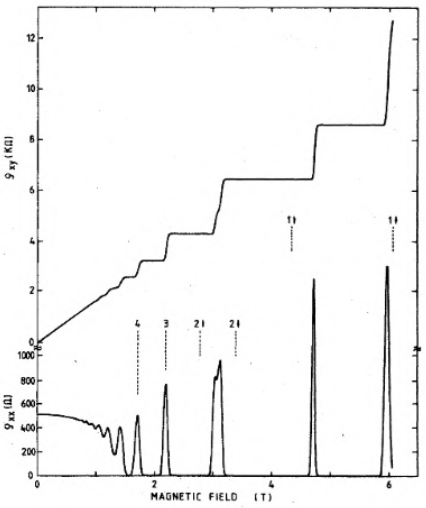

Figure 5.1: Hall resistivity ρ_{xy} and longitudinal resistivity ρ_{xx} of a quantum Hall sample plotted as a function of magnetic field (adapted from Ref. [182]). Quantized plateaus in ρ_{xy} are the hallmark of the experiment.

Under a strong magnetic field, the electronic states of the two-dimensional system condense into discrete Landau levels (LLs) [185], which are quantized cyclotron or-

bits with discrete energies. The QH experiment demonstrated that as the magnetic field varies, integer fillings of these Landau levels result in quantized Hall resistivity, R_H [see Fig. 5.1]. Simultaneously, the longitudinal resistivity R_{xx} approaches zero whenever R_H is quantized. Quantization of Hall conductance can be shown from Landau's theory; in fact, the Hall conductance at an integer filling ν has the expression

$$\sigma_{xy} = \nu \frac{e^2}{h}, \tag{5.1}$$

which shows discrete jumps of e^2/h each time the Fermi level crosses a Landau level. However, the more puzzling and subtler part is that quantization persists over a range of magnetic fields. The answer to this comes from the counterintuitive role of disorder. Particularly, in a pristine sample, LLs form sharply discrete energies, which get broadened by disorder. Most states in the tails of these broadened levels become localized and do not contribute to transport. Only the extended states near the center of each LL carry current. This gives rise to the characteristic plateaus observed in the Hall conductance.

The quantization in the QSH experiment was predicted by Ando *et. al.* [186] at University of Tokyo in 1975. However, a more complete picture and connection to topology was given by seminal work of Thouless, Kohmoto, Nightingale, and den Nijs in 1982 [187] . In this work, now widely known as the TKNN formulation, the Hall conductance was expressed in terms of a topological invariant

$$\sigma_{xy} = \mathcal{C} \frac{e^2}{h}, \tag{5.2}$$

where $\mathcal{C}$ is an integer termed as the Chern number. The role of $\mathcal{C}$ is profound here, as it triggered a paradigm shift in the classification of phases of matter. Unlike conventional local order parameters like magnetization, $\mathcal{C}$ depends on global properties of the Bloch wavefunction. It is noteworthy that Eq. (5.2) does not depend on dis-

order or perturbation, and therefore, the quantization is robust as long as the bulk gap exists.

5.2 Quantum anomalous Hall effect

Although QH effect is a foundational experiment with rich physics, its realization requires absurdly high magnetic fields, making it impractical for routine experiments. This started the quest for quantum anomalous Hall (QAH) effect [188], a version of the QH effect without the need of a magnetic field. Both QAH and QH effects require breaking of TRS, which is fundamentally different from previously discussed QSH effect. As a consequence, resulting edge states are significantly different. QAH phase leads to the so-called chiral edge states, which are spinless unidirectional states localized on the boundary. Even though helical states prevent backscattering in principle, it is not impossible (e.g. magnetic impurity). On the contrary, the lack of Kramer's theorem ensures that chiral states can exist as a single mode, eliminating any possibility of backscattering.

The route to a QAH platform was slow since the discovery of QH effect, and most of the progress was made after the discovery of TIs. Since TIs already have a connection to topology, the very first approach was to dope magnetic Mn ions to 2D TI platforms like HgTe/CdTe wells [189]. This proved to be unsuccessful since HgTe remain paramagnetic upon doping and does not break TRS [188]. Following theoretical predictions [190, 191], the first breakthrough came when 3D TI material $(Bi, Sb)_2Te_3$ was doped by magnetic Cr or Fe atoms [192, 193]. However, magnetic doping degrades material quality, and more recent methods prefer to use intrinsic magnetism [190]. This motivates the search for alternative ways to realize the QAH effect. The effect relies on broken TRS in materials, which in principle can be achieved by many factors, such as ferromagnetic order [191], non-coplanar magnetism [88], unconventional SC [194], chiral CDW [27], and loop current [146].

5.3 Microscopic theory of QAH effect: Haldane model

In 1988, Haldane gave the first microscopic theory for the QAH effect [195]. Haldane constructed a spinless toy model on graphene lattice, which broke TRS similar to magnetic materials. Such a system that breaks TRS yet keeps the lattice translation is known as a Chern insulator. The essence of Haldane model lies in a NNN complex hopping term. To see it more clearly, we write the QAH Hamiltonian based on the Haldane model on honeycomb lattice

$$H^{g}_{\mathrm{QAH}} = H_T + \sum_i (-M)^i c_i^\dagger c_i - \frac{t_2}{3\sqrt{3}} \sum_{\langle\langle ij \rangle\rangle} e^{i\phi_{ij}} c_i^\dagger c_j, \tag{5.3}$$

where H_T is already described in Eq. (2.9). The second term stands for a staggered onsite potential with strength M similar to Eq. (4.5). Finally, the last term describes the Haldane Hamiltonian, which contains a NNN hopping parameter t_2 and a phase factor ϕ_{ij}. The novelty of the model is that ϕ_{ij} takes $\pi/2$ for clockwise hopping and $-\pi/2$ for anticlockwise hopping. Despite having an appearance similar to KM Hamiltonian, Haldane term breaks TRS. This is because under TRS $\mathcal{T} : i \to -i$. In the KM Hamiltonian, there is an additional σ_z term that compensates for this negative sign, which is not possible in Haldane term, and the system is not invariant under TRS.

We can get a comprehensive idea of the Haldane model by writing Eq. (5.3) in momentum space $h^{g}_{\mathrm{QAH}}(\mathbf{k}) = \mathbf{d}(\mathbf{k}) \cdot \boldsymbol{\tau}$ such that

$$\begin{aligned} d_1(\mathbf{k}) &= t[1 + \cos(\mathbf{k}\cdot\mathbf{a}_1) + \cos(\mathbf{k}\cdot\mathbf{a}_2)] \\ d_2(\mathbf{k}) &= t[\sin(\mathbf{k}\cdot\mathbf{a}_1) + \sin(\mathbf{k}\cdot\mathbf{a}_2)] \\ d_3(\mathbf{k}) &= M + 2t_2\,[\sin(\mathbf{k}\cdot\mathbf{a}_1) - \sin(\mathbf{k}\cdot\mathbf{a}_2) - \sin(\mathbf{k}\cdot\mathbf{a}_1 - \mathbf{k}\cdot\mathbf{a}_2)], \end{aligned} \tag{5.4}$$

where $\boldsymbol{\tau}$ refers to a vector of Pauli matrices acting on sublattice space. With this

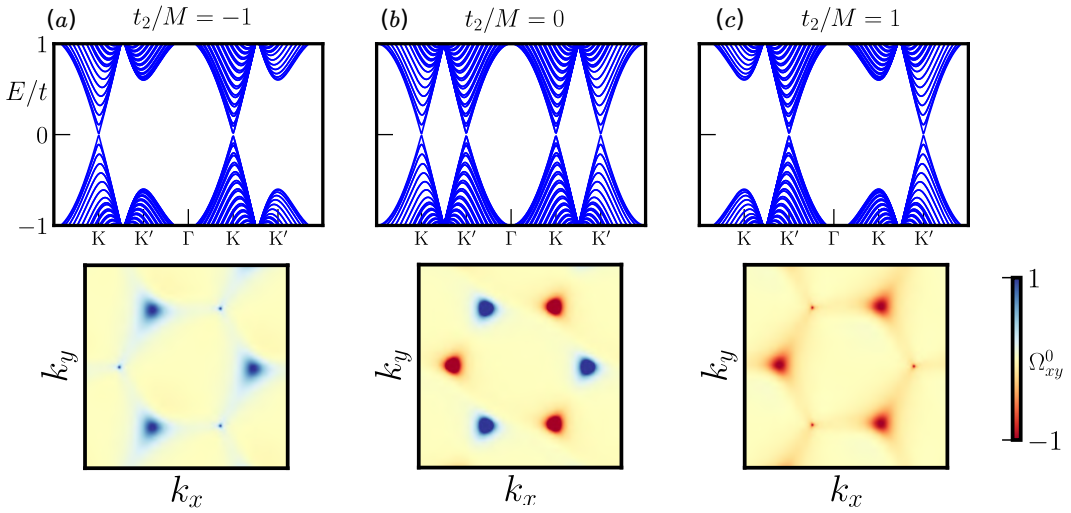

Figure 5.2: Honeycomb bulk bands (top) and their corresponding Berry curvature (bottom) for three sets of Haldane parameters: (a) $t_2/M = -1$, (b) $t_2/M = 0$, (c) $t_2/M = -1$. We take other parameters as $\mu/t = 0$ and $t = 1$.

Bloch sphere form, the energy bands are easy to write

$$E(\mathbf{k}) = \pm\sqrt{d_1^2(\mathbf{k}) + d_2^2(\mathbf{k}) + d_3^2(\mathbf{k})}. \tag{5.5}$$

The essential electronic and topological features of $h^g_{\text{QAH}}(\mathbf{k})$ are tuned by the ratio t_2/M. In more specific terms, presence of t_2/M gaps out a specific valley (K or K′) in the spectrum. This is demonstrated in top panel of Fig. 5.2, where bands are plotted along k_x axis (i.e. K–K′–Γ–K–K′ path) for multiple k_y values. As expected, $t_2/M = 0$ recreates band structure of pristine honeycomb lattice with Dirac points at K and K′. Now, if t_2/M is made finite, depending on its sign, a gap opens up either at K or K′. This valley-dependent physics gives away the lack of TRS of the system since $E(\text{K}) \neq E(\text{K}')$.

A central feature of Haldane model is that the system is an ordinary phase for $|t_2/M| < 1$, whereas a topological QAH phase emerges for $|t_2/M| > 1$. We show the Berry curvature in both regimes in bottom panel of Fig. 5.2 to illustrate this. Before interpreting the results, it is useful to remember that Dirac band touchings lead to

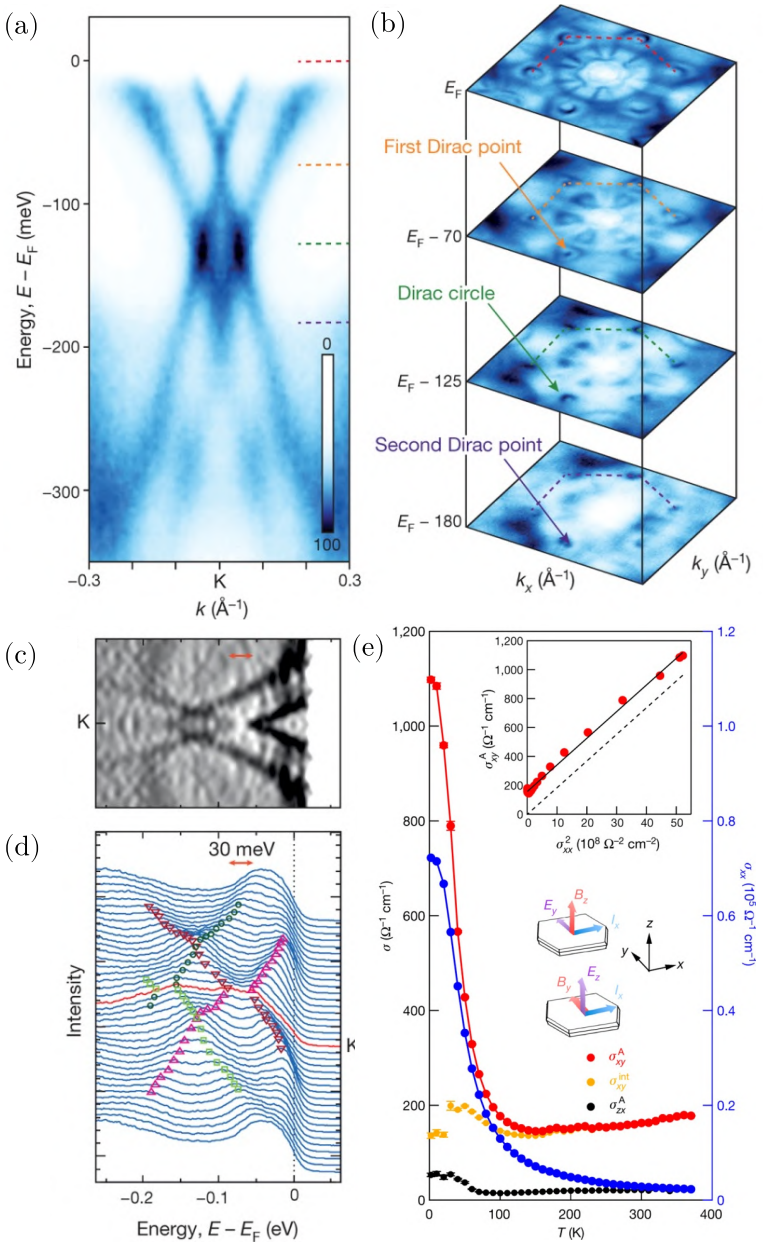

Figure 5.3: (a) ARPES data of kagome material Fe_3Sn_2. (b) Constant energy contour or Fermi surface for each dashed line in (a). (c) Second derivative of ARPES data and (d) stacked energy distributions highlight massive Dirac fermions at K point. (e) Magnetotransport as a function temperature presents anomalous conductivity tensors $\sigma^A_{xy,zx}$, intrinsic Hall conductivity σ^{int}_{xy}, and longitudinal conductivity σ_{xx}. Inset describes scaling between σ^A_{xy} and σ^2_{xx} (adapted from Ref. [21]).

peaks in Berry curvature and under TRS Berry curvatures satisfy $\Omega(\mathbf{k}) = -\Omega(-\mathbf{k})$. By virtue of this, Berry curvature of the pristine case $t_2/M = 0$ has a C_3 symmetric profile such that its sign changes as momentum is reversed. When we set $t_2/M = 1$, TRS vanishes, and the sign of Berry curvature no longer changes with momentum. In this regime, there is a net Berry curvature with its peaks localized at specific valleys tunable via $\mathrm{sgn}(t_2/M)$. Net positive or negative Berry curvature leads to $\mathcal{C} = 1$ or -1, respectively, which corresponds to the topological QAH phase.

5.4 QAH phase from ferromagnetism and Rashba SOC

5.4.1 Motivation from magnetic Weyl semimetals

In kagome materials, QAH effect was initially predicted using interplay of intrinsic magnetism and SOC [196]. Although theoretical blueprints for realizing the QAH effect in honeycomb lattices were already established, clean and naturally occurring magnetic systems with honeycomb geometry were rare. At the same time, there was a strong drive to realize QAH insulators with larger bulk gaps in order to achieve room-temperature operation. This naturally shifted the attention toward kagome lattices, which naturally occur in magnetic compounds and exhibit honeycomb-like electronic structure. In recent years, several kagome-based QAH platforms have been identified. This includes materials like (Fe,Co) based compounds [197–199], $ZrFe_2$ [200], 166 family of materials [21, 23, 201–203], and designer kagome lattices [204, 205].

Among these materials, Fe-based kagome compounds have been studied extensively in recent years; especially Fe_3Sn_2 demonstrates clear experimental signatures of a QAH conductivity at room temperatures. These are also known as magnetic Weyl semimetals. In Fig. 5.3(a,b), experimental ARPES data of Fe_3Sn_2 reveal the band dispersion and Fermi surface maps [21]. Especially in Fig. 5.3(b), changing energy

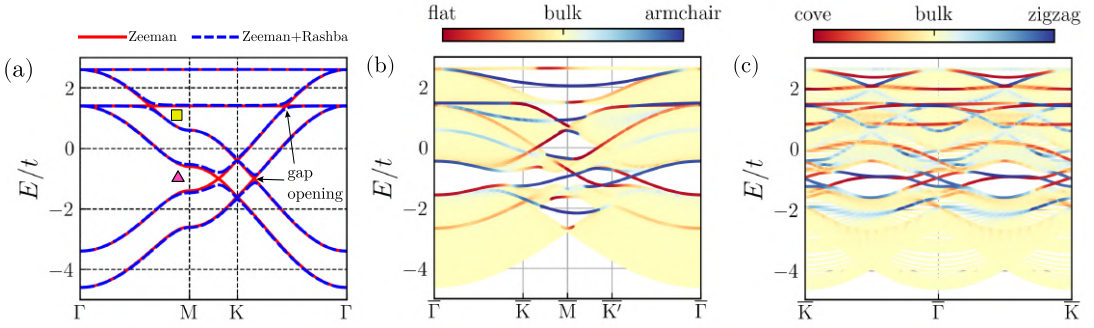

Figure 5.4: (a) The QSH bulk bands of the kagome lattice. (b) The phase of the Wilson loop eigenvalues is plotted as a function of k_y. For both filling, $\theta(k_y)$ crosses a reference line $\theta_c = -0.3$ exactly once. The ribbon band structure corresponding to the QSH phase is shown for (c) armchair-flat and (d) zigzag-cove termination. We take parameters $\lambda_R/t = 0.2$ and $h_z/t = 0.6$.

opens an energy gap at K point and creates massive Dirac fermions. This can be verified more clearly in Fig. 5.3(c,d), which shows nearly 30 meV gap in the spectrum. This map gap comes from SOC effects. A more direct diagnosis of QAH effect comes from magnetotransport. Fig. 5.3(e) shows that, at room temperature, longitudinal conductivity $\sigma_{xx} \approx 0$ almost vanishes and transport is dominated by anomalous conductivity tensor σ^A_{xy}. However, metallic nature of Fe_3Sn_2 is a bottleneck for observing quantized QAH effect, which requires an insulator, and thus anomalous conductivity is reported to be $\sigma^A_{xy} = 0.27e^2/h$ per bilayer [21].

5.4.2 Model details

There are several QAH candidates in kagome systems, which rely on breaking TRS by ferromagnetism. Magnetism can be intrinsic, like in magnetic Weyl systems, or it can be correlation-driven, where high electronic density leads to Stoner-type ferromagnetism. Motivated by this, we model the effective magnetic exchange as Zeeman field. In addition to this, presence of SOC is useful for lifting nodal-line degeneracies to realize a global gap in the spectrum. This effect can be effectively captured by introducing a Rashba spin–orbit coupling (RSOC) term, which serves

as a minimal model for inversion symmetry breaking. Thus, our QAH Hamiltonian reads

$$H_{\mathrm{QAH}} = H_T + H_Z + H_R, \tag{5.6}$$

where H_T is the kinetic Hamiltonian [see Eq. (4.4)]. Furthermore, H_Z and H_R describe out-of-plane Zeeman term and Rashba SOC, respectively [see Eq. (2.13) and (2.15)].

To analyze bulk bands, we can move to momentum space and write the QAH Hamiltonian

$$\begin{aligned} h_R(\mathbf{k}) &= \sigma_y \otimes \lambda_R \begin{bmatrix} 0 & \sin\delta_1 & \gamma^* \sin\delta_3 \\ \sin\delta_1 & 0 & \gamma \sin\delta_2 \\ \gamma^* \sin\delta_3 & \gamma \sin\delta_2 & 0 \end{bmatrix}, \\ h_Z(\mathbf{k}) &= \sigma_z \otimes \begin{bmatrix} h_z & 0 & 0 \\ 0 & h_z & 0 \\ 0 & 0 & h_z \end{bmatrix}, \end{aligned} \tag{5.7}$$

Here, we denote $\tau_i = \mathbf{k} \cdot \mathbf{d}_i$, $\mathbf{d}_i$ describe vector connecting NN sites, and $\gamma = i \exp[i\pi/6]$ is a coefficient.

We show the bulk bands in Fig. 5.4(a). Spinful kagome bands are two-fold degenerate in the pristine limit. Under Zeeman field, this degeneracy is lifted, and bands become spin-polarized. Subsequently, the spectrum contains a pair of DP and FB and two pairs of VHS. The Zeeman field alone does not open any gaps. When RSOC is turned on, bulk opens up a gap at DP and near FB. We also notice that bulk gap around FB is relatively much smaller.

One of the ways to characterize the nature of the bulk gaps is to inspect the ribbon band structure. This is displayed in Fig. 5.4(d,e), where colors depict edge state location similar to Fig. 4.5(a,b). Corresponding to bulk gaps, we see similar gaps

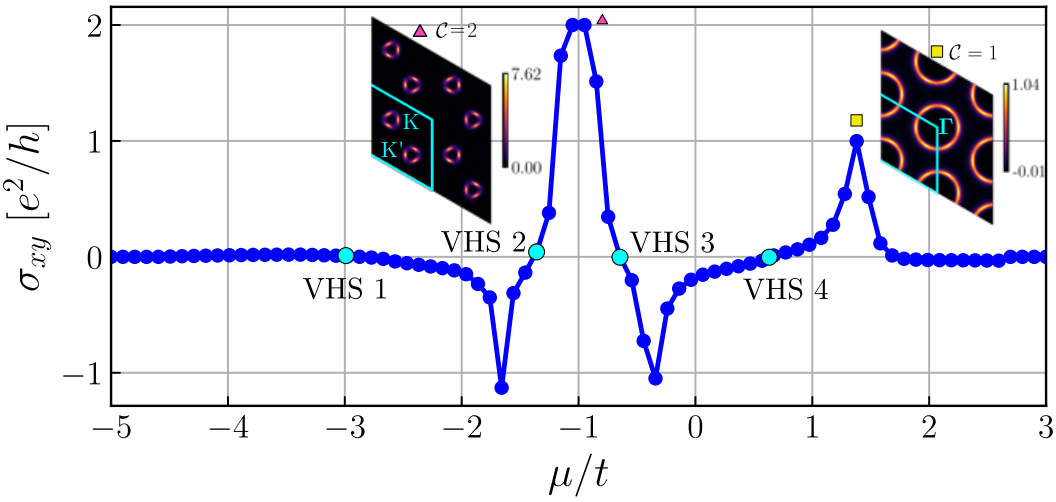

Figure 5.5: Anomalous Hall conductivity σ_{xy} (in terms of e^2/h) in kagome lattice is plotted as a function of chemical potential μ/t. Cyan circles indicate points where σ_{xy} changes sign. Furthermore, the inset shows Berry curvature maps in BZ corresponding to quantized reponses. We take parameters $\lambda_R/t = 0.2$ and $h_z/t = 0.6$.

appear in the ribbon bands, with edge states connecting the upper and lower bands. The fact that edge states (belonging to similar termination) have same sign of slope suggests these states are unidirectional. These are features of a chiral edge state. Although the edge states near the Dirac gap remain well-resolved, a small gap near FB hinders the visibility of edge states. Additionally, one can also notice the effect of valley mixing in zigzag-cover termination, which results in band structure periodicity spanning between $\overline{\text{K}}$–$\overline{\Gamma}$ points, with projected edge states appearing at $\overline{\Gamma}$ point.

5.4.3 Evolution of anomalous Hall conductance against filling

The hallmark of QAH effect is the quantization of Hall conductance in terms of e^2/h, which follows from the topological bulk order. An explicit confirmation of this order requires calculation of a topological invariant, which is Chern number in this case. Alternatively, one can also compute the anomalous Hall conductance σ_{xy}, which is

proportional to the Chern number when Fermi level is tuned inside the bulk gap corresponding to an insulator. Since Chern is defined for a 2D gapped insulator, such correspondence is not possible when systems are in a metallic state, and Fermi level crosses multiple bands.

Therefore, we compute σ_{xy} for a range of chemical potential (or filling). At $T = 0$, the intrinsic anomalous Hall conductance is given by [206, 207]

$$\sigma_{xy}(E) = \frac{e^2}{h} \int_{BZ} \frac{d^2k}{A_{BZ}} \sum_n \Omega_n(\mathbf{k})\ \Theta[E_n(\mathbf{k}) - E], \tag{5.8}$$

where Θ denotes the unit step function

$$\Theta(t) = \begin{cases} 1 & \text{if } t \geq 0 \\ 0 & \text{if } t < 0, \end{cases} \tag{5.9}$$

E_n corresponds to energy of the n-th filled band, A_{BZ} refers to BZ area, and the Berry curvature $\Omega_n(\mathbf{k})$ is already defined in Eq. (2.28).

We present the evolution of σ_{xy} versus chemical potential μ/t in Fig 5.5. We see that σ_{xy} becomes nonzero at various fillings owing to the TRS-broken bulk. The response exhibits a quantized plateau when μ/t is around -1. This corresponds to the case, when all bulk bands below the Dirac gap are filled [see bulk bands in Fig. 5.4(a)]. Since Fermi level lies inside bulk gap, here $\sigma_{xy} = \mathcal{C}e^2/h$ is expected to be quantized leading to the Chern number $\mathcal{C} = 2$. This is also in agreement with the bulk-boundary correspondence because we obtained exactly two chiral edge states in the ribbon spectrum [see Fig. 5.4(b,c)]. As μ/t is increased further, there is an additional quantized response close to FBs. Particularly, the plateau corresponds to Chern number $\mathcal{C} = 1$. Unfortunately, the narrow bulk gap makes this plateau hard to infer. Nonetheless, the different Chern numbers of these two topological gaps indicate distinct topological phases, and thus, a transition by continuous deformation is not

possible. This can be seen more qualitatively from insets of Fig 5.5, which showcase Berry curvature maps for $\mathcal{C} = 2$ and $\mathcal{C} = 1$. The Berry curvature maps of $\mathcal{C} = 2$ has asymmetric peaks (due to lack of TRS) around K and K′ valley. In contrast, a similar map for $\mathcal{C} = 1$ phase exhibits a ring shape around Γ.

We also point out that σ_{xy} undergoes a sign change at specific fillings. This happens when the Fermi level crosses a VHS point and is related to the Lifshitz transition [208]. Lifshitz originally predicted the phenomenon [209], which was later verified by ultrafast techniques [210]. A Lifshitz transition is a change in the topology of the Fermi surface (FS) driven by a continuous parameter, without breaking any symmetry. Two FSs are topologically different if they cannot be deformed into one another. Such differences are important in metals, where the FS controls the electronic properties.

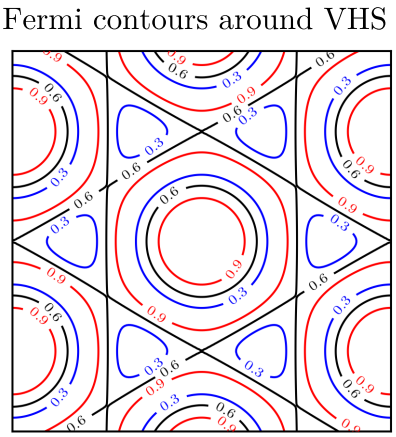

Figure 5.6: Fermi surface of the Kagome QAH model in the vicinity of VHS 4, corresponding to Fig. 5.5.

To show this in effect, we plot FS contours around VHS 4 (marked in Fig. 5.5) in Fig. 5.6. When the Fermi level crosses the VHS point at $\mu/t = 0.6$, the FS displays a hexagonal pattern with maximal extent, leading to a diverging DOS. Tuning μ/t above or below this point changes the FS abruptly. Specifically, setting $\mu/t = 0.3$ leads to circular FSs around the Γ and K, K′ points. The valley pockets disappear when the Fermi level moves above the VHS point. In this case, for $\mu/t = 0.9$, the FS consists of concentric circles around the Γ point.

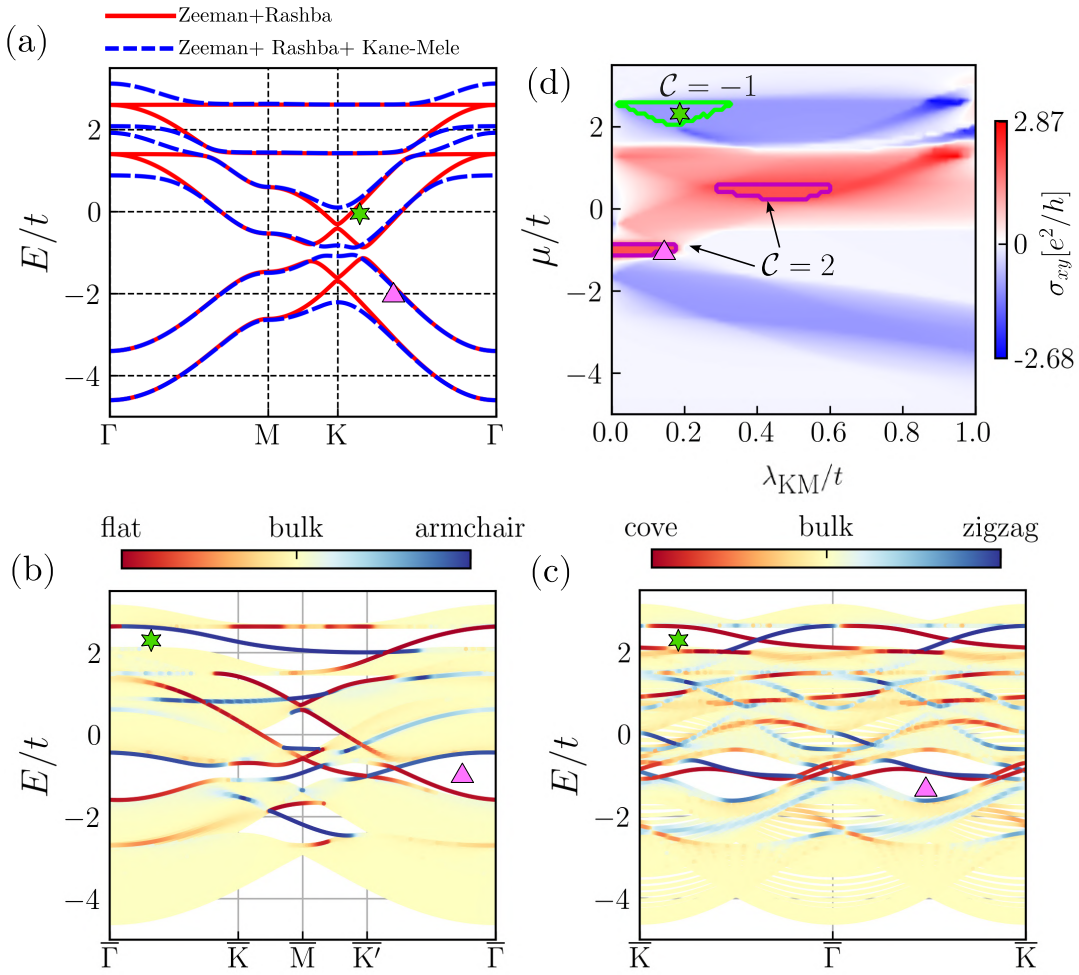

Figure 5.7: (a) Comparison of kagome bulk bands in the QAH phase without and with KMSOC ($\lambda_{KM}/t = 0.15$). Both cases have a constant Zeeman field ($h_z/t = 0.6$) and Rashba SOC ($\lambda_R/t = 0.2$). Ribbon spectrum in presence of KMSOC for (b) armchair-flat and (c) zigzag-cove type terminations. (d) Phase diagram describing tuning of anomalous Hall conductance σ_{xy} as chemical potential μ/t and KMSOC is changed. Closed areas indicate quantized anomalous response corresponding to a topological phase with non-zero Chern number $\mathcal{C}$. Star and triangle icons are used to highlight the bulk gaps related to topological phases.

5.4.4 Impact of Kane–Mele SOC on band topology

At this point, a natural question arises: does KMSOC influence the quantum QAH effect, and if so, does it suppress or enhance it? So far, we have neglected this term, as the combination of ferromagnetism (FM) and Rashba spin–orbit coupling (SOC) is already sufficient to realize the QAH phase. However, including KMSOC provides a more complete description of the band topology. This motivates us to consider the Hamiltonian in Eq. (5.10).

$$H' = H_{\mathrm{QAH}} + H_{\mathrm{KM}}, \tag{5.10}$$

where H_{QAH} is Hamiltonian in Eq. (5.6) and H_{KM} refers to KMSOC Hamiltonian [see Eq. (2.17)]. The corresponding bulk band structure is shown in Fig. 5.7(a). We observe that KMSOC opens additional energy gaps at the K [see green star] and [see magenta triangle]. These gaps are topological in nature. Specifically, the gap at K carries a Chern number $\mathcal{C} = 2$, while the gap at Γ has $\mathcal{C} = -1$. This is further confirmed by calculating the Hall conductivity σ_{xy} for in-gap fillings. In the slab geometry [see Fig. 5.7(b,c)], the spectrum exhibits either a single chiral edge state corresponding to a $\mathcal{C} = -1$ phase, or two chiral edge states corresponding to $\mathcal{C} = 2$. Note that, direction of the edge mode (i.e. $\partial E/\partial k$) changes when we compare two different gaps. This is connected to the opposite Chern number of these gaps. Furthermore, the inclusion of KMSOC also enlarges the gap FB, which is otherwise much narrower.

An important remaining question is how tuning the strength of KMSOC affects the topological phases across different fillings. To address this, we present the conductance phase diagram in Fig. 5.7(d). Here σ_{xy}, represented by the color scale, is plotted as a function of μ/t and λ_{KM}/t. We also devise a scheme to identify the topological regions. This is based on the observation that, for true quantization, the computed conductance should be very close to an integer value. Accordingly, we impose the

tolerance condition

$$\left|\sigma_{xy} - \text{round}(\sigma_{xy})\right| < \epsilon, \tag{5.11}$$

where $\epsilon = 10^{-8}$ is a small positive number. For small λ_{KM}/t, the Chern phases appear at fillings consistent with those indicated by the green star and magenta triangle and are in agreement with the band structure and edge spectra. If we start to tune λ_{KM}/t to higher values, these phases gradually disappear, and a distinct $\mathcal{C} = 2$ phase emerges near $\mu/t = 0$. However, for sufficiently large KMSOC, all Chern phases are eventually suppressed.

5.5 QAH phase from non-coplanar magnetism

In addition to FM order, non-coplanar (NCL) magnetic textures can also generate anomalous Hall responses. This arises from a quantity known as scalar spin chirality [211] (SSC), which is a mixed-scalar product of neighboring spins (i, j, k):

$$\chi_{ijk} = \mathbf{S}_i \cdot (\mathbf{S}_j \times \mathbf{S}_k). \tag{5.12}$$

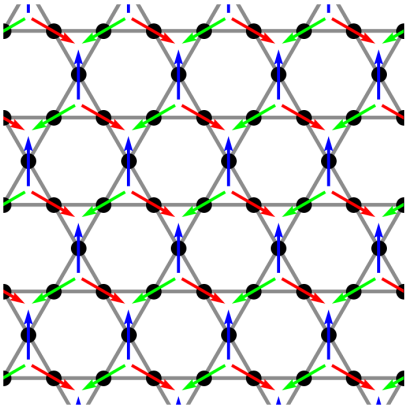

Figure 5.8: Figure illustrates 120° spin arrangement on kagome lattice corresponding to $\mathbf{q} = 0$ magnetic structure.

SSC becomes non-zero for noncollinear spins and remains zero otherwise. Wilczek and his collaborators have shown that properties of χ_{ijk} enable it to act like an effective magnetic field and are connected to the breaking of time-reversal symmetry (TRS) [212]. This makes the NCL order important for quantum anomalous Hall (QAH) phases. In fact, the idea gained strong support after the discovery of a large anomalous Hall

effect in noncollinear antiferromagnets such as Mn_3Sn [60] and Mn_3Ge [213].

The first theoretical prediction of a QAH phase arising from NCL order was made by Nagaosa and coauthors in 1999 [88]. Originally, they considered pyrochlore-kagome compounds, where magnetic spins assume a 120° AFM order. A true AFM is not possible on the kagome lattice due to its geometric frustration; however, spins on three sublattices can form 120° angles with each other. This configuration is dubbed as the $\mathbf{q} = 0$ structure [see Fig. 5.8]. In fact, the $\mathbf{q} = 0$ configuration is one of the allowed ground states of the Heisenberg model [214–216], with the magnetic unit cell being identical to the crystallographic unit cell. Although this magnetic order is coplanar in nature, Dzyaloshinskii-Moriya-type interactions [87, 217] in real materials can induce an out-of-plane component. In fact, such out-of-plane spin canting has already been reported in kagome systems [218–220].

5.5.1 Model details

Most previous studies of non-coplanar magnetic order are based on the Kondo lattice model, in which conduction electrons interact with localized magnetic moments through an exchange coupling. The theoretical treatment depends strongly on the magnitude of this coupling. In the strong-coupling limit, Ohgushi *et. al.* [88] employed a double-exchange framework, where the electron hopping amplitude acquires both a Peierls-like phase and a cosine factor determined by the relative angle between neighboring spins. In contrast, in the weak-coupling regime, the exchange interaction can be treated perturbatively [211]. We are interested in the intermediate regime, which cannot be solved analytically and requires numerics [221]. While bulk QAH phases driven by NCL order have been extensively investigated, the corresponding edge state dispersion and the role of SOC remain unexplored. We therefore explore the interplay between NCL magnetic order and SOC effects in this section.

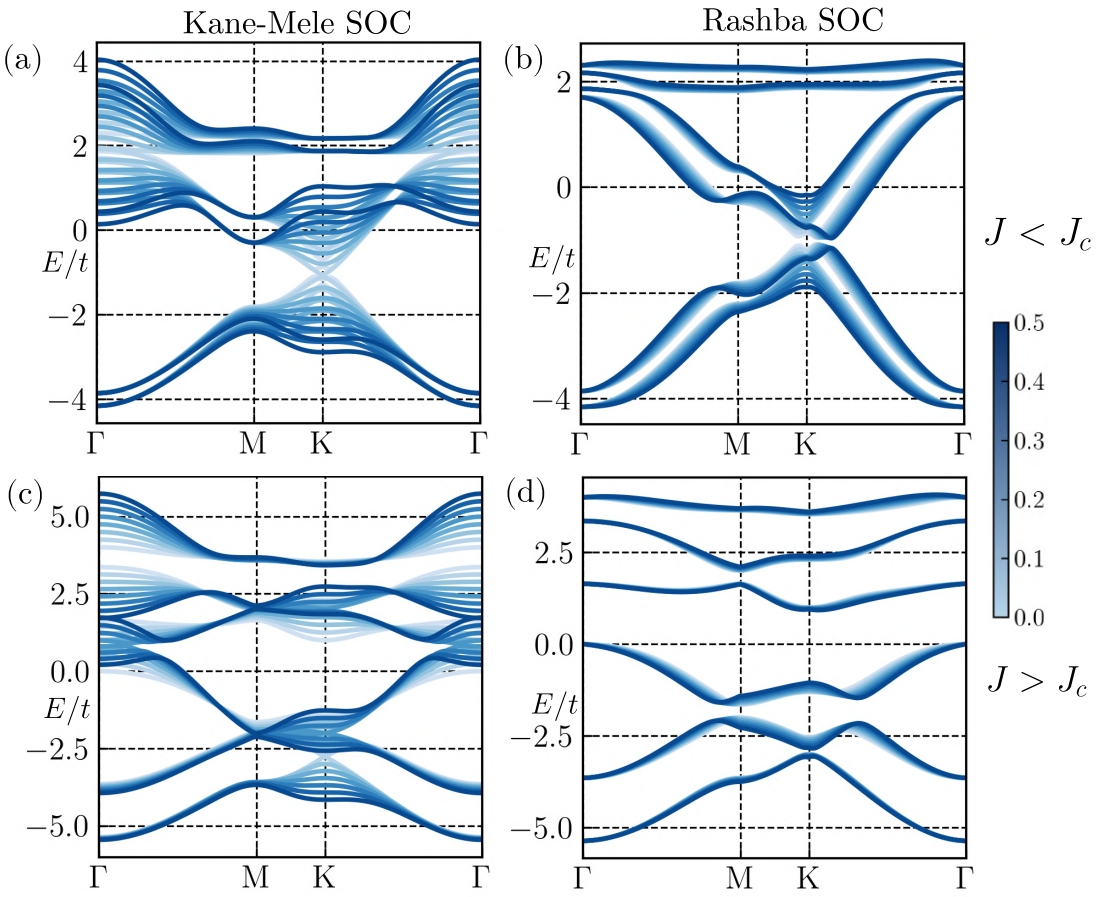

Figure 5.9: Kagome bulk band with NCL order is plotted for a range of (a,c) KMSOC and (b,d) RSOC coupling parameters. Top and bottom panels correspond to the subcritical ($J/t = 0.3$) and supercritical ($J/t = 2$) regimes of the exchange parameter J/t, with a critical value of $J_c/t \approx 1.51$.

We consider a minimal QAH Hamiltonian

$$H_{\mathrm{NCL}} = H_R + H_{\mathrm{KM}} + H_J, \tag{5.13}$$

where the first two terms refer to RSOC and KMSOC Hamiltonian [see Eq. (2.15) and Eq. (2.17)]. The last term denotes the magnetic Hamiltonian

$$H_J = -J_0 \sum_{i\sigma\sigma'} c^\dagger_{i\sigma}(\boldsymbol{\sigma}_{\sigma\sigma'} \cdot \mathbf{S}_i) c_{i\sigma'}, \tag{5.14}$$

where $\mathbf{S}_i$ describes the magnetic moment of i-th localized spin in spherical coordinates

$$\mathbf{S}_i = S\,(\sin\theta\cos\phi_i, \sin\theta\sin\phi_i, \cos\theta). \tag{5.15}$$

In this expression, $\phi_i \in (0, 2\pi/3, -2\pi/3)$ take three values depending on sublattice atom, $\theta \in [0, \pi]$ is the polar angle, and we define $J = J_0 S$ as the exchange parameter for compactness. Taillefumier *et. al.* [221] showed that θ sets a critical value $J = J_c$, where Chern number of bands changes. The relation between J_c and θ is given by

$$J_c(\theta)/t = \pm\frac{2}{\sqrt{1+3\cos^2\theta}}. \tag{5.16}$$

Now the parameter θ can vary a lot and is typically motivated by experiments. It is directly related to spin canting angle η via the relation $\theta = \pi/2 - \eta$. Some kagome compounds exhibit $\eta = \pi/6$ [222], and thus we take $\theta = \pi/3$ without losing any generality. This yields a critical coupling parameter $J_c/t \approx 1.51$ from Eq. (5.16).

First, we address the bulk properties of the QAH Hamiltonian in Eq. (5.13). Without SOC, the bulk remains gapless for small values of J/t. As J/t increases, a bulk gap appears due to the lifting of point-like degeneracies [221]. The situation becomes more straightforward in the presence of SOC. To gain a clearer understanding, we plot the bulk bands for a range of RSOC and KMSOC values from 0 to 0.5, while keeping the exchange field fixed [see Fig. 5.9]. We consider two representative regimes of the exchange coupling J: one below the critical value J_c ($J/t = 0.5$) and one above it ($J/t = 2$). These regimes are physically realistic. For instance, smaller values of J/t are typical in Fe-based kagome materials [223], where the Hund's coupling lies in the range $J_H/t \approx 0.25$–0.37. On the other hand, kagome heavy-fermion systems [224] with f electrons are expected to exhibit higher J/t values. Among the two types of SOC, we find that KMSOC modifies the band structure more significantly than RSOC. This remains true regardless of the J/t regime. More specifically,

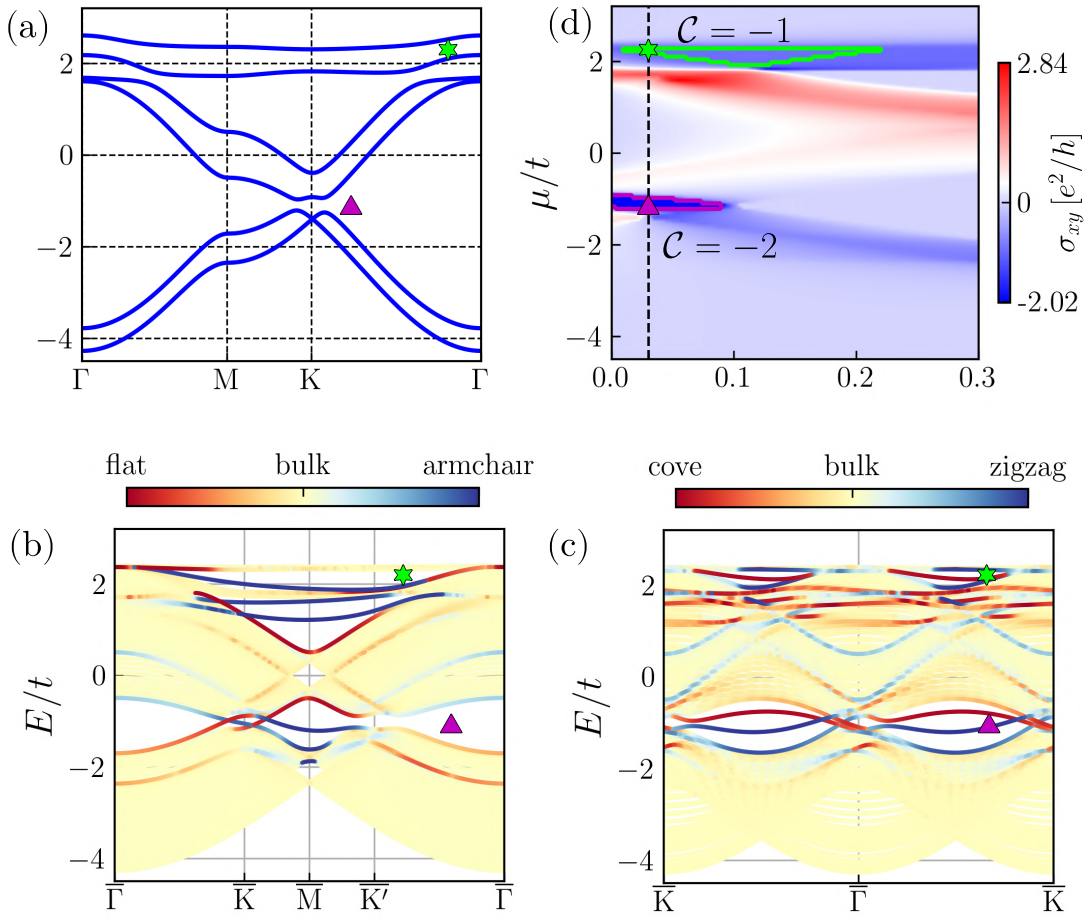

Figure 5.10: (a) Kagome bulk bands with subcritical exchange field $J/t = 0.3$ and KMSOC ($\lambda_{\mathrm{KM}}/t = 0.03$). Same parameters are used to show ribbon bands with (b) armchair-flat and (c) zigzag-cove termination. (d) Phase diagram describing anomalous conductance σ_{xy} (in terms of e^2/h) against chemical potential μ/t and KMSOC λ_{KM}/t. Closed regions denote quantized phases characterized by an integer Chern number $\mathcal{C}$, while icons relate specific points in the phase diagram to the bulk topological energy gap. Furthermore, a horizontal dashed line marks the KMSOC parameter used in band structure plots. We have use the following parameters $\mu/t = 0$, $\theta = \pi/3$, and $J_c(\theta)/t \approx 1.51$.

KMSOC facilitates the opening or closing of gaps at the K point, which may induce a topological transition. Based on this, we focus exclusively on the effects of KMSOC.

5.5.2 Subcritical exchange coupling

Let us first consider the subcritical exchange regime corresponding to $J < J_c$. We display the bulk bands under KMSOC for this case in Fig. 5.10(a). KMSOC opens multiple global gaps, which are further spin-split by the presence of the exchange field. These gaps are topological in nature. In fact, from Eq. (2.28), we estimate that the gaps marked by the triangle and star symbols exhibit $\mathcal{C} = -2$ and $\mathcal{C} = -1$, respectively. This is consistent with the number of edge states in the ribbon spectrum [see Fig. 5.10(b,c)]. We find that the gap corresponding to the triangle is large enough that its gapless edge modes are well separated from the bulk continuum. However, the chiral edge modes located in the gap denoted by the green star undergo hybridization with the bulk due to the smaller gap size, making them less distinct.

To obtain a complete picture of the topology, we compute the conductance phase diagram, similar to the FM case, and present it in Fig. 5.10(d). For small values of λ_{KM}/t, the phase diagram reveals two distinct Chern phases: one with Chern number $\mathcal{C} = -2$ (magenta triangle) and another with $\mathcal{C} = -1$ (green star). Notably, the $\mathcal{C} = -2$ phase can already be realized in the absence of KMSOC, whereas the $\mathcal{C} = -1$ phase emerges only at finite KMSOC. It is useful to note that KMSOC introduces helical-like characteristics to edge states, which cannot be fully captured by the Chern number (or anomalous conductance). Therefore, further increasing KMSOC generally leads to a vanishing Chern number. We restrict ourselves to $\lambda_{\mathrm{KM}}/t \leq 0.3$ in the phase diagram, beyond which no quantization is observed. This upper bound is motivated by the scale of J/t. Overall, when compared to the FM

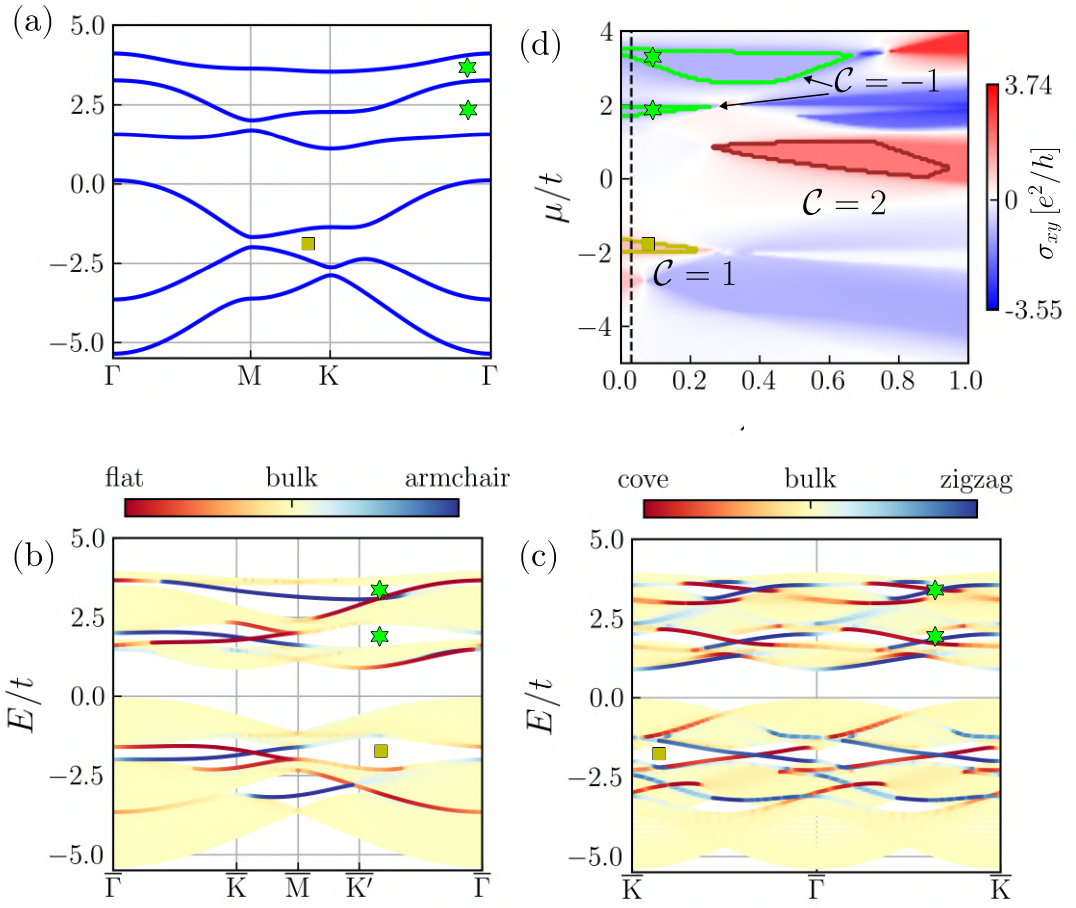

Figure 5.11: (a) Kagome bulk bands with supercritical exchange field $J/t = 2$ and KMSOC ($\lambda_{\mathrm{KM}}/t = 0.03$). Same parameters are used to show ribbon bands with (b) armchair-flat and (c) zigzag-cove termination. (d) Phase diagram describing anomalous conductance σ_{xy} (in terms of e^2/h) against chemical potential μ/t and KMSOC λ_{KM}/t. Closed regions denote quantized phases characterized by an integer Chern number $\mathcal{C}$, while icons relate specific points in the phase diagram to the bulk topological energy gap. Furthermore, a horizontal dashed line marks the KMSOC parameter used in band structure plots. We have use the following parameters $\mu/t = 0$, $\theta = \pi/3$, and $J_c(\theta)/t \approx 1.51$.

phase diagram, we observe that NCL Chern phases mostly exist at small values of λ_{KM}/t, while the gap corresponding to the triangle symbol undergoes a sign change.

5.5.3 Supercritical exchange coupling

On the other hand, when the system enters the supercritical regime $J > J_c$, the strong exchange field leads to a decoupling of the bands. This behavior is captured in the bulk band structure [see Fig. 5.11(a)], where we set $J/t = 2$. From this spectrum, we identify three global gaps, highlighted by green stars and yellow square markers. These marked gaps are topological in nature and each marker corresponds to a distinct Chern phase.

This can be further verified from the ribbon spectrum [see Fig. 5.11(b,c)], where the same gaps persist and each hosts a one gapless chiral edge mode. Comparing the propagation direction of these chiral modes across the topological gaps, we observe that the direction reverses between the star- and square-marked regions. This reversal is directly linked to a change in the sign of the Chern number, indicating distinct topological phases that can be accessed via band filling.

To clarify this further, we present the conductance phase diagram in Fig. 5.11(d). The dashed line indicates the KMSOC parameter corresponding to the band structure calculation. Along this cut, we observe a phase with $\mathcal{C} = -1$ below zero energy and two additional phases with $\mathcal{C} = 1$, consistent with the band structure results. However, the band plots do not fully capture the evolution of the topological gaps as λ_{KM}/t is varied. To address this, we increase λ_{KM}/t up to 1, following the same large-scale regime as J/t. We find that two of the three Chern phases present at small λ_{KM}/t disappear at larger values. Instead, a new phase with $\mathcal{C} = 2$ emerges and coexists with the topmost $\mathcal{C} = -1$ phase. For comparison, the $\mathcal{C} = 2$ phase is unique to the supercritical regime and does not appear in the subcritical regime.

Existence of the $C = 2$ phase at large KMSOC is particularly noteworthy, as such high values eliminate all Chern phases in the subcritical regime.

6 Conclusions

In summary, this thesis investigates pristine and topological edge states and their realization in kagome platforms. Distinct from bulk states, edge states refer to electronic states that are localized at the boundary. Over the years, edge states have become increasingly important due to their promise of topological immunity. This immunity arises from topological bulk order, which depends on global details instead of Landau-like local order parameters. In device applications where dissipationless transport or disorder-agnostic electronic state design is the main priority, such topological immunity is highly sought for. A contemporary example is the race to use Majorana edge states as a building block to realize noise-resilient quantum computing architecture. Therefore, study of edge states and their manipulation at the material level is a fundamentally important and timely topic. In this thesis, we demonstrate that kagome materials can be a fertile playground to explore the physics of edge states.

In Chapter 1, we describe main experimental signatures in kagome materials from an electronic perspective and lay out the goal of the thesis. Discussion of recent progress makes it clear that, while providing a honeycomb-like electronic structure, kagome materials exhibit rich charge and spin orders. This includes phenomena like charge density wave, superconductivity, spin-orbit coupling, Weyl phase, breathing distortion, complex magnetism, and Kondo physics. Effects like these may lead to the opening or closing of bulk bands, dimerization of bonds, Fermi arcs, pairing at Fermi level, or renormalization effects – all of which significantly affect edge state

properties. Motivated by this, we focus on rudimentary factors like lattice termination, spin-orbit coupling effects, and magnetism and see how they manipulate edge states in kagome systems.

We discuss key theoretical details in Chapter 2. We start by discussing concepts of second quantization and tight-binding framework. Tight-binding approach lets us write effective Hamiltonians on a discrete lattice to describe bands. While this captures essential physics, the numerical expense stays fairly low compared to other sophisticated numerical methods. We explain how to model terms such as Zeeman field and spin-orbit coupling using this methodology. We also provide a brief introduction to topological band theory and discuss recurring themes such as band touchings, Hamiltonian symmetries, Berry curvature, and topological invariants.

We investigate pristine edge states of kagome lattice in 3. These states originate from a lack of periodic crystal potential in finite geometries. Originally known as Shockley states, we show how these states arise in Schördinger's equation with their first realization in Cu(111) slab. This is followed by a discussion of graphene nanoribbons, where armchair and zigzag-type terminations lead to significantly different results. Motivated by this, we identify four terminations in kagome lattice that are possible due to a line cut: armchair, flat, zigzag, and cove. By virtue of kagome geometry, armchair and flat terminations occur at fixed y direction, whereas zigzag and cove terminations are possible along fixed x direction. Overall, we find that terminations control number of edge states and strongly affect edge dispersion. Effect on edge dispersion is particularly non-trivial for flat termination, resulting in a complete suppression of edge state, and the ribbon bands behave similarly to bulk. We additionally unfold that zigzag and cove terminations exhibit valley-mixing effect due to projection from bulk to ribbon Brillouin zone, resulting in momenta where K and K$'$ points are superimposed. Subsequently, Brillouin zone projection leads to additional edge states at Γ point. These effects are absent in armchair-flat terminations and valleys remain pure.

Our discussion of topological kagome edge states begins in Chapter 4. Particularly, we discuss how pristine edge states in Chapter 3 turn into topological helical states when intrinsic spin-orbit coupling (SOC) is used. Helical edge states are a consequence of time-reversal protected quantum spin Hall (QSH) phase, which depicts the bulk state of a 2D topological insulator. As a first step, we explain the original QSH platforms, effective theoretical models, and topological characterization of bulk to give an overview. Following the Kane–Mele model for the QSH in graphene, we investigate the impact of an analogous term in a kagome lattice. Our analysis of bulk bands indicate opening of two global gaps near Dirac point (DP) and flat band (FB). We confirm that both these gaps are topological from Wilson loop analysis. Finally, ribbon bands highlight bulk gaps that host counter-propagating, spin-polarized edge states at these fillings, which confirms their helical nature.

In Chapter 5, we discuss realization of chiral edge states primarily from intrinsic magnetism. Specifically, we investigated chiral edge states as a boundary effect of a quantum anomalous Hall (QAH) bulk, in which a Hall effect emerges without a magnetic field. We first give a historical overview of QAH by discussing early developments, experimental breakthrough, and the microscopic model. Motivated by ferromagnetic kagome materials, we then propose a minimal QAH kagome platform with Zeeman field and Rashba SOC. This combination leads to the opening of two bulk gaps, which consequently host gapless edge states in the ribbon spectrum. Compared to helical states, these edge states are unidirectional and do not necessarily come in pairs, which confirms their chiral nature. Topological chiral character is also apparent since anomalous Hall conductivity becomes quantized for insulating fillings. Here, finite Kane-Mele SOC increases band gaps and makes topological gaps more distinct.

In the same chapter, we also investigate QAH phase arising from non-coplanar magnetism and discuss SOC effects. The non-coplanar texture is given by 120° antiferromagnetic order with out-of-plane canting of spins. Our main results show that the

canting angle defines a critical exchange field, where Chern numbers of QAH phase change. Moreover, while Rashba SOC has a negligible impact on the band topology, Kane–Mele SOC strongly reconstructs the bulk spectrum by opening and closing gaps across a wide energy range, thereby driving topological phase transitions in both subcritical and supercritical regimes. In the subcritical regime, Kane–Mele SOC initially promotes Chern insulating phases with $\mathcal{C} = -2, -1$, but with increasing strength, these phases are progressively suppressed, ultimately yielding a trivial state. By contrast, in the supercritical regime, it induces multiple topological gaps with $\mathcal{C} = \pm 1$ and, at higher values, stabilizes an additional $\mathcal{C} = 2$ phase, leading to the coexistence of distinct topological phases. This highlights that KMSOC not only tunes but also qualitatively reorganizes the topological phase diagram depending on the exchange coupling strength.

Appendix A

Mirror symmetry-protected edge states

Consider the boundaries of a semi-infinite slab geometry are structurally equivalanet, then the edge states are connected by mirror symmetry. For an example, if the slab is finite along x axis then left (or right) edge state is mapped to the right (or left) edge state by virtue of mirror operator $\mathcal{M}_x$

$$\mathcal{M}_x|\psi_L\rangle = |\psi_R\rangle. \tag{A.1}$$

Here, eigenstates are projected on a subspace spanned by $\{|\psi_L\rangle, |\psi_R\rangle\}$. If we consider $|\psi_L\rangle$ is the left eigenstate satifying $H|\psi_L\rangle = E|\psi_L\rangle$, then operating H on $|\psi_R\rangle$ shows

$$H|\psi_R\rangle = H\mathcal{M}_x|\psi_L\rangle = \mathcal{M}_x H|\psi_L\rangle = E\mathcal{M}_x|\psi_L\rangle = E|\psi_R\rangle. \tag{A.2}$$

We see that right eigenstate occurs with same energy E. Here, we have used the relation: $[H, \mathcal{M}_x] = 0$. Therefore, the Hamiltonian is given by

$$H = \begin{pmatrix} E & \Lambda \\ \Lambda^* & E \end{pmatrix}, \tag{A.3}$$

where $E = \langle \psi_{L/R} | H | \psi_{L/R} \rangle$ and $\Lambda = \langle \psi_L | H | \psi_R \rangle$. Physically, Λ quantifies the tunneling amplitude between the left- and right-localized edge states. For an edge mode whose wavefunction is peaked at the boundary and decays exponentially into the bulk, this overlap is exponentially suppressed. In particular, $\Lambda \sim e^{-L/\xi}$ where L denotes the slab length and ξ is the localization length. Thus, increasing L suppresses the off-diagonal coupling, $\Lambda \to 0$, and the two edge states become effectively decoupled. In this limit, their energies converge, which ensures a twofold degeneracy.

Bibliography

[1] G. C. S. Branko Grunbaum, *Tilings and Patterns: Second Edition*. New York: Dover Publications Inc., 2016.

[2] J. Yin, "Exploring unknown quantum states in cage crystals," *Physics*, vol. 52, p. 157, 2023.

[3] China News Service, "Bamboo weaving products of ba culture first appeared in chongqing about 2200 years ago," 2022.

[4] Okinawa Institute of Science and Technology Graduate University (OIST), "Kagome basket," 2016.

[5] M. Mekata, "Kagome: The story of the basketweave lattice," *Phys. Today*, vol. 56, p. 12, 2003.

[6] L. Onsager, "Crystal statistics. I. a two-dimensional model with an order-disorder transition," *Phys. Rev.*, vol. 65, p. 117, 1944.

[7] K. Husimi and I. Syôzi, "The statistics of honeycomb and triangular lattice. I," *Progress of Theoretical Physics*, vol. 5, p. 177, 1950.

[8] I. Syôzi, "Statistics of kagomé lattice," *Progress of Theoretical Physics*, vol. 6, p. 306, 1951.

[9] M. Takano, T. Shinjo, M. Kiyama, and T. Takada, "Magnetic properties of jarosites, $RFe_3(OH)_6(SO_4)_2$(R=NH_4, Na or K)," *J. Phys. Soc. Jpn.*, vol. 25, p. 902, 1968.

[10] C. Broholm, G. Aeppli, G. P. Espinosa, and A. S. Cooper, "Antiferromagnetic fluctuations and short-range order in a kagomé lattice," *Phys. Rev. Lett.*, vol. 65, p. 3173, 1990.

[11] P. Anderson, "Resonating valence bonds: A new kind of insulator?," *Mater. Res. Bull.*, vol. 8, p. 153, 1973.

[12] J. S. Helton, K. Matan, M. P. Shores, E. A. Nytko, B. M. Bartlett, Y. Yoshida, Y. Takano, A. Suslov, Y. Qiu, J.-H. Chung, D. G. Nocera, and Y. S. Lee, "Spin dynamics of the spin-1/2 kagome lattice antiferromagnet $ZnCu_3(OH)_6Cl_2$," *Phys. Rev. Lett.*, vol. 98, p. 107204, 2007.

[13] A. Olariu, P. Mendels, F. Bert, F. Duc, J. C. Trombe, M. A. de Vries, and A. Harrison, "^{17}O NMR study of the intrinsic magnetic susceptibility and spin dynamics of the quantum kagome antiferromagnet $ZnCu_3(OH)_6Cl_2$," *Phys. Rev. Lett.*, vol. 100, p. 087202, 2008.

[14] F. Wang and A. Vishwanath, "Spin-liquid states on the triangular and kagomé lattices: A projective-symmetry-group analysis of schwinger boson states," *Phys. Rev. B*, vol. 74, p. 174423, 2006.

[15] M. Hermele, Y. Ran, P. A. Lee, and X.-G. Wen, "Properties of an algebraic spin liquid on the kagome lattice," *Phys. Rev. B*, vol. 77, p. 224413, 2008.

[16] Y.-M. Lu, Y. Ran, and P. A. Lee, "Z_2 spin liquids in the $s = \frac{1}{2}$ Heisenberg model on the kagome lattice: A projective symmetry-group study of Schwinger fermion mean-field states," *Phys. Rev. B*, vol. 83, p. 224413, 2011.

[17] Y. Iqbal, F. Becca, S. Sorella, and D. Poilblanc, "Gapless spin-liquid phase in the kagome spin-$\frac{1}{2}$ Heisenberg antiferromagnet," *Phys. Rev. B*, vol. 87, p. 060405, 2013.

[18] T. Dodds, S. Bhattacharjee, and Y. B. Kim, "Quantum spin liquids in the absence of spin-rotation symmetry: Application to herbertsmithite," *Phys. Rev. B*, vol. 88, p. 224413, 2013.

[19] M. Punk, D. Chowdhury, and S. Sachdev, "Topological excitations and the dynamic structure factor of spin liquids on the kagome lattice," *Nat. Phys.*, vol. 10, p. 289, 2014.

[20] Y. Iqbal, D. Poilblanc, and F. Becca, "Vanishing spin gap in a competing spin-liquid phase in the kagome Heisenberg antiferromagnet," *Phys. Rev. B*, vol. 89, p. 020407, 2014.

[21] L. Ye, M. Kang, J. Liu, F. von Cube, C. R. Wicker, T. Suzuki, C. Jozwiak, A. Bostwick, E. Rotenberg, D. C. Bell, L. Fu, R. Comin, and J. G. Checkelsky, "Massive dirac fermions in a ferromagnetic kagome metal," *Nature*, vol. 555, p. 638, 2018.

[22] B. R. Ortiz, L. C. Gomes, J. R. Morey, M. Winiarski, M. Bordelon, J. S. Mangum, I. W. H. Oswald, J. A. Rodriguez-Rivera, J. R. Neilson, S. D. Wilson, E. Ertekin, T. M. McQueen, and E. S. Toberer, "New kagome prototype materials: discovery of KV_3Sb_5, RbV_3Sb_5, and CsV_3Sb_5," *Phys. Rev. Mater.*, vol. 3, p. 094407, 2019.

[23] M. Kang, L. Ye, S. Fang, J.-S. You, A. Levitan, M. Han, J. I. Facio, C. Jozwiak, A. Bostwick, E. Rotenberg, M. K. Chan, R. D. McDonald, D. Graf, K. Kaznatcheev, E. Vescovo, D. C. Bell, E. Kaxiras, J. van den Brink, M. Richter, M. Prasad Ghimire, J. G. Checkelsky, and R. Comin, "Dirac fermions and flat bands in the ideal kagome metal FeSn," *Nat. Mater.*, vol. 19, p. 163, 2020.

[24] B. R. Ortiz, S. M. L. Teicher, Y. Hu, J. L. Zuo, P. M. Sarte, E. C. Schueller, A. M. M. Abeykoon, M. J. Krogstad, S. Rosenkranz, R. Osborn, R. Seshadri, L. Balents, J. He, and S. D. Wilson, "CsV_3Sb_5: A Z_2 topological kagome metal with a superconducting ground state," *Phys. Rev. Lett.*, vol. 125, p. 247002, 2020.

[25] B. R. Ortiz, S. M. L. Teicher, L. Kautzsch, P. M. Sarte, N. Ratcliff, J. Harter, J. P. C. Ruff, R. Seshadri, and S. D. Wilson, "Fermi surface mapping and the

nature of charge-density-wave order in the kagome superconductor CsV_3Sb_5," *Phys. Rev. X*, vol. 11, p. 041030, 2021.

[26] H. Zhao, H. Li, B. R. Ortiz, S. M. L. Teicher, T. Park, M. Ye, Z. Wang, L. Balents, S. D. Wilson, and I. Zeljkovic, "Cascade of correlated electron states in the kagome superconductor CsV_3Sb_5," *Nature*, vol. 599, p. 216, 2021.

[27] Y.-X. Jiang, J.-X. Yin, M. M. Denner, N. Shumiya, B. R. Ortiz, G. Xu, Z. Guguchia, J. He, M. S. Hossain, X. Liu, J. Ruff, L. Kautzsch, S. S. Zhang, G. Chang, I. Belopolski, Q. Zhang, T. A. Cochran, D. Multer, M. Litskevich, Z.-J. Cheng, X. P. Yang, Z. Wang, R. Thomale, T. Neupert, S. D. Wilson, and M. Z. Hasan, "Unconventional chiral charge order in kagome superconductor KV_3Sb_5," *Nat. Mater.*, vol. 20, p. 1353, 2021.

[28] B. R. Ortiz, P. M. Sarte, E. M. Kenney, M. J. Graf, S. M. L. Teicher, R. Seshadri, and S. D. Wilson, "Superconductivity in the Z_2 kagome metal KV_3Sb_5," *Phys. Rev. Mater.*, vol. 5, p. 034801, 2021.

[29] Z. Liang, X. Hou, F. Zhang, W. Ma, P. Wu, Z. Zhang, F. Yu, J.-J. Ying, K. Jiang, L. Shan, Z. Wang, and X.-H. Chen, "Three-dimensional charge density wave and surface-dependent vortex-core states in a kagome superconductor CsV_3Sb_5," *Phys. Rev. X*, vol. 11, p. 031026, 2021.

[30] T. Park, M. Ye, and L. Balents, "Electronic instabilities of kagome metals: Saddle points and Landau theory," *Phys. Rev. B*, vol. 104, p. 035142, 2021.

[31] A. Ptok, A. Kobiałka, M. Sternik, J. Łażewski, P. T. Jochym, A. M. Oleś, and P. Piekarz, "Dynamical study of the origin of the charge density wave in AV_3Sb_5 (A= K, Rb, Cs) compounds," *Phys. Rev. B*, vol. 105, p. 235134, 2022.

[32] A. Ptok, S. Basak, A. Kobiałka, M. Sternik, J. Łażewski, P. T. Jochym, A. M. Oleś, and P. Piekarz, "Lattice dynamics study of electron-correlation-induced charge density wave in antiferromagnetic kagome metal FeGe," *Phys. Rev. Mater.*, vol. 8, p. L080601, 2024.

[33] P. Park, B. R. Ortiz, M. Sprague, A. P. Sakhya, S. A. Chen, M. D. Frontzek, W. Tian, R. Sibille, D. G. Mazzone, C. Tabata, K. Kaneko, L. M. DeBeer-Schmitt, M. B. Stone, D. S. Parker, G. D. Samolyuk, H. Miao, M. Neupane, and A. D. Christianson, "Spin density wave and van hove singularity in the kagome metal $CeTi_3Bi_4$," *Nat. Commun.*, vol. 16, p. 4384, 2025.

[34] H. Chen, H. Yang, B. Hu, Z. Zhao, J. Yuan, Y. Xing, G. Qian, Z. Huang, G. Li, Y. Ye, S. Ma, S. Ni, H. Zhang, Q. Yin, C. Gong, Z. Tu, H. Lei, H. Tan, S. Zhou, C. Shen, X. Dong, B. Yan, Z. Wang, and H.-J. Gao, "Roton pair density wave in a strong-coupling kagome superconductor," *Nature*, vol. 599, p. 222, 2021.

[35] Y.-X. Jiang, S. Shao, W. Xia, M. M. Denner, J. Ingham, M. S. Hossain, Q. Qiu, X. Zheng, H. Chen, Z.-J. Cheng, X. P. Yang, B. Kim, J.-X. Yin, S. Zhang, M. Litskevich, Q. Zhang, T. A. Cochran, Y. Peng, G. Chang, Y. Guo, R. Thomale, T. Neupert, and M. Z. Hasan, "Van Hove annihilation and nematic instability on a kagome lattice," *Nat. Mater.*, vol. 23, p. 1214, 2024.

[36] Z. Jiang, H. Ma, W. Xia, Z. Liu, Q. Xiao, Z. Liu, Y. Yang, J. Ding, Z. Huang, J. Liu, Y. Qiao, J. Liu, Y. Peng, S. Cho, Y. Guo, J. Liu, and D. Shen, "Observation of electronic nematicity driven by the three-dimensional charge density wave in kagome lattice KV_3Sb_5," *Nano Lett.*, vol. 23, p. 5625, 2023.

[37] Y. Xu, Z. Ni, Y. Liu, B. R. Ortiz, Q. Deng, S. D. Wilson, B. Yan, L. Balents, and L. Wu, "Three-state nematicity and magneto-optical Kerr effect in the charge density waves in kagome superconductors," *Nat. Phys.*, vol. 18, p. 1470, 2022.

[38] N. Xia, Y. Guo, and S. Yang, "Unveiling stripe-shaped charge density modulations in doped mott insulators," *Phys. Rev. Lett.*, vol. 135, p. 116504, 2025.

[39] C. Mielke, D. Das, J.-X. Yin, H. Liu, R. Gupta, Y.-X. Jiang, M. Medarde, X. Wu, H. C. Lei, J. Chang, P. Dai, Q. Si, H. Miao, R. Thomale, T. Neupert, Y. Shi, R. Khasanov, M. Z. Hasan, H. Luetkens, and Z. Guguchia, "Time-

reversal symmetry-breaking charge order in a kagome superconductor," *Nature*, vol. 602, p. 245, 2022.

[40] Z. Guguchia, C. Mielke, D. Das, R. Gupta, J.-X. Yin, H. Liu, Q. Yin, M. H. Christensen, Z. Tu, C. Gong, N. Shumiya, M. S. Hossain, T. Gamsakhurdashvili, M. Elender, P. Dai, A. Amato, Y. Shi, H. C. Lei, R. M. Fernandes, M. Z. Hasan, H. Luetkens, and R. Khasanov, "Tunable unconventional kagome superconductivity in charge ordered RbV_3Sb_5 and KV_3Sb_5," *Nat. Commun.*, vol. 14, p. 153, 2023.

[41] M. L. Kiesel, C. Platt, and R. Thomale, "Unconventional Fermi surface instabilities in the kagome Hubbard model," *Phys. Rev. Lett.*, vol. 110, p. 126405, 2013.

[42] R. Karplus and J. M. Luttinger, "Hall effect in ferromagnetics," *Phys. Rev.*, vol. 95, p. 1154, 1954.

[43] J.-X. Yin, W. Ma, T. A. Cochran, X. Xu, S. S. Zhang, H.-J. Tien, N. Shumiya, G. Cheng, K. Jiang, B. Lian, Z. Song, G. Chang, I. Belopolski, D. Multer, M. Litskevich, Z.-J. Cheng, X. P. Yang, B. Swidler, H. Zhou, H. Lin, T. Neupert, Z. Wang, N. Yao, T.-R. Chang, S. Jia, and M. Zahid Hasan, "Quantum-limit Chern topological magnetism in $TbMn_6Sn_6$," *Nature*, vol. 583, p. 533, 2020.

[44] Q. Wang, S. Sun, X. Zhang, F. Pang, and H. Lei, "Anomalous Hall effect in a ferromagnetic Fe_3Sn_2 single crystal with a geometrically frustrated Fe bilayer kagome lattice," *Phys. Rev. B*, vol. 94, p. 075135, 2016.

[45] S. Cheng, B. Wang, I. Lyalin, N. Bagués, A. J. Bishop, D. W. McComb, and R. K. Kawakami, "Atomic layer epitaxy of kagome magnet Fe_3Sn_2 and Sn-modulated heterostructures," *APL Materials*, vol. 10, p. 061112, 2022.

[46] G. Venturini, B. E. Idrissi, and B. Malaman, "Magnetic properties of RMn_6Sn_6 (R = Sc, Y, Gd-Tm, Lu) compounds with $HfFe_6Ge_6$ type structure," *J. Magn. Magn. Mater.*, vol. 94, p. 35, 1991.

[47] W. Ma, X. Xu, J.-X. Yin, H. Yang, H. Zhou, Z.-J. Cheng, Y. Huang, Z. Qu, F. Wang, M. Z. Hasan, and S. Jia, "Rare earth engineering in RMn_6Sn_6 (R=Gd-Tm, Lu) topological kagome magnets," *Phys. Rev. Lett.*, vol. 126, p. 246602, 2021.

[48] Y. Lee, R. Skomski, X. Wang, P. P. Orth, Y. Ren, B. Kang, A. K. Pathak, A. Kutepov, B. N. Harmon, R. J. McQueeney, I. I. Mazin, and L. Ke, "Interplay between magnetism and band topology in the kagome magnets RMn_6Sn_6," *Phys. Rev. B*, vol. 108, p. 045132, 2023.

[49] Y. Wang, H. Wu, G. T. McCandless, J. Y. Chan, and M. N. Ali, "Quantum states and intertwining phases in kagome materials," *Nat. Rev. Phys*, vol. 5, p. 635, 2023.

[50] K. S. Novoselov, A. K. Geim, S. V. Morozov, D. Jiang, M. I. Katsnelson, I. V. Grigorieva, S. V. Dubonos, and A. A. Firsov, "Two-dimensional gas of massless Dirac fermions in graphene," *Nature*, vol. 438, p. 197, 2005.

[51] H. Zhang, J. Koo, C. Xu, M. Sretenovic, B. Yan, and X. Ke, "Exchange-biased topological transverse thermoelectric effects in a kagome ferrimagnet," *Nat. Commun.*, vol. 13, p. 1091, 2022.

[52] X. Xu, J.-X. Yin, W. Ma, H.-J. Tien, X.-B. Qiang, P. V. S. Reddy, H. Zhou, J. Shen, H.-Z. Lu, T.-R. Chang, Z. Qu, and S. Jia, "Topological charge-entropy scaling in kagome Chern magnet $TbMn_6Sn_6$," *Nat. Commun.*, vol. 13, p. 1197, 2022.

[53] D. F. Liu, A. J. Liang, E. K. Liu, Q. N. Xu, Y. W. Li, C. Chen, D. Pei, W. J. Shi, S. K. Mo, P. Dudin, T. Kim, C. Cacho, G. Li, Y. Sun, L. X. Yang, Z. K. Liu, S. S. P. Parkin, C. Felser, and Y. L. Chen, "Magnetic Weyl semimetal phase in a kagomé crystal," *Science*, vol. 365, p. 1282, 2019.

[54] X. Wan, A. M. Turner, A. Vishwanath, and S. Y. Savrasov, "Topological semimetal and Fermi-arc surface states in the electronic structure of pyrochlore iridates," *Phys. Rev. B*, vol. 83, p. 205101, 2011.

[55] N. P. Armitage, E. J. Mele, and A. Vishwanath, "Weyl and Dirac semimetals in three-dimensional solids," *Rev. Mod. Phys.*, vol. 90, p. 015001, 2018.

[56] S.-Y. Xu, I. Belopolski, N. Alidoust, M. Neupane, G. Bian, C. Zhang, R. Sankar, G. Chang, Z. Yuan, C.-C. Lee, S.-M. Huang, H. Zheng, J. Ma, D. S. Sanchez, B. Wang, A. Bansil, F. Chou, P. P. Shibayev, H. Lin, S. Jia, and M. Z. Hasan, "Discovery of a Weyl fermion semimetal and topological Fermi arcs," *Science*, vol. 349, p. 613, 2015.

[57] H. Weyl, "Elektron und gravitation. I," *Zeitschrift für Physik*, vol. 56, p. 330, 1929.

[58] H. Nielsen and M. Ninomiya, "Absence of neutrinos on a lattice," *Nucl. Phys. B*, vol. 185, p. 20, 1981.

[59] M.-Y. Yao, J. Noky, Q.-G. Mu, K. Manna, N. Kumar, V. N. Strocov, C. Shekhar, S. Medvedev, Y. Sun, and C. Felser, "High pressure induced superconductivity and chirality-neutral Fermi surface in $SrSi_2$," *Phys. Rev. B*, vol. 110, p. 224514, 2024.

[60] S. Nakatsuji, N. Kiyohara, and T. Higo, "Large anomalous Hall effect in a non-collinear antiferromagnet at room temperature," *Nature*, vol. 527, p. 212, 2015.

[61] A. K. Nayak, J. E. Fischer, Y. Sun, B. Yan, J. Karel, A. C. Komarek, C. Shekhar, N. Kumar, W. Schnelle, J. Kübler, C. Felser, and S. S. P. Parkin, "Large anomalous Hall effect driven by a nonvanishing Berry curvature in the noncolinear antiferromagnet Mn_3Ge," *Sci. Adv.*, vol. 2, p. e1501870, 2016.

[62] H. Yang, Y. Sun, Y. Zhang, W.-J. Shi, S. S. P. Parkin, and B. Yan, "Topological Weyl semimetals in the chiral antiferromagnetic materials Mn_3Ge and Mn_3Sn," *New J. Phys.*, vol. 19, p. 015008, 2017.

[63] K. Kuroda, T. Tomita, M.-T. Suzuki, C. Bareille, A. A. Nugroho, P. Goswami, M. Ochi, M. Ikhlas, M. Nakayama, S. Akebi, R. Noguchi, R. Ishii, N. Inami,

K. Ono, H. Kumigashira, A. Varykhalov, T. Muro, T. Koretsune, R. Arita, S. Shin, T. Kondo, and S. Nakatsuji, "Evidence for magnetic Weyl fermions in a correlated metal," *Nat. Mater.*, vol. 16, p. 1090, 2017.

[64] J. Kübler and C. Felser, "Weyl fermions in antiferromagnetic Mn_3Sn and Mn_3Ge," *EPL*, vol. 120, p. 47002, 2017.

[65] E. Liu, Y. Sun, N. Kumar, L. Muechler, A. Sun, L. Jiao, S.-Y. Yang, D. Liu, A. Liang, Q. Xu, J. Kroder, V. Süß, H. Borrmann, C. Shekhar, Z. Wang, C. Xi, W. Wang, W. Schnelle, S. Wirth, Y. Chen, S. T. B. Goennenwein, and C. Felser, "Giant anomalous Hall effect in a ferromagnetic kagome-lattice semimetal," *Nat. Phys.*, vol. 14, p. 1125, 2018.

[66] Q. Wang, Y. Xu, R. Lou, Z. Liu, M. Li, Y. Huang, D. Shen, H. Weng, S. Wang, and H. Lei, "Large intrinsic anomalous Hall effect in half-metallic ferromagnet $Co_3Sn_2S_2$ with magnetic Weyl fermions," *Nat. Commun.*, vol. 9, p. 3681, 2018.

[67] J.-R. Soh, C. Yi, I. Zivkovic, N. Qureshi, A. Stunault, B. Ouladdiaf, J. A. Rodríguez-Velamazán, Y. Shi, H. M. Rønnow, and A. T. Boothroyd, "Magnetic structure of the topological semimetal $Co_3Sn_3S_2$," *Phys. Rev. B*, vol. 105, p. 094435, 2022.

[68] Y. Zhang, Y. Sun, H. Yang, J. Železný, S. P. P. Parkin, C. Felser, and B. Yan, "Strong anisotropic anomalous Hall effect and spin Hall effect in the chiral antiferromagnetic compounds Mn_3X (X= Ge, Sn, Ga, Ir, Rh, and Pt)," *Phys. Rev. B*, vol. 95, p. 075128, 2017.

[69] A. A. Burkov and L. Balents, "Weyl semimetal in a topological insulator multilayer," *Phys. Rev. Lett.*, vol. 107, p. 127205, 2011.

[70] T. Chen, T. Tomita, S. Minami, M. Fu, T. Koretsune, M. Kitatani, I. Muhammad, D. Nishio-Hamane, R. Ishii, F. Ishii, R. Arita, and S. Nakatsuji, "Anomalous transport due to Weyl fermions in the chiral antiferromagnets Mn_3X, X = Sn, Ge," *Nat. Commun.*, vol. 12, p. 572, 2021.

[71] J. Liu, Y. Yang, J. Shen, D. Liu, G. S. Thakur, C. Guillemard, A. Smekhova, H. Chen, D. Biswas, M. Valvidares, E. Liu, C. Felser, T.-L. Lee, T. Hesjedal, Y. Chen, and G. van der Laan, "Unusually high occupation of Co 3d state in magnetic Weyl semimetal $Co_3Sn_2S_2$," *ACS Nano*, vol. 19, p. 8561, 2025.

[72] Q. Xu, E. Liu, W. Shi, L. Muechler, J. Gayles, C. Felser, and Y. Sun, "Topological surface Fermi arcs in the magnetic Weyl semimetal $Co_3Sn_2S_2$," *Phys. Rev. B*, vol. 97, p. 235416, 2018.

[73] K. Essafi, L. D. C. Jaubert, and M. Udagawa, "Flat bands and Dirac cones in breathing lattices," *J. Phys.: Condens. Matter*, vol. 29, p. 315802, 2017.

[74] S. Regmi, T. Fernando, Y. Zhao, A. P. Sakhya, G. Dhakal, I. Bin Elius, H. Vazquez, J. D. Denlinger, J. Yang, J.-H. Chu, X. Xu, T. Cao, and M. Neupane, "Spectroscopic evidence of flat bands in breathing kagome semiconductor Nb_3I_8," *Commun. Mater.*, vol. 3, p. 100, 2022.

[75] R. Schaffer, Y. Huh, K. Hwang, and Y. B. Kim, "Quantum spin liquid in a breathing kagome lattice," *Phys. Rev. B*, vol. 95, p. 054410, 2017.

[76] A. Bolens and N. Nagaosa, "Topological states on the breathing kagome lattice," *Phys. Rev. B*, vol. 99, p. 165141, 2019.

[77] F. Schindler, A. M. Cook, M. G. Vergniory, Z. Wang, S. S. P. Parkin, B. A. Bernevig, and T. Neupert, "Higher-order topological insulators," *Sci. Adv.*, vol. 4, p. eaat0346, 2018.

[78] M. Ezawa, "Higher-order topological insulators and semimetals on the breathing kagome and pyrochlore lattices," *Phys. Rev. Lett.*, vol. 120, p. 026801, 2018.

[79] M. A. J. Herrera, S. N. Kempkes, M. B. de Paz, A. García-Etxarri, I. Swart, C. M. Smith, and D. Bercioux, "Corner modes of the breathing kagome lattice: Origin and robustness," *Phys. Rev. B*, vol. 105, p. 085411, 2022.

[80] K. Yatsugi, S. E. Pandarakone, and H. Iizuka, "Higher-order topological corner state in a reconfigurable breathing kagome lattice consisting of magnetically coupled LC resonators," *Sci. Rep.*, vol. 13, p. 8301, 2023.

[81] C. L. Kane and E. J. Mele, "Z_2 topological order and the quantum spin Hall effect," *Phys. Rev. Lett.*, vol. 95, p. 146802, 2005.

[82] B. A. Bernevig, T. L. Hughes, and S.-C. Zhang, "Quantum spin Hall effect and topological phase transition in HgTe quantum wells," *Science*, vol. 314, p. 1757, 2006.

[83] L. Fu and C. L. Kane, "Topological insulators with inversion symmetry," *Phys. Rev. B*, vol. 76, p. 045302, 2007.

[84] Z. Zhu, Y. Cheng, and U. Schwingenschlögl, "Band inversion mechanism in topological insulators: A guideline for materials design," *Phys. Rev. B*, vol. 85, p. 235401, 2012.

[85] L. Balents, "Spin liquids in frustrated magnets," *Nature*, vol. 464, p. 199, 2010.

[86] T.-H. Han, J. S. Helton, S. Chu, D. G. Nocera, J. A. Rodriguez-Rivera, C. Broholm, and Y. S. Lee, "Fractionalized excitations in the spin-liquid state of a kagome-lattice antiferromagnet," *Nature*, vol. 492, p. 406, 2012.

[87] M. Elhajal, B. Canals, and C. Lacroix, "Symmetry breaking due to Dzyaloshinsky-Moriya interactions in the kagomé lattice," *Phys. Rev. B*, vol. 66, p. 014422, 2002.

[88] K. Ohgushi, S. Murakami, and N. Nagaosa, "Spin anisotropy and quantum Hall effect in the kagomé lattice: Chiral spin state based on a ferromagnet," *Phys. Rev. B*, vol. 62, p. R6065, 2000.

[89] T. Asaba, T.-H. Han, B. J. Lawson, F. Yu, C. Tinsman, Z. Xiang, G. Li, Y. S. Lee, and L. Li, "High-field magnetic ground state in $s = \frac{1}{2}$ kagome lattice antiferromagnet $ZnCu_3(OH)_6Cl_2$," *Phys. Rev. B*, vol. 90, p. 064417, 2014.

[90] Y. Taguchi, Y. Oohara, H. Yoshizawa, N. Nagaosa, and Y. Tokura, "Spin chirality, Berry phase, and anomalous Hall effect in a frustrated ferromagnet," *Science*, vol. 291, p. 2573, 2001.

[91] J.-X. Yin, S. S. Zhang, G. Chang, Q. Wang, S. S. Tsirkin, Z. Guguchia, B. Lian, H. Zhou, K. Jiang, I. Belopolski, N. Shumiya, D. Multer, M. Litskevich, T. A. Cochran, H. Lin, Z. Wang, T. Neupert, S. Jia, H. Lei, and M. Z. Hasan, "Negative flat band magnetism in a spin–orbit-coupled correlated kagome magnet," *Nat. Phys.*, vol. 15, p. 443, 2019.

[92] Y. Okamoto, G. J. Nilsen, J. P. Attfield, and Z. Hiroi, "Breathing pyrochlore lattice realized in *a*-site ordered spinel oxides ligacr$_4$o$_8$ and liincr$_4$o$_8$," *Phys. Rev. Lett.*, vol. 110, p. 097203, 2013.

[93] A. Mook, J. Henk, and I. Mertig, "Edge states in topological magnon insulators," *Phys. Rev. B*, vol. 90, p. 024412, 2014.

[94] J. Kondo, "Resistance minimum in dilute magnetic alloys," *Prog. Theor. Phys.*, vol. 32, p. 37, 1964.

[95] C. Kourris and M. Vojta, "Kondo screening and coherence in kagome local-moment metals: Energy scales of heavy fermions in the presence of flat bands," *Phys. Rev. B*, vol. 108, p. 235106, 2023.

[96] D.-B. Nguyen, T.-M. T. Tran, T. T. Nguyen, and M.-T. Tran, "Selective kondo strong coupling in magnetic impurity flat-band lattices," *Ann. Phys. (N. Y.)*, vol. 400, p. 9, 2019.

[97] G. R. Stewart, "Heavy-fermion systems," *Rev. Mod. Phys.*, vol. 56, p. 755, 1984.

[98] B. Song, Y. Xie, W.-J. Li, H. Liu, J. Chen, S. Tian, X. Zhang, Q. Wang, X. Li, H. Lei, Q. Zhang, J.-g. Guo, L. Zhao, S.-L. Yu, X. Zhou, X. Chen, and T. Ying, "Realization of kagome Kondo lattice," *Nat. Commun.*, vol. 16, p. 5643, 2025.

[99] N. W. Ashcroft and N. D. Mermin, *Solid State Physics*. Cengage Learning, new edition ed., 1976.

[100] J. C. Slater and G. F. Koster, "Simplified LCAO method for the periodic potential problem," *Phys. Rev.*, vol. 94, p. 1498, 1954.

[101] P. W. Anderson, "Localized magnetic states in metals," *Phys. Rev.*, vol. 124, p. 41, 1961.

[102] P. ZEEMAN, "The effect of magnetisation on the nature of light emitted by a substance," *Nature*, vol. 55, p. 347, 1897.

[103] W. Pauli, "Zur quantenmechanik des magnetischen elektrons," *Z. Phys.*, vol. 43, p. 601, 1927.

[104] Y. A. Bychkov and E. I. Rashba, "Oscillatory effects and the magnetic susceptibility of carriers in inversion layers," *J. Phys. C: Solid State Phys.*, vol. 17, p. 6039, 1984.

[105] A. Bansil, H. Lin, and T. Das, "Colloquium: Topological band theory," *Rev. Mod. Phys.*, vol. 88, p. 021004, 2016.

[106] Y. Hatsugai, "Chern number and edge states in the integer quantum Hall effect," *Phys. Rev. Lett.*, vol. 71, p. 3697, 1993.

[107] S. M. Bhattacharjee, M. Mj, and A. Bandyopadhyay, eds., *Topology and Condensed Matter Physics*. Texts and Readings in Physical Sciences, Springer Singapore, 1 ed., 2017.

[108] M. P. do Carmo, *Differential Geometry of Curves and Surfaces*. Dover Publications, revised and updated second edition ed., 2016.

[109] C.-K. Chiu, J. C. Y. Teo, A. P. Schnyder, and S. Ryu, "Classification of topological quantum matter with symmetries," *Rev. Mod. Phys.*, vol. 88, p. 035005, 2016.

[110] A. Altland and M. R. Zirnbauer, "Nonstandard symmetry classes in mesoscopic normal-superconducting hybrid structures," *Phys. Rev. B*, vol. 55, p. 1142, 1997.

[111] A. Kitaev, "Periodic table for topological insulators and superconductors," *AIP Conf. Proc.*, vol. 1134, p. 22, 2009.

[112] D. Xiao, M.-C. Chang, and Q. Niu, "Berry phase effects on electronic properties," *Rev. Mod. Phys.*, vol. 82, p. 1959, 2010.

[113] M. V. Berry, "Quantal phase factors accompanying adiabatic changes," *Proc. R. Soc. A*, vol. 392, p. 45, 1984.

[114] A. Euceda, D. M. Bylander, and L. Kleinman, "Self-consistent electronic structure of 6- and 18-layer Cu(111) films," *Phys. Rev. B*, vol. 28, p. 528, 1983.

[115] S. D. Kevan, "Evidence for a new broadening mechanism in angle-resolved photoemission from Cu(111)," *Phys. Rev. Lett.*, vol. 50, p. 526, 1983.

[116] A. Zangwill, *Physics at Surfaces*. Cambridge University Press, 1988.

[117] W. Shockley, "On the surface states associated with a periodic potential," *Phys. Rev.*, vol. 56, p. 317, 1939.

[118] A. H. Castro Neto, F. Guinea, N. M. R. Peres, K. S. Novoselov, and A. K. Geim, "The electronic properties of graphene," *Rev. Mod. Phys.*, vol. 81, p. 109, 2009.

[119] M. Ridene, J. Girard, L. Travers, C. David, and A. Ouerghi, "STM/STS investigation of edge structure in epitaxial graphene," *Surface Science*, vol. 606, p. 1289, 2012.

[120] J. Lado, N. García-Martínez, and J. Fernández-Rossier, "Edge states in graphene-like systems," *Synthetic Metals*, vol. 210, p. 56, 2015.

[121] G. Z. Magda, X. Jin, I. Hagymási, P. Vancsó, Z. Osváth, P. Nemes-Incze, C. Hwang, L. P. Biró, and L. Tapasztó, "Room-temperature magnetic order

on zigzag edges of narrow graphene nanoribbons," *Nature*, vol. 514, p. 608, 2014.

[122] M. Fujita, K. Wakabayashi, K. Nakada, and K. Kusakabe, "Peculiar localized state at zigzag graphite edge," *J. Phys. Soc. Jpn.*, vol. 65, p. 1920, 1996.

[123] K. Nakada, M. Fujita, G. Dresselhaus, and M. S. Dresselhaus, "Edge state in graphene ribbons: Nanometer size effect and edge shape dependence," *Phys. Rev. B*, vol. 54, p. 17954, 1996.

[124] L. Brey and H. A. Fertig, "Electronic states of graphene nanoribbons studied with the Dirac equation," *Phys. Rev. B*, vol. 73, p. 235411, 2006.

[125] Y.-W. Son, M. L. Cohen, and S. G. Louie, "Half-metallic graphene nanoribbons," *Nature*, vol. 444, p. 347, 2006.

[126] E. H. Lieb, "Two theorems on the Hubbard model," *Phys. Rev. Lett.*, vol. 62, p. 1201, 1989.

[127] M. Kabir and T. Saha-Dasgupta, "Manipulation of edge magnetism in hexagonal graphene nanoflakes," *Phys. Rev. B*, vol. 90, p. 035403, 2014.

[128] J. J. Palacios, J. Fernández-Rossier, and L. Brey, "Vacancy-induced magnetism in graphene and graphene ribbons," *Phys. Rev. B*, vol. 77, p. 195428, 2008.

[129] S. Yang, J. Li, and S.-S. Li, "Antiferromagnetic–ferromagnetic transition in zigzag graphene nanoribbons induced by substitutional doping," *Chinese Phys. B*, vol. 27, p. 117102, 2018.

[130] O. V. Yazyev, "Emergence of magnetism in graphene materials and nanostructures," *Rep. Prog. Phys.*, vol. 73, p. 056501, 2010.

[131] S. Sorella and E. Tosatti, "Semi-metal-insulator transition of the Hubbard model in the honeycomb lattice," *EPL*, vol. 19, p. 699, 1992.

[132] L. Pisani, J. A. Chan, B. Montanari, and N. M. Harrison, "Electronic structure and magnetic properties of graphitic ribbons," *Phys. Rev. B*, vol. 75, p. 064418, 2007.

[133] P. A. M. Dirac and R. H. Fowler, "The quantum theory of the electron," *Proc. R. Soc. A*, vol. 117, p. 610, 1928.

[134] L. Van Hove, "The occurrence of singularities in the elastic frequency distribution of a crystal," *Phys. Rev.*, vol. 89, p. 1189, 1953.

[135] R. Markiewicz, "A survey of the Van Hove scenario for high-tc superconductivity with special emphasis on pseudogaps and striped phases," *J. Phys. Chem. Solids*, vol. 58, p. 1179, 1997.

[136] Y. Hu, X. Wu, A. P. Schnyder, and M. Shi, "Electronic landscape of kagome superconductors AV_3Sb_5 (A = K, Rb, Cs) from angle-resolved photoemission spectroscopy," *npj Quantum Mater.*, vol. 8, p. 67, 2023.

[137] M. Kang, S. Fang, J.-K. Kim, B. R. Ortiz, S. H. Ryu, J. Kim, J. Yoo, G. Sangiovanni, D. Di Sante, B.-G. Park, C. Jozwiak, A. Bostwick, E. Rotenberg, E. Kaxiras, S. D. Wilson, J.-H. Park, and R. Comin, "Twofold van hove singularity and origin of charge order in topological kagome superconductor CsV_3Sb_5," *Nat. Phys.*, vol. 18, p. 301, 2022.

[138] S. Lee, C. Won, J. Kim, J. Yoo, S. Park, J. Denlinger, C. Jozwiak, A. Bostwick, E. Rotenberg, R. Comin, M. Kang, and J.-H. Park, "Nature of charge density wave in kagome metal ScV_6Sn_6," *npj Quantum Mater.*, vol. 9, p. 15, 2024.

[139] G. Grüner, "The dynamics of charge-density waves," *Rev. Mod. Phys.*, vol. 60, p. 1129, 1988.

[140] T. M. Rice and G. K. Scott, "New mechanism for a charge-density-wave instability," *Phys. Rev. Lett.*, vol. 35, p. 120, 1975.

[141] M. D. Johannes and I. I. Mazin, "Fermi surface nesting and the origin of charge density waves in metals," *Phys. Rev. B*, vol. 77, p. 165135, 2008.

[142] A. W. Overhauser, "Spin density waves in an electron gas," *Phys. Rev.*, vol. 128, p. 1437, 1962.

[143] G. Grüner, "The dynamics of spin-density waves," *Rev. Mod. Phys.*, vol. 66, p. 1, 1994.

[144] E. Berg, E. Fradkin, and S. A. Kivelson, "Charge-4e superconductivity from pair-density-wave order in certain high-temperature superconductors," *Nat. Phys.*, vol. 5, p. 830, 2009.

[145] R. M. Fernandes, A. V. Chubukov, and J. Schmalian, "What drives nematic order in iron-based superconductors?," *Nat. Phys.*, vol. 10, p. 97, 2014.

[146] C. M. Varma, "Non-fermi-liquid states and pairing instability of a general model of copper oxide metals," *Phys. Rev. B*, vol. 55, p. 14554, 1997.

[147] W.-S. Wang, Z.-Z. Li, Y.-Y. Xiang, and Q.-H. Wang, "Competing electronic orders on kagome lattices at van Hove filling," *Phys. Rev. B*, vol. 87, p. 115135, 2013.

[148] R. Nandkishore, L. S. Levitov, and A. V. Chubukov, "Chiral superconductivity from repulsive interactions in doped graphene," *Nat. Phys.*, vol. 8, p. 158, 2012.

[149] M. Imada, A. Fujimori, and Y. Tokura, "Metal-insulator transitions," *Rev. Mod. Phys.*, vol. 70, p. 1039, 1998.

[150] E. Tang, J.-W. Mei, and X.-G. Wen, "High-temperature fractional quantum Hall states," *Phys. Rev. Lett.*, vol. 106, p. 236802, 2011.

[151] T. T. Heikkilä, N. B. Kopnin, and G. E. Volovik, "Flat bands in topological media," *JETP Lett.*, vol. 94, p. 233, 2011.

[152] D. Leykam, A. Andreanov, and S. Flach, "Artificial flat band systems: from lattice models to experiments," *Adv. Phys. X*, vol. 3, p. 1473052, 2018.

[153] Y. Cao, V. Fatemi, S. Fang, K. Watanabe, T. Taniguchi, E. Kaxiras, and P. Jarillo-Herrero, "Unconventional superconductivity in magic-angle graphene superlattices," *Nature*, vol. 556, p. 43, 2018.

[154] Y. Cao, V. Fatemi, A. Demir, S. Fang, S. L. Tomarken, J. Y. Luo, J. D. Sanchez-Yamagishi, K. Watanabe, T. Taniguchi, E. Kaxiras, R. C. Ashoori, and P. Jarillo-Herrero, "Correlated insulator behaviour at half-filling in magic-angle graphene superlattices," *Nature*, vol. 556, p. 80, 2018.

[155] R. Bistritzer and A. H. MacDonald, "Moiré bands in twisted double-layer graphene," *PNAS*, vol. 108, p. 12233, 2011.

[156] H.-M. Guo and M. Franz, "Topological insulator on the kagome lattice," *Phys. Rev. B*, vol. 80, p. 113102, 2009.

[157] D. L. Bergman, C. Wu, and L. Balents, "Band touching from real-space topology in frustrated hopping models," *Phys. Rev. B*, vol. 78, p. 125104, 2008.

[158] E. C. Stoner, "Collective electron ferromagnetism," *Proc. R. Soc. A*, vol. 165, p. 372, 1938.

[159] A. Mielke, "Ferromagnetism in the Hubbard model and Hund's rule," *Phys. Lett. A*, vol. 174, p. 443, 1993.

[160] J. R. Schrieffer, *Theory of Superconductivity*. CRC Press, 2018.

[161] A. Julku, S. Peotta, T. I. Vanhala, D.-H. Kim, and P. Törmä, "Geometric origin of superfluidity in the Lieb-lattice flat band," *Phys. Rev. Lett.*, vol. 117, p. 045303, 2016.

[162] G. Wachutka, "Change of the density of electron states caused by the surface of a layered crystal structure," *Phys. Rev. B*, vol. 36, p. 4725, 1987.

[163] K. Wakabayashi, K.-i. Sasaki, T. Nakanishi, and T. Enoki, "Electronic states of graphene nanoribbons and analytical solutions," *Sci. Technol. Adv. Mater.*, vol. 11, p. 054504, 2010.

[164] O. Busch, I. Mertig, and B. Göbel, "Orbital Hall effect and orbital edge states caused by *s* electrons," *Phys. Rev. Res.*, vol. 5, p. 043052, 2023.

[165] T. P. Cysne, L. M. Canonico, M. Costa, R. B. Muniz, and T. G. Rappoport, "Orbitronics in two-dimensional materials," *npj Spintronics*, vol. 3, p. 39, 2025.

[166] J. J. Sakurai and J. Napolitano, *Modern Quantum Mechanics*. Pearson, 2nd ed., 2010.

[167] M. König, S. Wiedmann, C. Brüne, A. Roth, H. Buhmann, L. W. Molenkamp, X.-L. Qi, and S.-C. Zhang, "Quantum spin Hall insulator state in HgTe quantum wells," *Science*, vol. 318, p. 766, 2007.

[168] A. Roth, C. Brüne, H. Buhmann, L. W. Molenkamp, J. Maciejko, X.-L. Qi, and S.-C. Zhang, "Nonlocal transport in the quantum spin Hall state," *Science*, vol. 325, p. 294, 2009.

[169] R. Takahashi and S. Murakami, "Thermoelectric transport in topological insulators," *Semicond. Sci. Technol.*, vol. 27, p. 124005, 2012.

[170] N. Xu, Y. Xu, and J. Zhu, "Topological insulators for thermoelectrics," *npj Quantum Mater.*, vol. 2, p. 51, 2017.

[171] G. Blasi, F. Taddei, L. Arrachea, M. Carrega, and A. Braggio, "Nonlocal thermoelectricity in a superconductor–topological-insulator–superconductor junction in contact with a normal-metal probe: Evidence for helical edge states," *Phys. Rev. Lett.*, vol. 124, p. 227701, 2020.

[172] M. Z. Hasan and C. L. Kane, "Colloquium: Topological insulators," *Rev. Mod. Phys.*, vol. 82, p. 3045, 2010.

[173] X.-L. Qi and S.-C. Zhang, "Topological insulators and superconductors," *Rev. Mod. Phys.*, vol. 83, p. 1057, 2011.

[174] A. G. Grushin, "Introduction to topological phases in condensed matter," 2024. Lecture notes.

[175] X.-L. Qi and S.-C. Zhang, "The quantum spin Hall effect and topological insulators," *Phys. Today*, vol. 63, p. 33, 2010.

[176] A. A. Soluyanov and D. Vanderbilt, "Wannier representation of Z_2 topological insulators," *Phys. Rev. B*, vol. 83, p. 035108, 2011.

[177] A. A. Soluyanov and D. Vanderbilt, "Smooth gauge for topological insulators," *Phys. Rev. B*, vol. 85, p. 115415, 2012.

[178] A. A. Soluyanov and D. Vanderbilt, "Computing topological invariants without inversion symmetry," *Phys. Rev. B*, vol. 83, p. 235401, 2011.

[179] G. Pizzi, V. Vitale, R. Arita, S. Blügel, F. Freimuth, G. Géranton, M. Gibertini, D. Gresch, C. Johnson, T. Koretsune, J. Ibañez-Azpiroz, H. Lee, J.-M. Lihm, D. Marchand, A. Marrazzo, Y. Mokrousov, J. I. Mustafa, Y. Nohara, Y. Nomura, L. Paulatto, S. Poncé, T. Ponweiser, J. Qiao, F. Thöle, S. S. Tsirkin, M. Wierzbowska, N. Marzari, D. Vanderbilt, I. Souza, A. A. Mostofi, and J. R. Yates, "Wannier90 as a community code: new features and applications," *J. Phys.: Condens. Matter*, vol. 32, p. 165902, 2020.

[180] D. Gresch, G. Autès, O. V. Yazyev, M. Troyer, D. Vanderbilt, B. A. Bernevig, and A. A. Soluyanov, "Z2Pack: Numerical implementation of hybrid Wannier centers for identifying topological materials," *Phys. Rev. B*, vol. 95, p. 075146, 2017.

[181] R. Yu, X. L. Qi, A. Bernevig, Z. Fang, and X. Dai, "Equivalent expression of Z_2 topological invariant for band insulators using the non-Abelian Berry connection," *Phys. Rev. B*, vol. 84, p. 075119, 2011.

[182] K. von Klitzing, "The quantized Hall effect," *Rev. Mod. Phys.*, vol. 58, p. 519, 1986.

[183] K. v. Klitzing, G. Dorda, and M. Pepper, "New method for high-accuracy determination of the fine-structure constant based on quantized Hall resistance," *Phys. Rev. Lett.*, vol. 45, p. 494, 1980.

[184] K. von Klitzing, "Developments in the quantum Hall effect," *Philos. Trans. R. Soc. A*, vol. 363, p. 2203, 2005.

[185] L. Landau, "Diamagnetismus der metalle," *Z. Phys.*, vol. 64, p. 629, 1930.

[186] T. Ando, Y. Matsumoto, and Y. Uemura, "Theory of Hall effect in a two-dimensional electron system," *J. Phys. Soc. Jpn.*, vol. 39, p. 279, 1975.

[187] D. J. Thouless, M. Kohmoto, M. P. Nightingale, and M. den Nijs, "Quantized Hall conductance in a two-dimensional periodic potential," *Phys. Rev. Lett.*, vol. 49, p. 405, 1982.

[188] C.-Z. Chang, C.-X. Liu, and A. H. MacDonald, "Colloquium: Quantum anomalous Hall effect," *Rev. Mod. Phys.*, vol. 95, p. 011002, 2023.

[189] C.-X. Liu, X.-L. Qi, X. Dai, Z. Fang, and S.-C. Zhang, "Quantum anomalous Hall effect in $Hg_{1-y}Mn_yTe$ quantum wells," *Phys. Rev. Lett.*, vol. 101, p. 146802, 2008.

[190] X.-L. Qi, T. L. Hughes, and S.-C. Zhang, "Topological field theory of time-reversal invariant insulators," *Phys. Rev. B*, vol. 78, p. 195424, 2008.

[191] R. Yu, W. Zhang, H.-J. Zhang, S.-C. Zhang, X. Dai, and Z. Fang, "Quantized anomalous Hall effect in magnetic topological insulators," *Science*, vol. 329, p. 61, 2010.

[192] C.-Z. Chang, J. Zhang, X. Feng, J. Shen, Z. Zhang, M. Guo, K. Li, Y. Ou, P. Wei, L.-L. Wang, Z.-Q. Ji, Y. Feng, S. Ji, X. Chen, J. Jia, X. Dai, Z. Fang, S.-C. Zhang, K. He, Y. Wang, L. Lu, X.-C. Ma, and Q.-K. Xue, "Experimental observation of the quantum anomalous Hall effect in a magnetic topological insulator," *Science*, vol. 340, p. 167, 2013.

[193] C.-Z. Chang, W. Zhao, D. Y. Kim, H. Zhang, B. A. Assaf, D. Heiman, S.-C. Zhang, C. Liu, M. H. W. Chan, and J. S. Moodera, "High-precision realization

of robust quantum anomalous Hall state in a hard ferromagnetic topological insulator," *Nat. Mater.*, vol. 14, p. 473, 2015.

[194] N. Read and D. Green, "Paired states of fermions in two dimensions with breaking of parity and time-reversal symmetries and the fractional quantum Hall effect," *Phys. Rev. B*, vol. 61, p. 10267, 2000.

[195] F. D. M. Haldane, "Model for a quantum Hall effect without Landau levels: Condensed-matter realization of the "parity anomaly"," *Phys. Rev. Lett.*, vol. 61, p. 2015, 1988.

[196] G. Xu, B. Lian, and S.-C. Zhang, "Intrinsic quantum anomalous Hall effect in the kagome lattice $Cs_2LiMn_3F_{12}$," *Phys. Rev. Lett.*, vol. 115, p. 186802, 2015.

[197] B. P. Belbase, L. Ye, B. Karki, J. I. Facio, J.-S. You, J. G. Checkelsky, J. van den Brink, and M. P. Ghimire, "Large anomalous Hall effect in single crystals of the kagome Weyl ferromagnet Fe_3Sn," *Phys. Rev. B*, vol. 108, p. 075164, 2023.

[198] Z. Zhang, J.-Y. You, X.-Y. Ma, B. Gu, and G. Su, "Kagome quantum anomalous Hall effect with high Chern number and large band gap," *Phys. Rev. B*, vol. 103, p. 014410, 2021.

[199] S. E. Pate, B. Wang, Y. Zhang, B. Shen, E. Liu, I. Martin, J. S. Jiang, X. Zhou, D. Y. Chung, M. G. Kanatzidis, U. Welp, W.-K. Kwok, and Z.-L. Xiao, "Tunable anomalous Hall effect in a kagomé ferromagnetic Weyl semimetal," *Adv. Sci.*, vol. 11, p. 2406882, 2024.

[200] W. Ren, W. Li, G. Feng, L. Jiang, J. Gan, Y. Han, X. Luo, C. Chen, C. Fang, and S. Ma, "Large room temperature anomalous Hall and Nernst effects in kagomé $ZrFe_2$ ferromagnet," *Mater. Today Phys.*, vol. 57, p. 101838, 2025.

[201] C. Q. Xu, T. W. Heitmann, H. Zhang, X. Xu, and X. Ke, "Magnetic phase transition, magnetoresistance, and anomalous Hall effect in Ga-substituted YMn_6Sn_6 with a ferromagnetic kagome lattice," *Phys. Rev. B*, vol. 104, p. 024413, 2021.

[202] D. Chen, C. Le, C. Fu, H. Lin, W. Schnelle, Y. Sun, and C. Felser, "Large anomalous Hall effect in the kagome ferromagnet $LiMn_6Sn_6$," *Phys. Rev. B*, vol. 103, p. 144410, 2021.

[203] H. Zeng, G. Yu, X. Luo, C. Chen, C. Fang, S. Ma, Z. Mo, J. Shen, M. Yuan, and Z. Zhong, "Large anomalous Hall effect in kagomé ferrimagnetic $HoMn_6Sn_6$ single crystal," *J. Alloys Compd.*, vol. 899, p. 163356, 2022.

[204] Y.-p. Wang, W.-x. Ji, C.-w. Zhang, P. Li, P.-j. Wang, B. Kong, S.-s. Li, S.-s. Yan, and K. Liang, "Discovery of intrinsic quantum anomalous Hall effect in organic Mn-DCA lattice," *Appl. Phys. Lett.*, vol. 110, p. 233107, 2017.

[205] P. Li, Y. Ma, Y. Zhang, and Z.-X. Guo, "Room temperature quantum anomalous Hall insulator in a honeycomb-kagome lattice, Ta_2O_3, with huge magnetic anisotropy energy," *ACS Appl. Electron. Mater.*, vol. 3, p. 1826, 2021.

[206] T. Jungwirth, Q. Niu, and A. H. MacDonald, "Anomalous Hall effect in ferromagnetic semiconductors," *Phys. Rev. Lett.*, vol. 88, p. 207208, 2002.

[207] N. Nagaosa, J. Sinova, S. Onoda, A. H. MacDonald, and N. P. Ong, "Anomalous Hall effect," *Rev. Mod. Phys.*, vol. 82, p. 1539, 2010.

[208] G. E. Volovik, "Topological Lifshitz transitions," *Low Temp. Phys.*, vol. 43, p. 47, 2017.

[209] I. M. Lifshitz, "Anomalies of electron characteristics of a metal in the high pressure region," *Soviet Physics JETP*, vol. 11, p. 1130, 1960.

[210] S. Beaulieu, S. Dong, N. Tancogne-Dejean, M. Dendzik, T. Pincelli, J. Maklar, R. P. Xian, M. A. Sentef, M. Wolf, A. Rubio, L. Rettig, and R. Ernstorfer, "Ultrafast dynamical Lifshitz transition," *Sci. Adv.*, vol. 7, p. eabd9275, 2021.

[211] G. Tatara and H. Kawamura, "Chirality-driven anomalous Hall effect in weak coupling regime," *J. Phys. Soc. Jpn.*, vol. 71, p. 2613, 2002.

[212] X. G. Wen, F. Wilczek, and A. Zee, "Chiral spin states and superconductivity," *Phys. Rev. B*, vol. 39, p. 11413, 1989.

[213] N. Kiyohara, T. Tomita, and S. Nakatsuji, "Giant anomalous Hall effect in the chiral antiferromagnet Mn_3Ge," *Phys. Rev. Appl.*, vol. 5, p. 064009, 2016.

[214] A. Chubukov, "Order from disorder in a kagomé antiferromagnet," *Phys. Rev. Lett.*, vol. 69, p. 832, 1992.

[215] A. B. Harris, C. Kallin, and A. J. Berlinsky, "Possible Néel orderings of the kagomé antiferromagnet," *Phys. Rev. B*, vol. 45, p. 2899, 1992.

[216] O. Götze, D. J. J. Farnell, R. F. Bishop, P. H. Y. Li, and J. Richter, "Heisenberg antiferromagnet on the kagome lattice with arbitrary spin: A higher-order coupled cluster treatment," *Phys. Rev. B*, vol. 84, p. 224428, 2011.

[217] B. Li, S. Sandhoefner, and A. A. Kovalev, "Intrinsic spin Nernst effect of magnons in a noncollinear antiferromagnet," *Phys. Rev. Res.*, vol. 2, p. 013079, 2020.

[218] T. Yildirim and A. B. Harris, "Magnetic structure and spin waves in the kagomé jarosite compound $KFe_3(SO_4)_2(OH)_6$," *Phys. Rev. B*, vol. 73, p. 214446, 2006.

[219] A. Verrier, F. Bert, J. M. Parent, M. El-Amine, J. C. Orain, D. Boldrin, A. S. Wills, P. Mendels, and J. A. Quilliam, "Canted antiferromagnetic order in the kagome material Sr-vesignieite," *Phys. Rev. B*, vol. 101, p. 054425, 2020.

[220] K. Fujiwara, Y. Kato, T. Seki, K. Nomura, K. Takanashi, Y. Motome, and A. Tsukazaki, "Tuning scalar spin chirality in ultrathin films of the kagome-lattice ferromagnet Fe_3Sn," *Commun. Mater.*, vol. 2, p. 113, 2021.

[221] M. Taillefumier, B. Canals, C. Lacroix, V. K. Dugaev, and P. Bruno, "Anomalous Hall effect due to spin chirality in the kagomé lattice," *Phys. Rev. B*, vol. 74, p. 085105, 2006.

[222] P. Laurell and G. A. Fiete, "Magnon thermal Hall effect in kagome antiferromagnets with Dzyaloshinskii–Moriya interactions," *Phys. Rev. B*, vol. 98, p. 094419, 2018.

[223] W. Zhang, T. C. Asmara, Y. Tseng, J. Li, Y. Xiong, Y. Wei, T. Yu, C. W. Galdino, Z. Zhang, K. Kummer, V. N. Strocov, Y. Soh, T. Schmitt, and G. Aeppli, "Spin waves and orbital contribution to ferromagnetism in a topological metal," *Nat. Commun.*, vol. 15, p. 8905, 2024.

[224] B. Song, Y. Xie, W.-J. Li, H. Liu, J. Chen, S. Tian, X. Zhang, Q. Wang, X. Li, H. Lei, Q. Zhang, J.-g. Guo, L. Zhao, S.-L. Yu, X. Zhou, X. Chen, and T. Ying, "Realization of kagome Kondo lattice," *Nat. Commun.*, vol. 16, p. 5643, 2025.

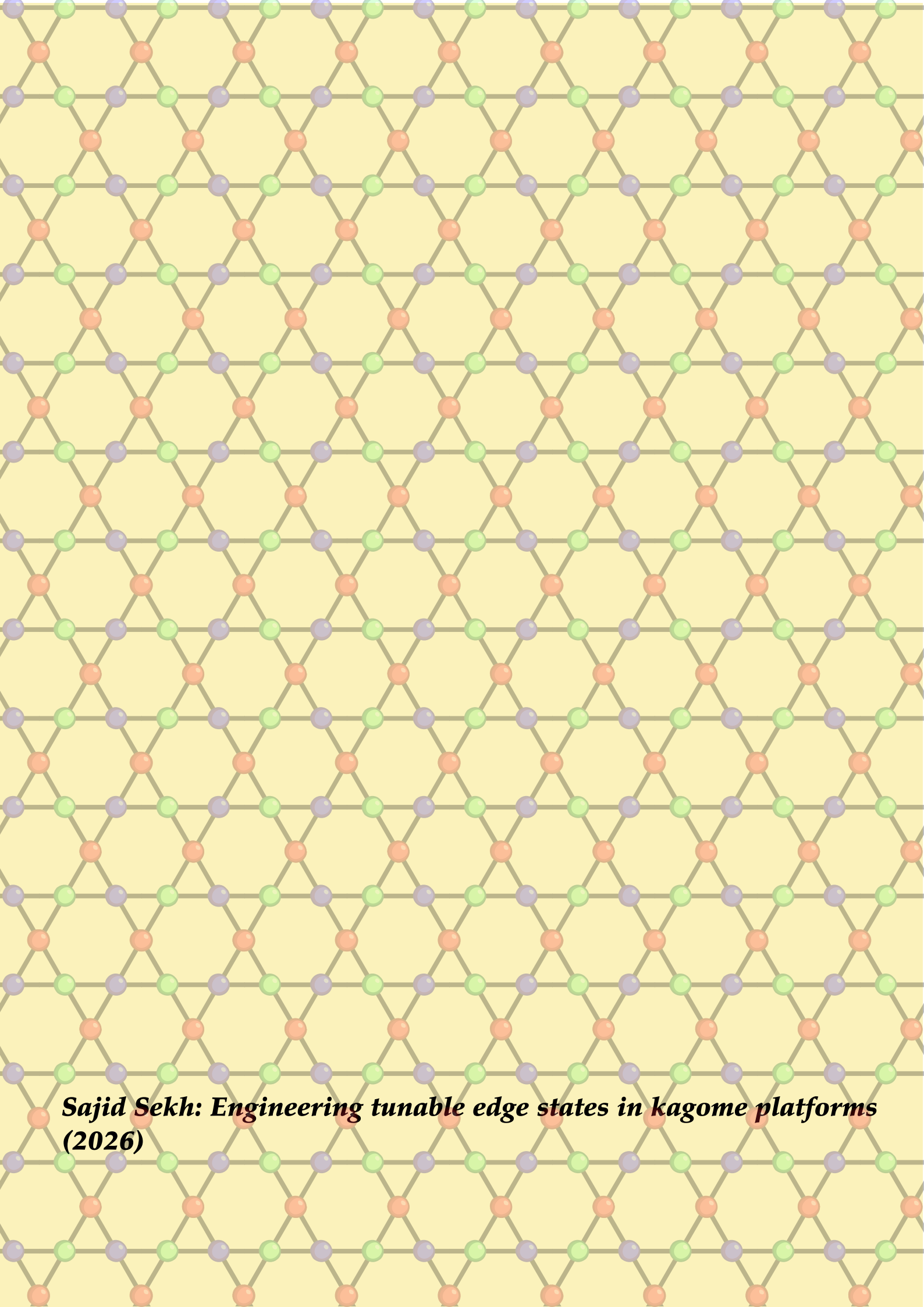

Sajid Sekh: Engineering tunable edge states in kagome platforms (2026)